Characterization of Endoplasmic Reticulum Gla Protein (ERGP), a novel γ-carboxylated protein regulating calcium flux in pancreatic β-cells

By

Kevin Guo

Division of Experimental Medicine

Faculty of Medicine

McGill University

Montreal, Quebec, Canada

June 2024

A thesis submitted to McGill University in partial fulfillment of the requirements of the degree of Doctor of Philosophy

i. Abstract

Increased vitamin K intake may prevent the development of diabetes. However, the mechanism by which it confers this protective effect is unknown. Vitamin K is an essential cofactor for gamma-glutamyl carboxylase (GGCX), which converts glutamic acid (Glu) into gamma-carboxyglutamic acid (Gla) residues in proteins within the endoplasmic reticulum (ER). In this study, we demonstrated that beta-cells lacking GGCX fail to adapt their insulin secretion in response to glucose in the context of diet-induced beta-cell stress, leading to elevated fasting insulin and peripheral insulin resistance. Recently, we discovered ER Gla protein (ERGP) as a new transmembrane gamma-carboxylated protein in beta-cells with Gla residues localized to ERGP's luminal "Glu-rich domain". We hypothesized that gamma-carboxylation is essential for the functioning of ERGP and that it may mediate the protective effect of vitamin K against diabetes. In HEK293 cells, carboxylated ERGP reduces store-operated calcium entry (SOCE) and ER calcium stores. *Ggcx*-deficient beta-cells lacking carboxylated ERGP exhibited elevated basal cytosolic calcium and increased SOCE. In addition, the absence of carboxylated ERGP disrupts normal whole islet calcium oscillatory patterns and intra-islet beta cell connectivity by increasing the period of calcium oscillation and reducing the coactivity of individual islet cells. We next used TurboID, a proximity labeling assay, to characterize ERGP interactors. This led to the identification of the IP_3 receptors (ITPR1-3), which are involved in ER calcium efflux, and STIM2, a regulator of SOCE, as interactors of ERGP. Other identified interactors suggest that carboxylated ERGP may also be involved in ER protein folding and the unfolded protein response and in cell-cell interactions. Altogether, this work reveals a new function for gamma-carboxylation in regulating calcium fluxes in beta-cells.

ii. Résumé

Une augmentation de l'apport en vitamine K pourrait prévenir le développement du diabète. Cependant, le mécanisme par lequel elle confère cet effet protecteur reste inconnu. La vitamine K est un cofacteur essentiel pour la gamma-glutamyl carboxylase (GGCX), qui convertit l'acide glutamique (Glu) en résidus d'acide gamma-carboxyglutamique (Gla) dans les protéines du réticulum endoplasmique (RE). Dans cette étude, nous avons démontré que les cellules bêta dépourvues de GGCX ne parviennent pas à adapter leur sécrétion d'insuline en réponse au glucose dans un contexte de stress des cellules bêta induit par l'alimentation. Ceci entraînant une augmentation de l'insuline à jeun et une résistance périphérique à l'insuline. Récemment, nous avons découvert la protéine Gla du RE (ERGP) comme une nouvelle protéine transmembranaire gamma-carboxylée dans les cellules bêta, avec des résidus Gla localisés dans le "domaine riche en Glu" luminal de l'ERGP. Nous avons émis l'hypothèse que la gamma-carboxylation est essentielle au fonctionnement de l'ERGP et qu'elle pourrait médier l'effet protecteur de la vitamine K contre le diabète. Dans les cellules HEK293, l'ERGP carboxylée réduit l'entrée de calcium dépendant des stocks (SOCE) et les réserves de calcium du RE. Les cellules bêta déficientes en Ggcx, dépourvues d'ERGP carboxylée, ont montré une augmentation du calcium cytosolique basal et une SOCE accrue. En outre, l'absence d'ERGP carboxylée perturbe les modèles oscillatoires normaux du calcium dans les îlots entiers et la connectivité des cellules bêta au sein de l'îlot en augmentant la période d'oscillation du calcium et en réduisant la coactivité des cellules individuelles de l'îlot. Nous avons ensuite utilisé TurboID, un test de marquage de proximité, pour caractériser les interacteurs d'ERGP, ce qui a conduit à l'identification des récepteurs IP3 (ITPR1-3), impliqués dans l'efflux de calcium du RE, et de STIM2, un régulateur de la SOCE, comme interacteurs d'ERGP. D'autres interacteurs identifiés

suggèrent que l’ERGP carboxylée pourrait également être impliquée dans le repliement des protéines dans le RE et la réponse aux protéines mal repliées ainsi que dans les interactions cellule-cellule. Dans l'ensemble, ce travail révèle une nouvelle fonction de la gamma-carboxylation dans la régulation des flux de calcium dans les cellules bêta.

iii. Acknowledgements

A massive thank you to my supervisor Mathieu Ferron. It was such an honor to grow with you these last couple of years. Our moments of mutual torture turned out to generate some pretty good science in the end! Most of all, I'd like to thank Julie Lacombe who started the beta cell project and co-supervised me throughout my PhD. You remain one of the best examples of what it means to be a good scientist. Thank you to the excellent core facilities at the IRCM. Special shout out to Dominic Filion for helping me wrangle the spinning disk confocal on which many of the experiments presented in this thesis were performed. Thank you to all the members of the animal facilities at IRCM for working tirelessly to care for our mouse lines.

I'd also like to thank the other students in the lab who struggled alongside me these years. To Omar Al-Rafai, who liked to act as the father of the lab, to Celine Schott, with whom I loved to share gossip, and to Shayesteh Kiani, whose fierceness of spirit is only matched by her sharp intellect, it was such a pleasure to work with all of you. Thank you to Florian Gioanni for being an excellent undergraduate trainee and for his company throughout the worst of the COVID19 lockdowns in Montreal. To Danyl Khider, who I hope is actually reading this thesis since you're going to inherit the project, I have a few things to say to you 1) you are far more capable than you think, 2) only you can give yourself confidence, 3) look at the clock, is it past midnight? If so, immediately go to bed, you make stupid mistakes when you're tired.

A massive thank you to all my family and friends throughout these years. To my father Zhenyu Guo, I am now Dr. Guo, do NOT call me Dr. Guo Jr. I am my own doctor now. To my mother Quan Zhou, thank you so much for your love and support, I hope I've done you proud. To my sister Louisa Guo, I did it! Who would've thought, eh? (Not me, tbh) And to Juliette, my beautiful love, I can't wait to start the rest of my life with you <3.

iv. <u>Contribution to original knowledge</u>

The expression of vitamin K dependent gamma-carboxylated proteins in the pancreatic islet had previously never been demonstrated. While the protective effect of vitamin K on the development of type 2 diabetes (T2D) had been known, the tissues affected and molecular mechanism underlying its effect was entirely unknown. This study details the very first published work characterizing the role of vitamin K dependent gamma-carboxylation specifically in beta cells. We discovered a fasting hyperinsuliemic phenotype in mice lacking gamma-carboxylation specifically in the beta cells (*Ggcx*^{ff}*;Ins1-Cre*) following a one week high fat diet, suggesting that vitamin K dependent gamma-carboxylation is necessary for beta-cells to adapt to metabolic stress.

This study was also the first to identify ASPH and ERGP as vitamin K-dependent gamma-carboxylated proteins. Importantly, we found that gamma-carboxylation is necessary for the functioning of ERGP, a discovery that prompted us to change the protein's name to reflect this quality. When carboxylated, we found that ERGP suppresses store-operated calcium entry (SOCE) by inhibiting the formation of the SOCE complex, potentially preventing calcium overfilling of the beta-cell and subsequent high fat diet induced fasting hyperinsulinemia. This study was also the first to identify the interactome of ERGP. Using TurboID screens, we identified numerous potential interactors of ERGP, including the SOCE complex proteins STIM1 and STIM2 and the IP_3 receptor proteins ITPR1, ITPR2, and ITPR3. Finally, this study was also the first to characterize a potential role for carboxylated ERGP in regulating whole islet calcium oscillations by maintaining islet cell coordination and coactivity.

v. Contribution of authors

Chapter 2:

Julie Lacombe, Kevin Guo, Jessica Bonneau, Denis Faubert, Florian Gioanni, Alexis Vivoli, Sarah M. Muir, Soraya Hezzaz, Vincent Poitout, and Mathieu Ferron

Vitamin K-dependent carboxylation regulates Ca2+ flux and adaptation to metabolic stress in β-cells

J.L. and K.G. are listed as co-first authors of this manuscript. Written consent of J.L. to use the manuscript in this thesis has been attached. K.G. performed the experiments and data analysis and contributed to the creation of figure 5, 6, 7, S6, and S7. K.G. also designed the experiments presented in figure 6, 7, and S7. J.L. and M.F. conceived the study, designed the experiments, and initiated the project. J.L., D.F. and M.F. collected and analyzed data. J.B., F.G., S.M.M., and S.H. collected data. A.V. and V.P. prepared islet cDNA from rats infused with glucose. M.F. and J.L. wrote the manuscript, and all authors commented and contributed to editing the final version.

Chapter 3.

Kevin Guo, Giada Ostinelli, Julie Lacombe, Laura Quirion, Jonathan Boulais, Denis Faubert, Jean-Francois Cote, Guy A. Rutter, and Mathieu Ferron

Endoplamic reticulum Gla protein (ERGP) is a novel vitamin K-dependent protein regulating ER calcium homeostasis and beta-cell coordination

K.G. contributed to experimental design and collected and analyzed the data in figure 1, 3, 4, 5, 6, and 7. K.G wrote the manuscript with input from M.F. and organized the figures. M.F. contributed to the design of experiments in all figures. G.O. and G.R. contributed to the

experimental design and analyzed the data in figure 4. J.L. contributed to the design and collected and analyzed the data in figure 2 and generated the *Ggcx*^{ff}*;Ins1-Cre* mice used in figure 3 and 4. L.Q. and J.F.C. generated the cell lines used in figure 6 and 7 and contributed to experimental design. D.F. collected and analyzed data for figure 6 and 7.

Chapter 2 is published in *Cell Reports*. Permission to use the manuscript in this thesis has been granted by the publisher (Cell Press) under the terms of the Creative Commons non-commercial share alike licenses (4.0). Chapter 3 is in preparation for publication.

List of tables and figures

2. Chapter 2
    a. Figure 1: Vitamin K-dependent gamma-carboxylation machinery is active in islets and beta cells
    b. Figure 2: GGCX is necessary for the maintenance of an adequate beta cell mass in adult mice
    c. Figure 3: Pancreas or beta cell specific deletion of *Ggcx* compromises insulin secretion in response to high fat diet
    d. Figure 4: Gamma-carboxylation protects beta cells from ER stress induced cell death and is regulated by glucose
    e. Figure 5: ERGP is a gamma carboxylated protein expressed in beta cells
    f. ERGP gamma carboxylation regulates Ca^{2+} flux by modulating STIM1/Orai1 interaction
    g. Figure 7: Increased SOCE and basal cytosolic Ca^{2+} in *Ggcx*- deficient beta cells cause impaired fasting hyperinsuliemia
3. Chapter 3
    a. Figure 1: SOCE and glucose stimulated Ca^{2+} flux is elevated in semi-dispersed beta cells isolated from $Asph^{LacZ/LacZ}$ mice
    b. Figure 2: $Asph^{LacZ/LacZ}$ mice do not have significantly altered glucose tolerance or glucose stimulated insulin secretion (GSIS) compared to WT mice
    c. Figure 3: Beta cell specific knockout of GGCX increases the period of whole islet Ca^{2+} ocillations
    d. Figure 4: Beta cell specific knockout of GGCX reduces islet connectivity and coactivity

e. Figure 5: ERGP-miniTurbo fusion proteins generated and validated for use in TurboID screen
f. Figure 6: ERGP specific interactors modulated by ER Ca^{2+} depletion with thapsigargin identified with miniTurbo
g. Figure 7: ERGP interacts with proteins involved in ER Ca^{2+} regulation, unfolded protein response (UPR), and cell-cell signaling

4. Chapter 4
    a. Figure 1. (left) Western blot depicting STIM1 biotinylated by ERGP-mT in the presence or absence of thapsigargin. Cells expressing ERGP-mT and transiently transfected with GGCX and VKORC1 and cultured in the presence or absence of vitamin K (22μM) overnight. Cells were then treated with biotin (50μM) and thapsigargin (1μM) or just biotin for 15 minutes before lysis and analysis. (right) Quantification of biotinylated STIM1 normalized to total STIM1 from the input (n=3). * $p < 0.05$, *** $p < 0.001$, **** $p < 0.0001$
    b. Figure 2. (left) Western blot of islet extracts taken from *Ins1-Cre*, *ERGP^{ff},* and *ERGP^{ff};Ins1-Cre* mice. (right) Quantification of bands corresponding to ASPH and ERGP normalized to actin expressed as fold change of *Ins1-Cre*

List of abbreviations

Akt – Ak strain transforming (protein kinase B)

ASPH – aspartyl/asparaginyl beta-hydroxylase

CHOP – C/EBP homologous protein

CRAC – calcium release activated channels

ER – endoplasmic reticulum

ERGP – endoplasmic reticulum gla protein

ERK – extracellular signal regulated kinase

FSP1 – ferroptosis suppressor protein 1

G6P – glucose 6 phosphate

GCK – glucokinase

GGCX – gamma-glutamyl carboxylase

Gla – gamma-carboxyglutamic acid

GLP-1 – glucagon like peptide 1

Glu – glutamic acid

GLUT1 – glucose transporter 1

GLUT2 – glucose transporter 2

GLUT4 – glucose transporter 4

GRD – glu rich domain

GRP78 – Glucose regulated protein 78

GSIS – glucose stimulated insulin secretion

GTT – glucose tolerance test

HbA1c – glycated hemoglobin

IP_3 - inositol 1,4,5-trisphosphate

IP_3R – IP_3 receptor

IRS – insulin receptor substrate

ITT – insulin tolerance test

JNK – c-Jun N-terminal kinases

LC-MS/MS – liquid chromatography tandem mass spectrometry

MAPK – mitogen activated protein kinase

MGP – Matrix Gla protein

MODY – mature onset diabetes of the young

mTORC1 – mammalian target of rapamycin complex 1

NFAT – nuclear factor of activated T cells

OxPhos – oxidative phosphorylation

PEP – phosphoenolpyruvate

PI3K – phosphoinositide 3-kinase

PK – pyruvate kinase

PLC – phospholipase C

PTPN1 – protein tyrosine phosphatase non-receptor type 1

qGPCR – Gq-protein coupled receptor

S6K – S6 kinase

SAM – sterile-a-motif

SERCA – sarcoplasmic reticulum calcium ATPase

SHC – Src homology and collagen family

SOAR – STIM-Orai activating region

SOCE – store-operated calcium entry

SOCS2 – suppressor of cytokine signaling 2

STIM1 – stromal interaction molecule 1

STIM2 – stromal interaction molecule 2

T1D – type 1 diabetes

T2D – type 2 diabetes

TAM receptors – Tyro3, Axl, Mer receptors

TRPC – transient receptor channel

UPR – unfolded protein response

VKORC1 – vitamin K oxidoreductase complex 1

VKORC1L1 – vitamin K oxidoreductase complex 1 like 1

XBP1 – X-box binding protein 1

Chapter 1. Introduction

1.1. The diabetes epidemic

Diabetes, or diabetes mellitus, is a class of diseases characterized by a deregulation of blood glucose, resulting in persistently elevated blood glucose, or hyperglycemia, and subsequent excessive thirst and urination as the body attempts to expel excess glucose. Insufficient production and sensitivity to insulin, the primary hormone that signals glucose uptake from the blood, underlie this disease [1]. To be considered diabetic, a person must present with a fasting blood glucose level of higher than 7mmol/L on two separate tests. In contrast, normal fasting blood glucose is around 5.6mmol/L. Even following a meal, a blood glucose level higher than 11.1mmol/L also suggests diabetes. Another diagnostic tool for diabetes is the measurement of glycated hemoglobin (HbA1c) which forms when glucose interacts with hemoglobin in the red blood cells. As red blood cells turn over once every 2-3 months, HbA1c measurement serves as an indicator of blood glucose levels over the past 2-3 months. An HbA1c reading of greater than 6.5% on two separate tests is sufficient to diagnose diabetes [2].

Diabetes has witnessed a staggering rise in prevalence worldwide, making it one of the most significant global public health concerns of our time. Five hundred and thirty-seven million adults aged 20-79 were living with diabetes in 2021. This number is projected to rise to 643 million by 2030 and 783 million by 2045. Poorly treated diabetes accounts for an estimated 1.5 million deaths globally each year (Figure 1) [3]. In addition to those living with diabetes, an estimated 1 in 3 adults in the US alone are living with prediabetes, where blood glucose levels are persistently elevated above normoglycemia but not enough to warrant a diabetes diagnosis. Despite this, people with prediabetes already have an elevated risk of cardiovascular disease,

stroke, and of course the eventual development of diabetes [4].

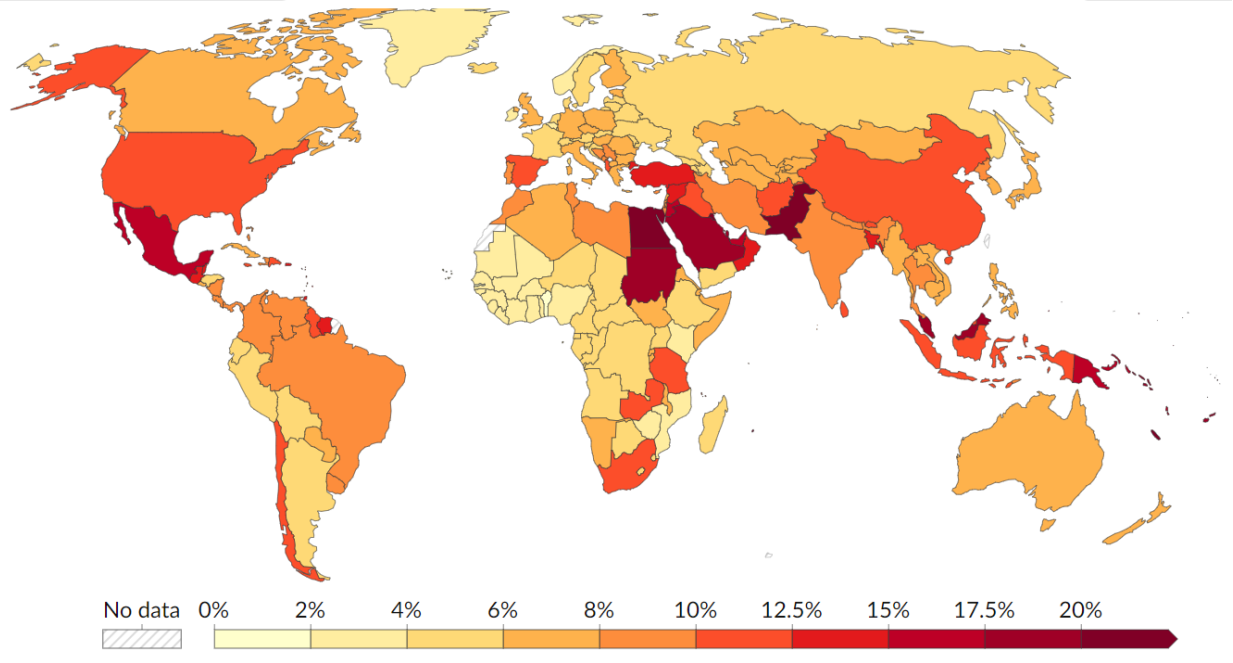

Figure 1. Percentage of population living with diabetes by country [3]

1.2. Diabetes types and disease complications

The two main types of diabetes are type 1 diabetes (T1D) and type 2 diabetes (T2D). T1D is caused by autoimmune destruction of the insulin-producing pancreatic beta-cells, the body's only source of insulin. While sensitivity to insulin remains intact, the lack of insulin production results in the development of diabetes. T1D accounts for 5-10% of all cases of diabetes and most commonly first manifests in patients younger than 20 years, but may also appear in adulthood [5]. In cases where insulin signaling is completely absent, as in T1D, failure to uptake glucose from the blood not only leads to chronic hyperglycemia but will also render glucose storage impossible since all excess glucose is expelled in the urine. Without glucose stores, the body is entirely dependent on fat stores. Since triglycerides are unable to cross the blood-brain barrier, they must be broken down into ketone bodies to be used by the central nervous system.

Unfortunately, the buildup of ketone bodies can critically lower the pH of the blood leading to diabetic ketoacidosis, a potentially fatal condition [6].

T2D is the most common form of diabetes, accounting for around 80% of all cases of diabetes. Classically, T2D develops as a result of chronic hyperinsulinemia eventually resulting in peripheral insulin resistance, a condition where target tissues become desensitized to insulin signaling [7]. Excessive consumption of foods high in sugar and fats will cause increased secretion of insulin to clear excess glucose from the blood and maintain normoglycemia. Lack of exercise, genetic factors, and advanced age can also speed the progression of insulin resistance. Increasing insulin resistance in turn drives further hyperinsulinemia as more insulin is secreted to meet glucose clearing demands. This vicious cycle has been proposed to underlie the development of metabolic disorder, obesity, and T2D [8]. In addition to insulin resistance, clinical evidence points towards the necessary presence of beta-cell dysfunction for T2D to fully develop [9, 10]. Unlike T1D, the average age of diagnosis for T2D is around 45 years old, owing to the gradual nature of the disease's development trajectory [11]. The work of this thesis will focus primarily on T2D, which is further discussed in later sections.

Other notable types of diabetes are gestational diabetes, a diabetic condition affecting some pregnant women which may improve or resolve after delivery [12], and mature onset diabetes of the young (MODY), a form of diabetes that presents similarly to T2D but manifests before the age of 30 [13]. Diabetes can also be caused by monogenetic mutations which lead to defects in insulin function, like mutations in the insulin or insulin receptor gene itself, or any disease that causes extensive damage to the whole pancreas; such as, chronic pancreatitis or cystic fibrosis [14, 15]. Even in cases where insulin signaling remains partially intact, as in T2D, MODY, and gestational diabetes, the disease is still associated with numerous complications.

Patients with diabetes are 2 to 4 times more likely to develop cardiovascular diseases with around 75% of people living with diabetes ultimately succumbing to coronary artery disease [16]. Diabetes is also associated with peripheral neuropathies, as chronic high glucose destroys nerves in the extremities [17]. It can also lead to nerve damage of the heart, contributing to cardiac arrhythmia and increasing the risk of death from cardiac arrest as the patient will unable to feel the normally associated chest pain [18]. The need to constantly filter glucose from the blood to the urine can also lead to chronic kidney disease and end-stage renal failure [19]. Increased blood viscosity caused by hyperinsulinemia can also damage microvasculature throughout the body, leading to vision loss [20].

1.3. The function of insulin

Insulin is produced by beta-cells in the islets of Langerhans, spherical cell clusters found in the pancreas that conduct the endocrine functions of the pancreas. The role of the pancreas in blood glucose regulation was first recognized in 1889 when the removal of the pancreas from a dog was observed to cause severe and fatal diabetes. Later in 1921, the landmark discovery and isolation of insulin for use in the treatment of T1D transformed the disease from what was essentially a death sentence to a manageable condition [21]. Insulin is secreted from the beta-cells into the blood stream in response to elevated blood glucose. It will then bind to insulin receptor present on the surface of effector cells, resulting in the translocation of the glucose transporter GLUT4 to the cell surface, allowing the uptake of glucose out of the bloodstream and into the cell [22].

Beyond its function in regulating blood glucose levels, insulin is also one of the body's primary signals for nutrient abundance, stimulating numerous anabolic pathways to promote energy storage. In the liver, insulin signaling inhibits gluconeogenesis and stimulates glycogen synthesis and lipogenesis, promoting energy storage [23]. Insulin signaling also promotes glycogen synthesis in skeletal muscle tissue and lipogenesis in adipose tissue. It also stimulates the intake of amino acids into the muscle and inhibits lipolysis in adipose tissue. Insulin signaling also stimulates the differentiation and growth of skeletal muscle and adipose tissue [24]. Insulin signaling also regulates the energetic state of the body by promoting satiety. It may do so by inhibiting the expression of appetite stimulating neuropeptides, such as neuropeptide y, in the arcuate nucleus of the hypothalamus [25].

The insulin receptor is a transmembrane homodimer composed of two alpha subunits and two beta subunits linked by disulfide bonds. Upon binding of insulin to the extracellular alpha subunits, the receptor undergoes conformational changes, leading to autophosphorylation of tyrosine residues within the intracellular beta subunits and the phosphorylation of the insulin receptor substrate (IRS) proteins [22]. This activation initiates a cascade of intracellular signaling events via several downstream effectors; such as, PI3K, mTORC1, and SHC. One major pathway involves the activation of phosphoinositide 3-kinase (PI3K), leading to the phosphorylation of protein kinase B (Akt). Akt activation is responsible for many of the energy storage functions of insulin; such as, translocation of GLUT4, stimulation of glycogen synthesis, and inhibition of gluconeogenesis [26]. Another important downstream effector of the insulin receptor is the mitogen-activated protein kinase (MAPK) pathway, which regulates growth, proliferation, and differentiation, processes essential for insulin's role in expanding muscular and adipose tissue

[27]. Recently, it was also discovered that endocytosis of the insulin receptor can regulate its function [28].

Insulin resistance occurs in part due to negative feed back within the insulin receptor signaling cascade. mTORC1 will activate S6 kinase (S6K) which subjects IRS1 to serine phosphorylation, targeting it for degradation [29]. Insulin receptor autophosphorylation can also be reversed via the action of the phosphatase PTPN1 and its kinase function inhibited by SOCS2. There is also evidence that inflammatory cytokines and metabolic overload leading to excessive reactive oxygen species (ROS) production will drive the activation of stress induced serine kinases like ERK, JNK, mTOR, and S6K, leading to the serine phosphorylation and degradation of IRS [30].

1.4. Insulin resistance and beta-cell decompensation in the development of T2D

As pre-diabetic individuals become increasingly insulin resistant, the beta-cells are initially able to compensate by increasing insulin secretion. Longitudinal studies following individuals who eventually develop T2D show that increased insulin secretion is initially able to maintain blood glucose at normoglycemic levels, but begin to show a decline in insulin secretion once fasting blood glucose levels surpass the upper limits of normoglycemia, which is around 5.5mM [31]. Beta-cells initially compensate for increased peripheral insulin resistance through increased glucose and fatty-acid metabolism [32, 33], and increased insulin expression and production [34]. However, in the case of T2D, these compensation mechanisms are eventually overwhelmed, and beta-cell dysfunction and death ensue (Figure 2) [35]. Analysis of post-mortem beta-cell mass found that obese individuals with T2D had a 63% reduced beta-cell mass when compared to weight matched individuals without T2D. This difference in beta-cell mass

was associated with increased markers of apoptosis, while no change in proliferative markers was seen [36].

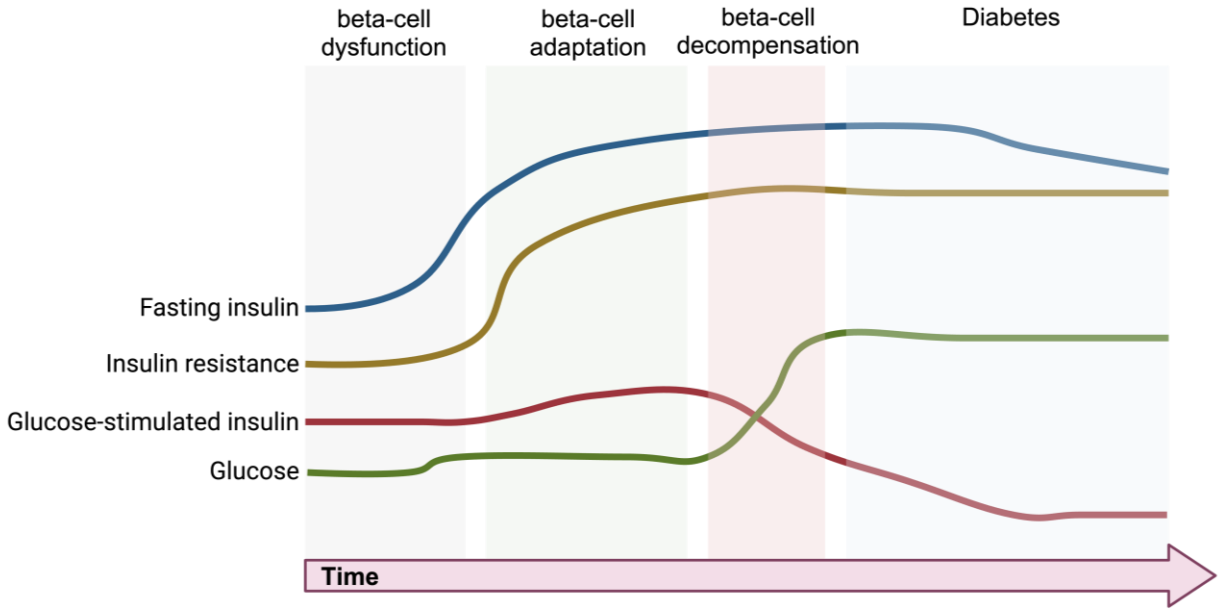

Figure 2. Progression of T2D from insulin resistance to beta-cell failure [37]

Insulin resistance is often associated with the excessive consumption of fatty, processed foods and lack of sufficient exercise, leading to weight gain and eventual obesity. Previously thought to merely be a consequence of excess sugar and fat intake, there is now increasing evidence that obesity and hyperinsulinemia form a vicious cycle whereby excessive insulin secretion can lead to increased appetite and glucose dysregulation leading to greater insulin resistance [38]. Loss of function mouse models partially lacking insulin gene expression via inactivation of one of the two mouse insulin genes are unable to sustain hyperinsulinemia normally seen when fed a high fat diet and were subsequently protected against obesity [39]. Clearly, not all obese or prediabetic individuals go on to develop T2D, exposing the multifaceted nature of this disease [40].

Numerous genetic factors are associated with the risk of developing T2D. The probability of eventually developing T2D is 40% for individuals with one parent with T2D and 70% for individuals where both parents have T2D [41]. While monoallelic gene variants causing T2D are rare, linkage studies, candidate gene screens, and genome wide association studies have identified numerous genes associated with an elevated risk of developing T2D. Many of these genes are directly involved in insulin secretion and signalling; such as, insulin receptor substrate 1 and 2 (*IRS1*and *IRS2*) and *KCNJ11*, the gene encoding the ATP sensitive potassium channel involved in the insulin secretion cascade. However, many genes are not directly involved in insulin signalling and instead are thought to increase the risk of T2D through their effects on beta-cell functioning; such as, *TCF7L2* a transcription factor that is a member of the Wnt signalling pathway which is involved in beta-cell differentiation [42]. Environmental factors also play an essential role in differing individual risks for T2D, as evidenced by the observation that individuals have an only 70% chance of developing T2D if their identical, monozygotic twin has T2D [43]. One such key environmental factor is differences in the nutritional makeup of the food consumed. In this study, we will focus on the role of vitamin K in the development of T2D.

1.5. Vitamin K dependent gamma-carboxylation and the functions of known vitamin K dependent proteins

Vitamin K is a group of fat-soluble molecules which all contain a functional naphthoquinone group and varying hydrocarbon side chains [44]. There are two main classes of vitamin K: phylloquinone or vitamin K_1 which has a primarily saturated hydrocarbon side chain, and menaquinone or vitamin K_2 which has an unsaturated side chain. Dietary vitamin K_1 comes primarily from leafy greens while vitamin K_2 is found in a variety of fermented foods and animal products, most notably natto [45]. While there exists some evidence that vitamin K_2 has a

specific role in regulating bone metabolism and density and may have added beneficial effects due to its longer half-life and effect on steroid and xenobiotic receptors in osteoblasts to promote extracellular matrix formation [46-48], the role of vitamin K in gamma-carboxylation is dependent on its functional naphthoquinone group. A synthetic form of vitamin K containing only the naphthoquinone group, called menadione or vitamin K_3, is used to supplement pet food and animal feed. Vitamin K_3 is the only form of vitamin K with known overdose symptoms, causing jaundice and in severe cases liver failure, suggesting that the side chains may be essential for the transport, storage, and clearance of naturally occurring vitamin K (Figure 3) [49].

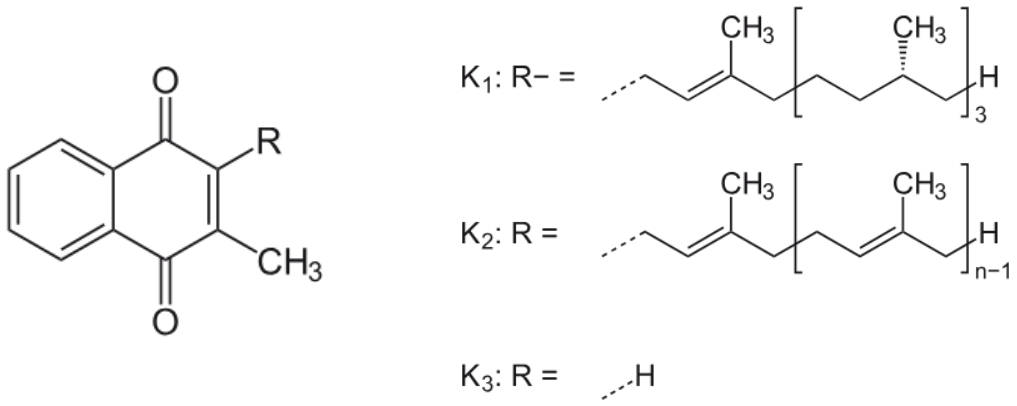

Figure 3. Naphthoquinone group shown on the left with different functional groups (R) characteristic of each type of vitamin K

Vitamin K is essential for the post translation modification known as gamma-carboxylation. Gamma-carboxylation involves the addition of an extra carboxylic acid group onto the gamma carbon of glutamic acid (Glu) residues, converting them into gamma-carboxyglutamic acid (Gla) residues [50]. In the cell, dietary vitamin K, which is in its quinone form, is reduced into its active hydroquinone form by vitamin K oxido reductase 1 (VKORC1). Vitamin K is then used as a cofactor by the enzyme gamma-glutamyl carboxylase (GGCX), an

ER resident transmembrane protein which catalyzes the conversion of Glu to Gla residues in specific ER proteins, oxidizing vitamin K into an epoxide form where it can be reduced back into its quinone form before being activated into its hydroquinone form again by VKORC1 (Figure 4). Gamma-carboxylation can be abrogated by disrupting this cycle through the pharmacological inhibition of VKORC1 by warfarin, a commonly used anti-coagulant drug [51]. Canonically, GGCX recognizes its substrates via a recognition sequence [FL]-X(5)-[GA]-X(3)-[ILV]-X(1,5)-R-X(0,2)-R] found on a propeptide immediately preceding the region containing the Gla residues [52-55].

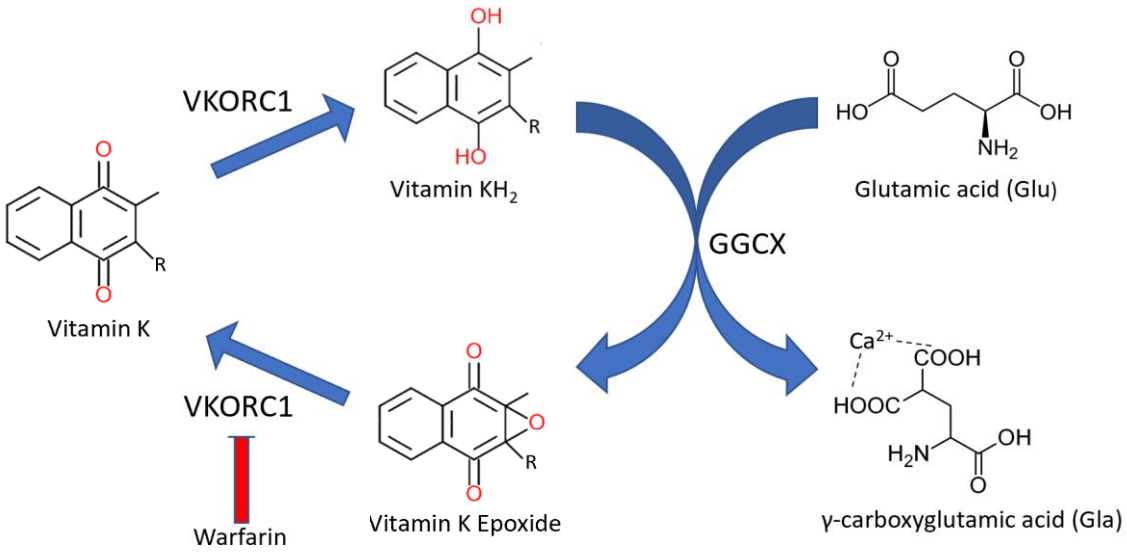

Figure 4. Schematic depicting the vitamin K cycle and gamma carboxylation

While GGCX is the only known gamma-carboxylase enzyme, VKORC1 is not the only protein known to reduce vitamin K. Vitamin K oxidoreductase complex 1 like 1 (VKORC1L1) is a paralogue of VKORC1 which can also reduce vitamin K into its active form and rescue the gamma-carboxylation of essential clotting factors when it is overexpressed in the livers of mice lacking VKORC1 [56]. The function of VKORC1L1 is not completely redundant with

VKORC1, as there is evidence that VKORC1L1 is a potent suppressor of ferroptosis, an iron-dependent mechanism of cell death [57]. The function of VKORC1L1 converges with ferroptosis suppressor protein 1 (FSP1), a protein initially identified as an inhibitor of ferroptosis that was recently discovered to also be able to reduce vitamin K into its active form [58]. This presents a dual function of vitamin K: in the gamma-carboxylation of specific ER proteins, and the suppression of ferroptosis. Vitamin K may also play a direct role in protecting against oxidative stress induced cell death, as evidenced by its ability to reduce the death of cells that are depleted of glutathione, an important cellular antioxidant. Importantly, this protective effect was not abrogated by warfarin, suggesting that it is independent of gamma-carboxylation [59].

Vitamin K was initially discovered to be essential for proper blood coagulation and the functioning of the clotting factor prothrombin, which lead to the vitamin's namesake *Koagulationvitamin* or vitamin K [60, 61]. Consequently, the first gamma-carboxylated protein identified was prothrombin [62], followed by the other clotting factors, factor VII, factor IX, and factor X [63]. Gamma-carboxylation was also found to be essential for the function of two anti-coagulant proteins: protein C and protein S [64]. The known roles of vitamin K expanded beyond blood coagulation when osteocalcin (aka. bone Gla protein) was discovered to be gamma-carboxylated [65]. Initially thought to be involved in bone development and calcification, osteocalcin was later characterized as a bone-derived hormone that regulates glucose metabolism. It is produced by osteoblasts then trapped in the calcium-rich, hydroxyapatite matrix of the bone via their Gla resides [66]. Adrenaline, insulin, and bone remodelling events will trigger demineralization of the bone by osteoclasts which create acidic (<4.5pH) bone resorption lacuna. Osteocalcin will also be decarboxylated in these lacunae and released into the bloodstream where it will promote insulin secretion in beta-cells and trigger the release of

adiponectin (which increases sensitivity to insulin) in fat cells [67, 68]. Matrix Gla protein (MGP) was discovered shortly after osteocalcin as another Gla protein that is not involved in coagulation [69]. MGP plays a vital role in regulating tissue calcification, as evidenced by the overcalcification of arteries and cartilage in mice lacking MGP [70]. In humans, mutations in MGP are linked to Keutel syndrome, a disease characterized by abnormal cartilage calcification, peripheral pulmonary stenosis, and midfacial hypoplasia [71].

1.6. Vitamin K intake protects against the development of T2D

The meteoric rise in obesity and T2D has largely been blamed on the widespread consumption of highly processed, fatty and sugary foods, such as those purchased from fast food restaurants. Since the 1990s, global obesity rates have more than doubled [72]. While rich in calories from fats and carbohydrates, diets full of processed foods are also poor in micronutrients. A cross sectional study in Brazil found a significant correlation between the consumption of ultra-processed foods and micronutrient insufficiency in children [73]. Despite consuming excessive calories, morbidly obese patients awaiting bariatric surgery often report vitamin and mineral deficiencies [74]. Such micronutrient deficiencies may contribute to the inability of beta-cells to adapt to increased insulin demand and their eventual failure and apoptosis [75].

Recent evidence has suggested that increased dietary vitamin K intake may protect against the development of T2D. In a study involving over 50,000 participants in Denmark, researchers found that individuals with the highest vitamin K_1 intake had a 31% lower risk of developing diabetes compared to those with the lowest median intake, which was about 3.5 times

less than the high intake group. Importantly, vitamin K_1 intake was linearly correlated with a decreased risk of developing diabetes even after correcting for potentially confounding variables, such as age, sex, physical activity, socioeconomic status, education, alcohol intake, and smoking status (Figure 5) [76]. Earlier studies done on different cohorts reported similar findings, with increased vitamin K_1 intake leading to reduced hyperglycemia [77] and a reduced risk of developing T2D [78-80]. This effect is also seen on a genetic level where a Mendelian randomization study found genetic markers associated with higher circulating levels of vitamin K_1 to also be associated with a lower risk of developing T2D [81]. In patients who already have T2D, increasing vitamin K_2 intake was associated with lower levels of glycated hemoglobin, a marker of chronic hyperglycemia, and fasting glucose [82, 83]. A study in rats showed that vitamin K_1 supplementation improved glycemic indices following pharmacological destruction of beta-cells by streptozotocin [84]. These studies suggest that vitamin K supplementation may protect against and be used in the treatment of T2D. Recent clinical studies have also shown an elevated risk of developing T2D in patients taking warfarin, strengthening the role of vitamin K and gamma-carboxylation in protecting against the development of diabetes [85, 86]. In this thesis, we detail our work uncovering the molecular mechanism through which vitamin K elicits this protective effect.

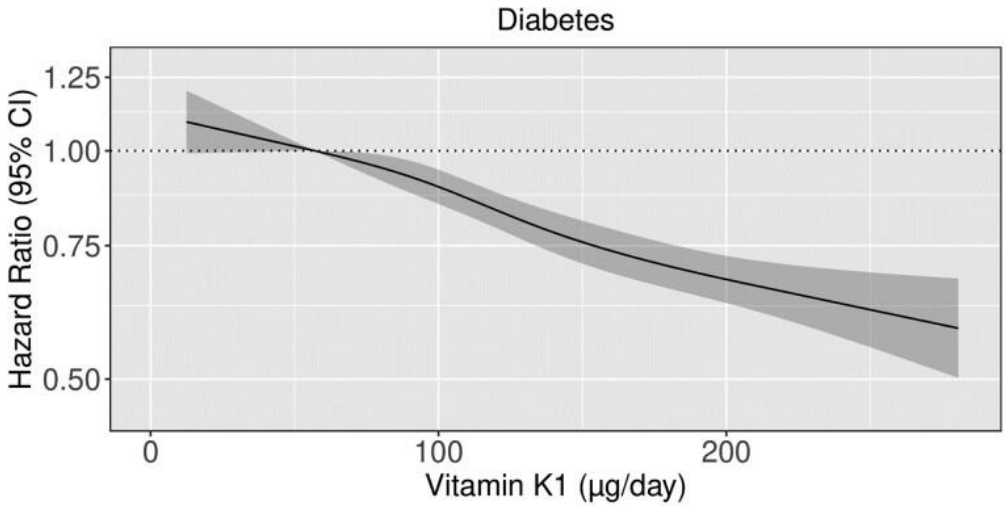

Figure 5. Hazard ratios from Cox proportional-hazards model with restricted cubic spline curves describing the association between vitamin K_1 intake (µg/day) and incident of diabetes [76]

1.7. Mechanisms and regulation of beta-cell insulin secretion

The process by which beta-cells secrete insulin is finely tuned, responding to fluctuations in blood glucose levels. Within murine beta-cells, glucose sensing is facilitated by the glucose transporter GLUT2, enabling the entry of glucose. Unlike the other GLUT transporters (GLUT1, 3, and 4) which have a Km of about 2-5mM, GLUT2 has a comparatively higher Km of 15-20mM. This causes glucose entering the beta-cell to increase in a more linear manner as extracellular glucose increases, allowing a more finely tuned response to blood glucose levels (Figure 6) [87]. Once inside the beta-cell, glucose exit is blocked via the first step of glycolysis: the conversion of glucose to glucose 6 phosphate (G6P) by glucokinase (GCK), which renders it no longer able to pass through any GLUT transporters. It has been hypothesized that GCK plays an essential role in every glucose sensing tissue, ranging from islet cells to hepatocytes and hypothalamic neurons, by generating a unidirectional flux of glucose into glucose sensing cells [88]. After the glucose is converted to G6P by GCK, it enters glycolysis to be transformed into

pyruvate then acetyl-CoA to generate ATP through oxidative phosphorylation (OxPhos), increasing the ATP/ADP ratio.

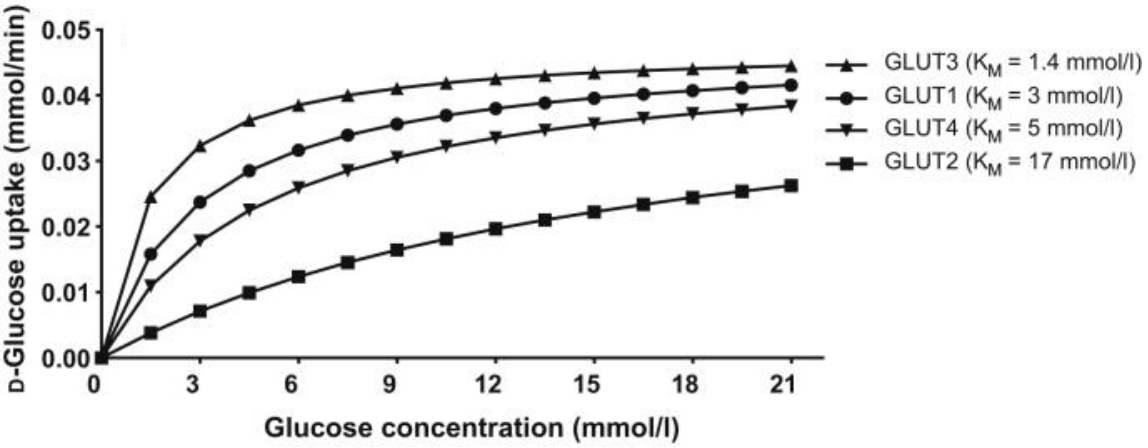

Figure 6. Predicted extracellular glucose concentration vs. glucose uptake for each of the human GLUT transporters [89]

The rise in ATP levels and fall in ADP triggers the closure of ATP-sensitive potassium (K^+ ATP) channels on the beta-cell membrane, leading to membrane depolarization and subsequent opening of the voltage gated calcium channels, allowing calcium to rush into the cytosol [90, 91]. The calcium ions will then trigger exocytosis of the insulin granules. This pathway is considered to be the primary mechanism by which glucose triggers insulin secretion [92]. However, it has since been proposed that the initial closure of K^+ ATP channels is dependent on the ATP generated from pyruvate kinase (PK) via metabolizing phosphoenolpyruvate (PEP) to pyruvate, with the sustained closure of the K^+ ATP channels driven by ATP generated from OxPhos. This allows beta-cell insulin release to be driven by both the cell's overall metabolic state as well as the presence of glucose metabolites, though this remains controversial [93].

Evidence for this is provided by the fact that insulin secretion can be stimulated by metabolites which can enter the citric acid cycle, be metabolized to increase oxaloacetate levels, and be converted back into PEP through the action of PEP carboxykinase; such as, glutamine, alpha-ketoisocaproate, and pyruvate [94-96]. However, when beta-cell ATP levels are increased by methyl-succinate, a metabolite that directly feeds complex 2 and cannot raise PEP levels, insulin secretion is not stimulated [97]. Importantly, allosteric activation of PK via the glycolytic metabolite fructose 1,6-bisphosphate precedes the closing of the K^+ ATP channels while increase of oxygen consumption and change in mitochondrial inner membrane potential associated with increased OxPhos is seen after initial K^+ ATP channel closure [98].

This delayed increase in OxPhos related ATP production is likely caused by an increase in ADP resulting from the energetic demand associated with insulin granule exocytosis and increased insulin production. As ATP production rises, OxPhos will then be inhibited by decreased ADP availability (Figure 7) [93]. The rising and falling of the ATP/ADP ratio will cause K^+ ATP channel closure to oscillate as well, resulting in the oscillation of cytosolic calcium entering the beta-cell [99]. Indeed, it was shown that oscillation of NADH, another product of OxPhos, in beta-cells was in phase with calcium influx oscillations [100]. Both in vivo and ex vivo, glucose stimulated insulin secretion is driven by such oscillating waves of calcium, causing insulin to be secreted in a pulsatile manner. A breakdown of coordinated islet calcium oscillation is associated with glucose intolerance [101], and the loss of insulin secretion oscillations are an early sign of progression to diabetes [102, 103].

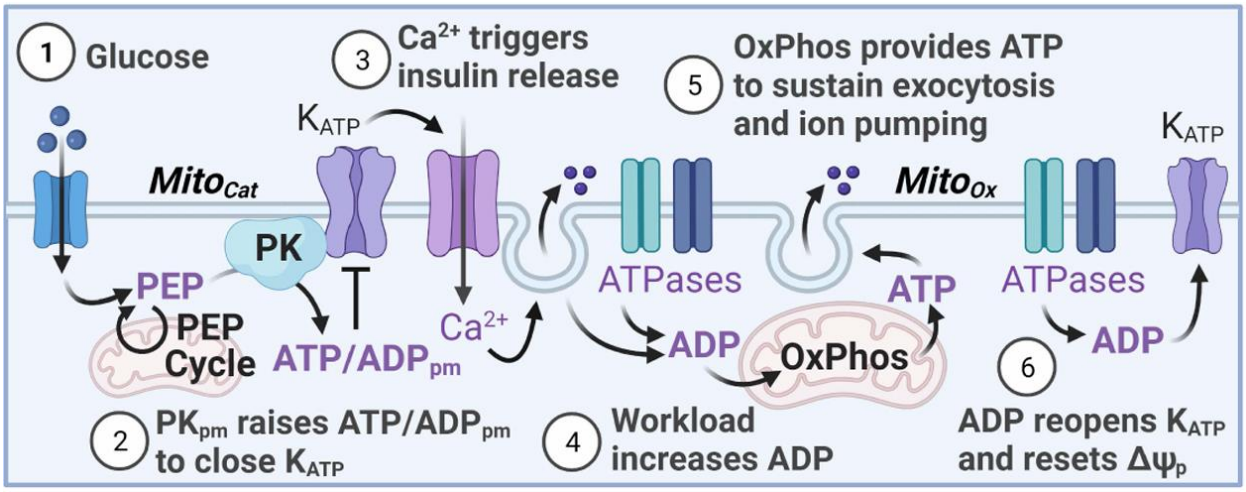

Figure 7. Model for glucose stimulated insulin release from beta-cells [93]

Beyond glucose, various factors known as incretins modulate insulin secretion. Hormones such as glucagon-like peptide-1 (GLP-1) and glucose-dependent insulinotropic peptide (GIP), released from the gut in response to nutrient ingestion, enhance glucose stimulated insulin secretion [104]. The presence of certain amino acids and free fatty acids (FFA) is also known to potentiate insulin secretion [105]. However, excess FFA exposure can cause lower ex vivo glucose stimulated insulin secretion due to lipotoxicity [106]. Additionally, neural inputs from the autonomic nervous system, particularly parasympathetic stimulation, contribute to the modulation of beta-cell activity. Insulin secretion becomes elevated for about 10 minutes following the mere sight, smell, and taste of food in anticipation of nutrient absorption. Subsequent chewing, swallowing, and gastric distension all serve to further activate the parasympathetic nervous system and elicit anticipatory insulin secretion [107].

1.8. Beta-cell coordination, connectivity, and heterogeneity: a complex micro-organ

Coordination of the aforementioned oscillating calcium waves throughout the beta-cells of an islet is essential for their proper functioning. It is known that intact, properly connected

islets are able to secrete more insulin than what would be supposed from the average insulin secretion of individual disassociated beta-cells [108]. The beta-cells of an islet are able to transmit ions between each other via gap junctions, most notably connexin 36 [109]. Gap junctions allow the passage of ions such as sodium, calcium, and zinc ions as well as the movement of ATP and ADP between beta-cells [110]. This enables the coordination of both metabolic and electrical waves and ultimately insulin secretion across the islet. Despite the fact that connexin 36 is expressed in all beta-cells, there exists heterogeneity in the apparent connectedness of each cell as cells which are in closer proximity to each other are not necessarily more synchronized [111]. This is reinforced by the fact that fluorescent protein recovery is not homogenous following photobleaching, suggesting the existence of strong connections with even more distally located beta-cells in some cells [112].

Indeed, there exists a population of highly connected beta-cells known as hub cells. These cells appear to oscillate in phase with a larger proportion of beta-cells. Optogenetic silencing of these cells results in a catastrophic breakdown of coordinated islet calcium oscillation which is reversed when the laser is turned off. Interestingly, GCK expression is significantly higher in hub cells, suggesting they may have heightened glucose sensing abilities [111]. Distinct from the hub cells, there are a population of beta-cells who are activated before the rest of the beta-cells within the islet called leader cells. As their activation precedes that of the rest of the islet, these leader cells are thought to serves as pacemakers for islet calcium oscillations. Photoablation of these cells caused a significant reduction in calcium oscillations throughout the islet whereas photoablation of random beta-cells produced no significant changes [113]. Rather than forming a homogenous cluster of cells, it is becoming increasingly clear that the heterogenous functions of beta-cells are essential for their proper coordinated functioning.

Islet wide single cell RNA sequencing of beta-cells has revealed a plethora of molecular profiles represented in a single islet. In conjunction with whole cell patch clamping, these studies have revealed distinct subpopulations with differing insulin secretion capacities as seen by measurements of single cell exocytosis [114]. Some of these differences may not exist to directly service beta-cell insulin secretion. For example, mouse models expressing less mature, low-insulin producing beta cells are more resistant to immune attack [115, 116]. Beta-cell proliferation also seem to be inversely correlated with insulin production [117]. The production and release of insulin is metabolically demanding, and beta-cells may not have the capacity to proliferate and secrete insulin simultaneously. It has been proposed that beta-cells may even be able to dedifferentiate to immature, highly-proliferative states or even transdifferentiate to other islet cell types [118, 119], adding a dynamic layer to the concept of beta-cell heterogeneity.

1.9. Calcium regulation in beta-cell endoplasmic reticulum (ER) stress

As previously described, calcium influx plays an essential role in triggering insulin secretion from beta-cells. However, the regulation of cellular calcium dynamics is also essential for protein folding and protection against endoplasmic reticulum (ER) stress. Following initial synthesis and translocation into the ER, secreted proteins like proinsulin are folded via the action of various ER lumen chaperones such as, GRP78, calnexin, calreticulin, protein disulfide isomerase, and Erp57 [120-122]. Almost all of these chaperones bind and sequester calcium, acting as a buffer for ER calcium concentrations following depletion of the ER calcium stores. In vitro evidence has shown that the activity of these chaperones is unaffected across the range of physiological ER calcium concentrations [123]. However, ER calcium concentrations associated with non-depleted ER calcium stores (~200μM) are known to be essential for the folding of

many secreted proteins [124-126]. Calcium binding ER chaperones are also known to regulate cellular calcium flux and oscillations by regulating the activity of sarcoplasmic reticulum calcium ATPase (SERCA), the ATP dependent pump which actively transports calcium into the ER [127, 128]. This activity may be essential for maintaining the ER calcium environment necessary for proper protein folding. Furthermore, luminal calcium depletion may alter ER chaperone activity by changing their spatial distribution within the organelle [129]. It is well known that prolonged ER calcium depletion will result in the activation of the unfolded protein response (UPR) and eventual ER stress induced apoptosis [130].

Activation of the UPR in beta-cells is a beneficial compensatory mechanism in its early stages, causing enhanced survival and proliferation [131]. However, left unchecked, chronic activation of the UPR in beta-cells leads to apoptosis [132]. Beta-cells taken from the islets of patients with type 2 diabetes (T2D) showed significantly higher ER density volumes as seen by electron microscopy, a sign of ER stress, as well as increased expression of markers of ER stress, such as spliced XBP-1 and CHOP, when subjected to high glucose conditions [133]. Mutations in several genes regulating UPR, such as *DNAJC, PPP1R15B, and eIF2α*, are associated with the development of diabetes [134-138]. Beta-cells are also known to modulate their ER calcium flux to mitigate ER stress. This is evidenced by increased expression of ryanodine receptor 1, an ER calcium channel which opens in response to elevated cytosolic calcium levels, following treatment with tunicamycin, a pharmacological inducer of ER stress which prevents proper folding of ER glycoproteins [139]. Importantly, tunicamycin induced ER stress increases beta-cell basal calcium levels and ER calcium refilling via store operated calcium entry (SOCE) [140].

1.10. Store operated calcium entry (SOCE)

Store operated calcium entry (SOCE) is a mechanism whereby cells replenish ER calcium stores by allowing the entry of extracellular calcium into the cytosol following ER calcium depletion. The cytosolic calcium is then available for uptake into the ER via the SERCA pump (Figure 8a). SOCE plays a vital role in calcium signal transduction, cell proliferation, and the calcium dependent activation of NFAT, a transcription factor involved in immune response and other cellular processes [141]. In beta-cells, SOCE is important in protecting against ER stress [140] and regulating insulin secretion. Pharmacological inhibition of SOCE decreases the frequency and amplitude of islet calcium oscillations and ex vivo insulin secretion—a phenotype also seen in islets taken from mice lacking STIM1 [142].

Physiologically, a key pathway by which SOCE becomes activated is following the opening of the inositol 1,4,5-triphosphate receptor (IP_3R) calcium channels. The IP_3R channels are calcium channels expressed on the ER that are opened upon binding with inositol 1,4,5-triphosphate (IP_3), allowing the efflux of calcium from the ER. IP_3 is generated following activation of phospholipase C (PLC) by Gq-protein coupled receptor (qGPCR) signaling [143]. qGPCR signaling is triggered in a myriad of cellular signaling pathways ranging from T cell activation and signaling [144] to long term potentiation of neurons [145]. IP_3R signaling is also involved in insulin secretion from beta-cells and protection against ER stress induced apoptosis [146, 147].

ER calcium depletion will trigger a conformational change in the stromal interaction molecule (STIM) proteins, causing them to oligomerize and translocate to ER-plasma membrane (PM) junctions [148]. These ER-PM junctions are visible through electron microscopy as dense puncta where the ER membrane makes direct contact with the PM (Figure 8b). Here, STIM will

interact with and open the calcium release activated channels (CRAC), allowing the influx of calcium into the cytosol [148]. Previously, it was thought that there were two family of CRAC channels: the Orai PM calcium channel proteins and the transient receptor channel (TRPC) proteins. However, recent evidence has shown that the involvement of the TRPC proteins in SOCE is dependent on the Orai proteins, suggesting that SOCE is chiefly dependent on the interaction between the STIM and Orai proteins [149].

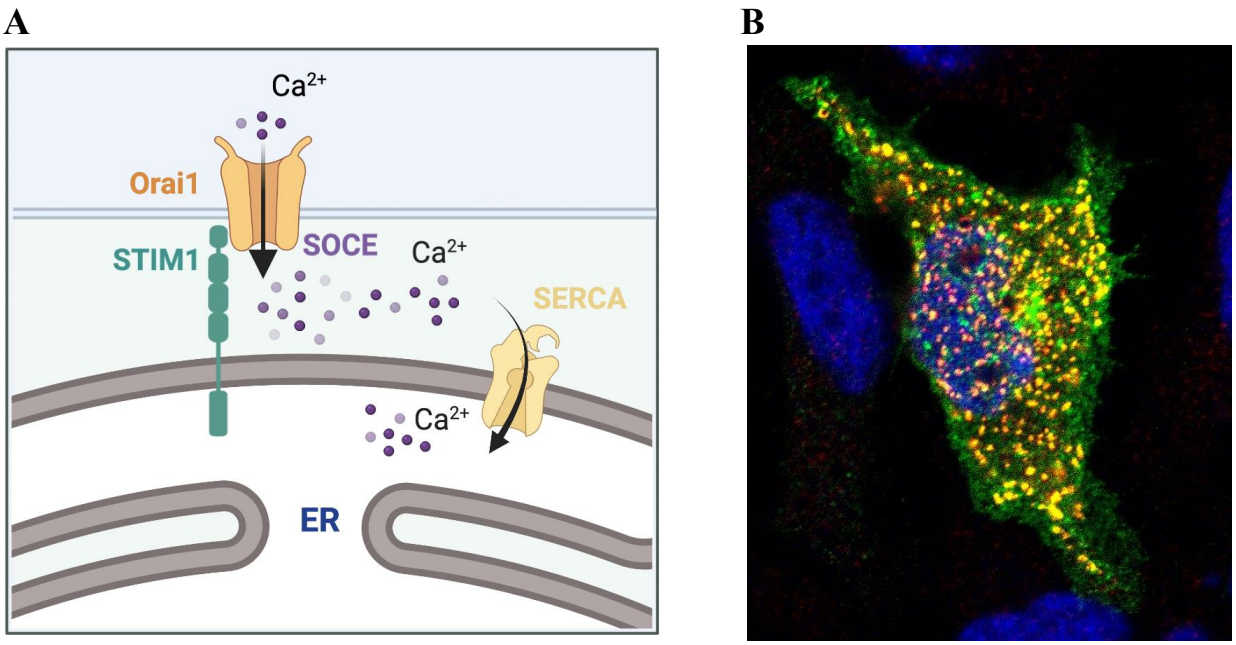

Figure 8: A) Schematic of store operated calcium entry (SOCE). B) Immunofluorescent image of STIM1 (red) and Orai1 (green) puncta in HEK293 cells following depletion of ER calcium with thapsigargin

In mammals there are two STIM paralogs, known as STIM1 and STIM2. STIM1 and 2 are coexpressed in most human tissues and commonly used mammalian cell lines like HEK293 and HeLa [150]. Both STIM proteins are type one transmembrane proteins localized to the ER and sense ER calcium levels through their near identical N-terminal ER luminal regions, which contain two calcium binding EF-hand domains and a sterile-a-motif domain (SAM). The STIM

proteins interact with the CRAC channels via their C-terminal cytosolic domains, containing two coiled-coil domains and a STIM-Orai activating region (SOAR) domain. STIM1 and 2 primarily differ in the structure of their SOAR domain, which mediates their interaction with the CRAC channels, resulting in a weaker STIM2 mediated SOCE transient when compared to STIM1(Figure 9) [151]. Knockout of only STIM2 in HEK293 cells has little effect on SOCE following ER calcium depletion by acetylcholine, whereas knockout of only STIM1 results in greatly diminished SOCE under the same conditions [152]. There is also evidence to suggest that the STIM2 ER luminal regions have a slightly lower affinity for calcium, making it more sensitive to minor changes in calcium concentrations [153]. Despite having little role in SOCE following acute ER calcium depletion, overexpression of STIM2 has been shown to elevate basal cytosolic calcium levels more than overexpression of STIM1 [154]. These evidences suggest that STIM1 is more important in triggering SOCE following acute ER calcium depletion while STIM2 plays a role in regulating basal cytosolic calcium through SOCE.

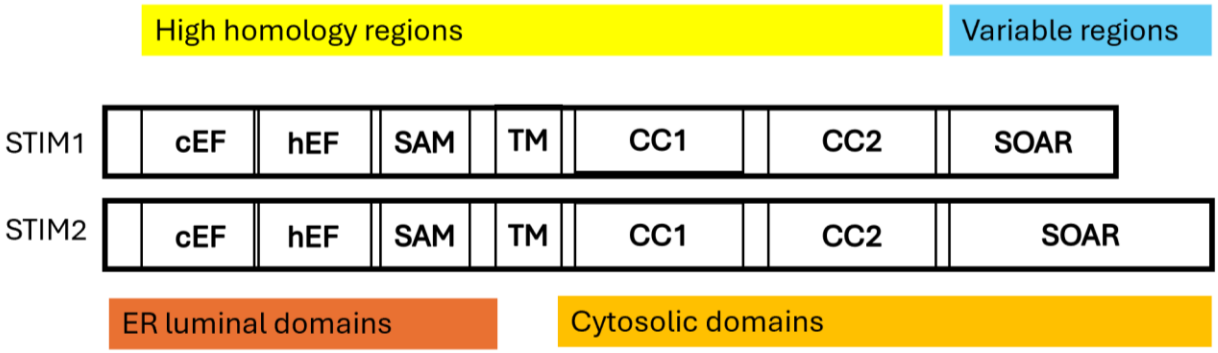

Figure 9. Structure of STIM1 and STIM2 showing their conserved EF hand domains (cEF), hidden EF hand domains (hEF), sterile-a-motif domains (SAM), transmembrane domains (TM), coil-coiled domains (CC), and variable STIM-Orai activating regions (SOAR) [151]

Fine tuning of SOCE to regulate ER calcium replenishment and basal cytosolic calcium is made more intricate by the various Orai calcium channels. There are three mammalian homologues of Orai, called Orai1, 2, and 3, which are all present on the PM. The Orai proteins all contain four transmembrane domains which hexamerize to form a central pore which is highly selective for calcium ions under physiological conditions [155]. When inactive, the Orai proteins exist as dimers as seen by stepwise fluorescent protein photobleaching of GFP tagged Orai1 and Orai3. Interestingly, these same experiments revealed the fluorescently tagged Orai constructs to only tetramerize when co-expressed with a constitutively active mutant of STIM1 [156-158]. While it is possible that the lack of apparent hexamer formation in these studies is an artifact of the fluorescent protein fusion, there is also the possibility that the different Orai homologues form mixed hexamers as the endogenous Orai proteins were not knocked out in these studies.

STIM1 and 2 have also been shown to have distinct interaction profiles with Orai1, 2, and 3. Following depletion of ER calcium with thapsigargin, an inhibitor of SERCA, the interaction between STIM1 and the Orai proteins increases to differing extents while the interaction between STIM2 and the Orai proteins does not change from their respective baseline levels, as seen by Forester resonance energy transfer (FRET) experiments [152]. These results further support the differential roles of STIM1 as the regulator of “active” SOCE following ER calcium depletion and STIM2 as the regulator of “resting” SOCE to support basal cytosolic and ER calcium levels. Consequently, when measuring SOCE, through methods such as fluorescent calcium imaging, it is important to measure both the cytosolic calcium influx following ER calcium depletion as well as basal cytosolic calcium levels.

Various other proteins have also been shown to regulate SOCE. SOCE associated regulatory factor (SARAF), an ER resident protein, is a well-established negative regulator of SOCE. It has been shown to decrease basal cytosolic and ER calcium levels via interaction with STIM2 and inhibit SOCE following ER calcium depletion with thapsigargin via interaction with STIM1 [159, 160]. Positive regulators of SOCE include CRAC regulator 2A and 2B (CRACR2A and CRACR2B), which have been shown to facilitate the proper formation of the STIM-Orai complex and whose expression is associated with elevated SOCE following depletion of ER calcium with thapsigargin [161]. Calmodulin, a well-known cytosolic calcium binding protein, has also been shown to inhibit the interaction between STIM1 and Orai1 via interaction with STIM1 when calmodulin is calcium bound [162]. Protein kinase C has also been implicated in SOCE regulation via phosphorylation of both STIM1 and Orai1. However, the mechanism by which this phosphorylation affects SOCE remains unclear [163, 164].

1.11. Products of *ASPH,* the gene locus encoding the novel gamma-carboxylated protein Endoplasmic Reticulum Gla Protein (ERGP)

In this thesis, we will detail our studies identifying Endoplasmic Reticulum Gla Protein (ERGP), a novel gamma-carboxylated protein which is encoded by the *ASPH* gene locus, located on chromosome 8 in humans and chromosome 4 in mice. The *ASPH* gene locus is named after its longest encoded product, an enzyme called aspartyl/asparaginyl beta-hydroxylase (ASPH). *ASPH* has two promoters. Promoter 1 is generally expressed across all tissues in the body while promoter 2 is activated by muscle enhancer factor 2 and 3 and is therefore specifically expressed in skeletal and cardiac muscle [165]. Promoter 1 encodes ASPH and a shorter isoform that lacks the enzymatic domain previously called junctate [165] or humbug [166], which we have renamed

ERGP due to our discovery that it is a gamma-carboxylated protein. Promoter 2 encodes junctate and junctin, proteins which may have a role in regulating cellular calcium flux [167-169] (Figure 10).

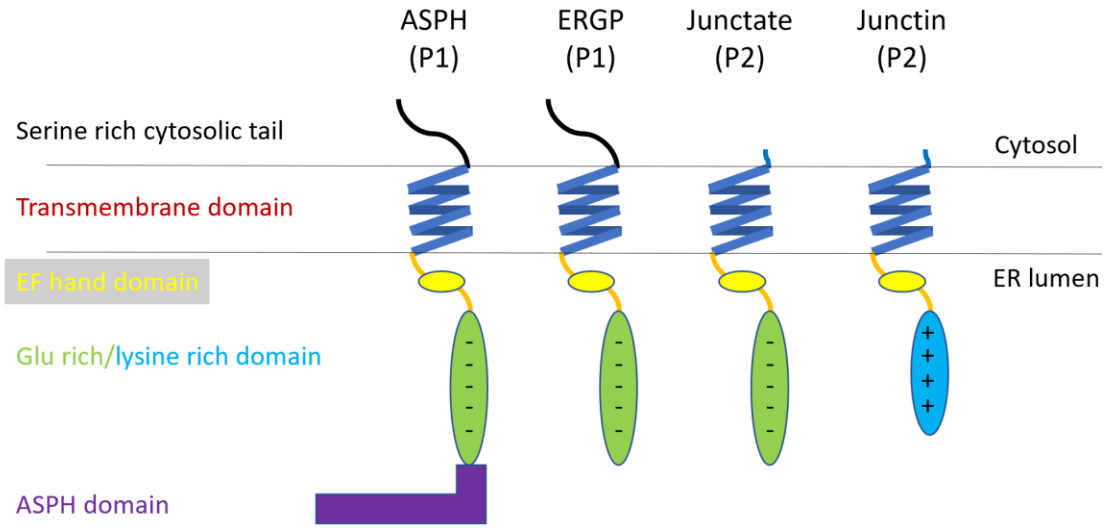

Figure 10. Known isoforms expressed by the *ASPH* gene from promoter 1 (P1) or promoter 2 (P2)

ASPH is a type 2 ER resident transmembrane protein. It has an N-terminal serine rich cytosolic tail and single transmembrane domain. These lead down into a putative calcium binding EF hand motif and a Glu rich domain containing 39 Glu residues in the ER lumen. Finally, ASPH contains a catalytic domain which uses alpha-ketoglutarate to beta-hydroxylate aspartate and asparagine residues on substrates containing a conserved sequence (CxD/NxxxxY/FxCxC) found on calcium binding EGF-like domains [166, 170, 171]. There is evidence that phosphorylation of ASPH's serine rich tail may modulate its enzymatic activity [172]. The gamma-carboxylated blood clotting proteins factor VII, factor IX, factor X, protein C, and protein S also have calcium binding EGF-like domains and are beta-hydroxylated by ASPH

[173]. However, it has been shown that inhibiting beta-hydroxylation by preventing alpha-ketoglutarate availability to ASPH with compounds like dipyridyl, o-phenanthroline, and pyridine 2,4-dicarboxylate does not affect the gamma-carboxylation nor function of the clotting factors in vitro [174].

Recently, it has been proposed that ASPH mediated beta-hydroxylation is involved in the proper folding and disulfide bond formation of the calcium binding EGF-like domains. This is based on the observation that ASPH more easily hydroxylates calcium binding EGF-like domains with improperly formed disulfide bonds [175]. ASPH has also been also implicated in the development of pancreatic and hepatic cancer where ASPH enzymatic activity promotes the oncogenic signalling activity of Notch, which is a calcium binding EGF-like domain containing protein [176, 177]. Congenital inactivation of the ASPH enzymatic domain results in Traboulsi syndrome, which is characterized by facial dysmorphism, eye abnormalities like lens dislocation, cardiac abnormalities like ventricular septal defects, and elongation of the limbs like that seen in Marfan syndrome [178, 179]. However, due to the extremely rare nature of this disease, our knowledge of Traboulsi syndrome is limited to a handful of case studies.

Junctin is the most structurally different isoform of ASPH and is expressed exclusively from P2. Junctin does not have a serine rich cytosolic tail and instead of a Glu rich domain, junctin possesses a positively charged lysine rich domain [180]. Junctin is part of a complex with triadin, calsequestrin, and the ryanodine receptor which regulates calcium efflux out of the sarcoplasmic reticulum (SR). Functionally, junctin acts as an SR lumen facing calcium sensor which bridges the interaction between calsequestrin and the ryanodine receptor to increase the probability of ryanodine receptor opening in response to cytosolic calcium when SR lumen calcium levels are higher [181]. Junctate is the second isoform encoded by promoter 2 and is

structurally similar to junctin, except that it posesses the ASPH Glu rich domain rather than the positively charged lysine rich domain. Junctate has been shown to have a role in regulating SOCE through its association with STIM1 [169]. It has also been proposed that junctate may regulate cellular calcium flux via interaction with the IP_3R channels [168]. Previously, ASPH and isoforms had no known functions in the beta-cells. In this study, we characterize the role of ERGP in beta-cells.

1.12. Hypothesis and objectives

Clinical evidence suggests that vitamin K has a role in protecting against the development of T2D [76, 78, 79, 81, 83]. However, the mechanisms underlying this effect remain unknown. Previous work has shown that beta-cell dysfunction is necessary for the development of T2D [8, 35]. Therefore, we hypothesized that vitamin K acts directly on pancreatic beta-cells to confer its beneficial effect against diabetes. Our objectives were to 1) investigate the potential role of vitamin K dependent gamma-carboxylation in beta-cell function in vivo, 2) characterize the novel gamma-carboxylated protein that mediates this effect, and 3) investigate the molecular mechanism by which this gamma-carboxylated protein elicits its effect.

To investigate the potential role of vitamin K dependent gamma-carboxylation in beta-cell function, we used a mouse model specifically lacking GGCX in the beta-cells (*Ggcx$^{f/f}$;Ins1-Cre)* and the whole pancreas (*Ggcx$^{f/f}$;Pdx1-Cre)*. These mice were subjected to a high fat diet to drive insulin resistance and hyperinsulinemia. Histological analysis were done to assess beta-cell mass and apoptosis. Furthermore, metabolic tests for glucose tolerance, glucose stimulated

insulin secretion, and insulin tolerance were done to assess the in vivo functioning of the beta-cells and peripheral insulin resistance.

Previously, no known Gla proteins expressed in beta-cells could explain the protective effect of vitamin K against diabetes. Therefore, we also aimed to identify and characterize the novel gamma-carboxylated protein that mediated this effect. In this endeavour, we used our unique pan-specific anti-Gla antibody to pull down Gla proteins from isolated islets [56]. The Gla proteins were then identified via liquid chromatography tandem mass spectrometry (LC-MS/MS), leading to the discovery of ERGP as a novel gamma-carboxlyated protein. ERGP was then characterized molecularly, with the location of its Gla residues mapped via site directed mutagenesis and LC-MS/MS. Appropriate functional assays were also used to determine the effect of gamma-carboxylation on the functioning of this ERGP; such as, calcium imaging to determine the potential effect of carboxylated ERGP on SOCE and glucose stimulated calcium flux.

Finally, we characterized the interactome of ERGP using TurboID [182]. This shed more light on the role of gamma-carboxylation in the functioning of ERGP in beta-cells, helping to better characterize the link between vitamin K and the reduced risk of developing T2D. We also examined the effect of the gamma-carboxylation of this protein on whole islet calcium oscillations, providing further insight into the molecular mechanisms underlying coordinated islet calcium oscillations.

Chapter 2: First manuscript

Vitamin K-dependent γ-carboxylation regulates Ca^{2+} flux and adaptation to metabolic stress in β-cells

Julie Lacombe[1,7,*], Kevin Guo[1,2,7], Jessica Bonneau[1,3], Denis Faubert[4], Florian Gioanni[1], Alexis Vivoli[5], Sarah M. Muir[1], Soraya Hezzaz[1], Vincent Poitout[5,6], Mathieu Ferron[1,2,3,6,8*]

[1]Molecular Physiology Research Unit, Institut de Recherches Cliniques de Montréal, Montréal, QC, H2W 1R7, Canada

[2]Division of Experimental Medicine, McGill University, Montréal, QC, H4A 3J1, Canada

[3]Programme de Biologie Moléculaire, Université de Montréal, Montréal, QC, H3T 1J4, Canada

[4]Mass Spectrometry and Proteomics Platform, Institut de Recherches Cliniques de Montréal, Montréal, QC, H2W 1R7, Canada

[5]Montreal Diabetes Research Center, Centre de Recherche du Centre Hospitalier de l'Université de Montréal (CRCHUM), Montréal, QC, H2X 0A9, Canada

[6]Département de Médecine, Université de Montréal, Montréal, QC, H3T 1J4, Canada

[7]These authors contributed equally

[8]Lead Contact

[*]Correspondence: mathieu.ferron@ircm.qc.ca (M.F.), julie.lacombe@ircm.qc.ca (J.L.)

SUMMARY

Vitamin K is a micronutrient necessary for the γ-carboxylation of glutamic acids. This post-translational modification occurs in the endoplasmic reticulum (ER) and affects secreted proteins. Recent clinical studies implicates vitamin K in the pathophysiology of diabetes, but the underlying molecular mechanism remains unknown. Here, we show that mouse β-cells lacking γ-carboxylation fail to adapt their insulin secretion in the context of age-related insulin resistance or diet-induced β-cell stress. In human islets, γ-carboxylase expression positively correlates with improved insulin secretion in response to glucose. We identify Endoplasmic Reticulum Gla Protein (ERGP) as a γ-carboxylated ER-resident Ca^{2+}-binding protein expressed in β-cells. Mechanistically, γ-carboxylation of ERGP protects cells against Ca^{2+} overfilling by diminishing STIM1 and Orai1 interaction and restraining store-operated Ca^{2+} entry. These results reveal a critical role for vitamin K-dependent γ-carboxylation in the regulation of Ca^{2+} flux in β-cells and in their capacity to adapt to metabolic stress.

INTRODUCTION

Type 2 diabetes (T2D) is a metabolic disorder characterized by insulin resistance, hyperglycemia and hyperinsulinemia.[1] Traditionally, T2D has been viewed as a disease initiated by peripheral insulin resistance ultimately resulting in pancreatic β-cell exhaustion. However, recent studies suggest that uncontrolled and excessive insulin secretion by β-cells could be the driving force that elicits peripheral insulin resistance and metabolic complications in T2D.[2, 3] Human and animal studies indicate that several factors can influence T2D susceptibility, including age, genetic variants, and diet. Many of these factors are thought to directly impact β-cell function.[4] Increased consumption of highly processed, calorie-rich but nutrient-poor food is one possible contributor to the current T2D pandemic.[5] Paradoxically, in Western countries, excess calorie intake is frequently associated with deficiencies in a number of micronutrients, including several vitamins.[6] Other studies have linked micronutrient deficiencies to an increased risk of diabetes.[7, 8] Yet, the role of micronutrients in β-cell function remains poorly understood.

Vitamin K (VK), a fat-soluble vitamin, functions as a co-factor during the γ-carboxylation reaction that converts glutamic acid (Glu) residues to γ-carboxyglutamic acid (Gla) residues in proteins transiting through the endoplasmic reticulum (ER). Two ER-resident enzymes are involved in this reaction, which together form the VK cycle: γ-glutamyl carboxylase (GGCX), and vitamin K oxidoreductase (VKORC1).[9] GGCX requires reduced VK (VKH_2) as an essential cofactor, which upon carboxylation of proteins, is oxidized to VK epoxide (VKO) and then reconverted to VKH_2 by VKORC1. The presence of this post-translational modification in proteins results in higher affinity for calcium ions (Ca^{2+}). Altogether, in vertebrates, less than

fifteen γ-carboxylated proteins have been identified so far, all of them being secreted proteins. Gamma-carboxylation is essential in the liver for the activity of several coagulation factors (e.g., prothrombin, factor IX, etc.), and in arteries and cartilage to modulate the activity of Matrix Gla Protein (MGP), which prevents extra-osseous tissue mineralization.[10, 11] Gamma-carboxylation also negatively regulates the function of osteocalcin, a bone-derived hormone with pleiotropic actions.[12, 13] Whether γ-carboxylation occurs on ER-resident proteins and regulates cellular functions in a cell-autonomous manner is currently unknown.

Clinical and genetic data suggest that VK insufficiency or reduced VK intake are associated with an increased risk of developing metabolic syndrome or T2D.[14] Two longitudinal studies found a positive association between low dietary VK intake and risk of developing T2D.[15, 16] It was also observed that 40% of morbidly obese patients are characterized by VK insufficiency and that low serum VK correlates positively with the presence of T2D in these subjects.[17-19] Finally, VK supplementation in patients with T2D significantly decreased their fasting glucose and HbA1c blood concentrations.[20, 21] These clinical studies suggest a link between VK insufficiency and the risk of developing diabetes. However, they also raise important questions regarding the mechanism by which VK protects against T2D. Does VK directly affect β-cell function? If so, what are the cellular and molecular mechanisms involved, and which γ-carboxylated protein mediates the protective effect of VK?

In the current study, we aimed at answering these questions using a combination of unique genetic, cellular, and biochemical tools we developed to study γ-carboxylation. Using loss-of-function models, we found that the inactivation of *Ggcx* impairs β-cell function in young mice

exposed to a short bout of high-fat diet (HFD), and compromises β-cell survival in older animals fed a regular diet. Additionally, we identified Endoplasmic Reticulum Gla Protein (ERGP), as a γ-carboxylated ER-resident protein that prevents Ca^{2+} overfilling by regulating store-operated Ca^{2+} entry (SOCE) in β-cells. These data demonstrate that γ-carboxylation plays a critical role in the capacity of β-cells to adapt to physiological stress and extend the cellular functions of this post-translational modification.

RESULTS

Vitamin K-dependent carboxylation occurs in islets and β-cells

To identify tissue(s) involved in the beneficial effect of VK on glucose metabolism and T2D, we examined GGCX and VKORC1 protein levels in a panel of human tissues using the ProteomicsDB resource.[22] This analysis revealed that pancreatic islets were ranked fourth and first for GGCX and VKORC1 protein expression respectively (Fig.1A), in agreement with our own data showing that *Ggcx* and *Vkorc1* genes are highly expressed in mouse islets (Fig.S1A-B). To dissect *Ggcx* and *Vkorc1* expression within mouse islets, we used fluorescence-activated cell sorting to isolate β-cells based on the expression of the fluorescent reporter protein tdTomato (Tom) conditionally expressed in the insulin-positive cells of $Ins1^{Cre/+}$; $Rosa26^{CAG\text{-}lox\text{-}stop\text{-}lox\text{-}tdTomato}$ mice. Using this strategy, we obtained a pure β-cell population (Tom+), as demonstrated by the expression of the insulin genes *Ins1* and *Ins2*, and the absence of the other endocrine cell type markers *Gcg*, *Ppy* and *Sst* (Fig.1B). Further quantitative PCR (qPCR) analyses revealed that *Ggcx* and *Vkorc1* were expressed in β-cells and other islet endocrine cells (Fig.1C). *Tabula Muris* single cell transcriptomics data[23] confirmed *Ggcx* and *Vkorc1* expression in the endocrine pancreas (Fig.S1C-D). These results agree with another set of publicly available

mouse islet transcriptomic data.[24] In addition, we found that GGCX and VKORC1 proteins are expressed at similar and higher levels respectively in purified β-cells as compared to whole islets (Fig.1D). Using γ-carboxylated GGCX (Gla-GGCX) as a readout of a functional VK cycle[25, 26], we demonstrated that carboxylation does take place in pancreatic islets and specifically in β-cells (Fig.1D). GGCX expression was also detected in the rat insulinoma cell line INS-1 832/3 and its γ-carboxylation was induced following treatment with phylloquinone (vitamin K_1; VK_1), which is absent from cell culture media and fetal bovine serum[27] (Fig.1E). To determine the extent of γ-carboxylation in vivo in islets and β-cells, we isolated islets from *Ggcx^{ff}; Pdx1-Cre* and *Ggcx^{ff}; Ins1-Cre* mice in which *Ggcx* has been inactivated specifically in the pancreas or in β-cells respectively (Fig.1F and Fig.S1E-F). Western blot analyses with a previously characterized α-Gla specific antibodies[26] revealed the presence of carboxylated proteins in islets and β-cells as demonstrated by reduced α-Gla immunoreactivity in *Ggcx^{ff}; Pdx1-Cre* and *Ggcx^{ff}; Ins1-Cre* islets (Fig.1F). Finally, GGCX expression was also detected in human islets and culturing them with VK_1 significantly increased protein γ-carboxylation. Conversely, warfarin, an inhibitor of VK oxidoreductase activity[28], reduced it (Fig.1G-H, Table S1). We also observed that in the presence of warfarin, GGCX migrates faster on SDS-PAGE because of its incomplete γ-carboxylation, in agreement with previous studies.[25, 26] Together, these data indicate that VKORC1, GGCX and γ-carboxylated proteins are present in islets and β-cells.

Loss of γ-carboxylation induces a diabetic signature in islets

As a first step to determine the role of VK-dependent carboxylation in islets and β-cells, we analyzed the expression profile of *Ggcx^{ff}; Pdx1-Cre* islets by RNA-sequencing (RNAseq). In comparison to control *Ggcx^{ff}* islets, 319 genes were differentially expressed in *Ggcx^{ff}; Pdx1-Cre*

islets (adjusted *P* value ≤ 0.05; Table S2). This set of genes was divided into two groups based on whether their expression was increased (114 genes) or decreased (205 genes) following *Ggcx* inactivation in islets and a series of bioinformatics analyses was completed. Gene set enrichment analyses with Gene Ontology revealed that many biological processes implicated in the response to ER stress were significantly enriched within the group of genes downregulated in *Ggcx^{ff}; Pdx1-Cre* islets (Fig.S2A). Similarly, when we interrogated the KEGG pathway database, we found that this group of genes was enriched for pathways such as *apoptosis* and *protein processing in ER* (Fig.S2B). Using the UniProt annotated keywords database, we observed, in the group of genes that were upregulated in *Ggcx^{ff}; Pdx1-Cre* islets, a very strong enrichment for protein keywords related to the secretory pathway (Fig.S2C). We therefore hypothesized that the capacity of islet cells to respond and adapt to ER stress might be dysregulated in the absence of γ-carboxylation, potentially leading to impaired β-cell function. In support of this notion, we found that a network of genes previously implicated in the β-cell response to ER stress[29, 30] was down-regulated in the absence of γ-carboxylation (Fig.S2D).

We next determined to which extent the transcriptome of *Ggcx^{ff}; Pdx1-Cre* islets intersects with the gene expression profile of islets from pre-diabetic (adult C57BL/6 mice on HFD for 8 weeks) or diabetic (8-weeks old *Lepr$^{db/db}$* and 7-weeks old *Ire1α^{ff}; Ins2-Cre$^{ERT/+}$*) mouse models.[31-33] Seventy-five % of the up- and 45% of the down-regulated genes in *Ggcx^{ff}; Pdx1-Cre* islets were similarly dysregulated in at least one of these models (Fig.S2E). About one-third of these genes encode proteins found within the secretory pathway (Fig.S2F). The overlap between the transcriptome of *Ggcx^{ff}; Pdx1-Cre* islets and each mouse model was statistically significant for all comparisons (Table S3). Overall, these data suggest that loss of function of *Ggcx* in

pancreatic endocrine cells induces a diabetic gene signature in these cells, presumably by altering their capacity to respond to ER stress.

GGCX is necessary for the maintenance of an adequate β-cell mass in adult mice

To determine the role of VK-dependent carboxylation in islet function in vivo, we next analyzed the metabolic consequences of a pancreas-specific inactivation of *Ggcx* (*Ggcx^{ff}; Pdx1-Cre* mice). The *Pdx1-Cre* driver was selected because it resulted in efficient deletion in pancreatic islets[34], without expressing the human growth hormone (hGH).[35, 36] *Ggcx* mRNA level was reduced by >90% and GGCX protein was undetectable in the pancreatic islets of these mice (Fig.S1E and Fig.1F). In agreement with efficient inactivation of GGCX, protein γ-carboxylation was abrogated in *Ggcx^{ff}; Pdx1-Cre* islets (Fig. 1F). These mice did not display any differences in energy expenditure parameters (energy expenditure, O_2 consumption, CO_2 release), physical activity, food intake, pancreas weight and body weight (Fig.S3A-E). In addition, inactivation of *Ggcx* occurred only in the pancreas of the *Ggcx^{ff}; Pdx1-Cre* mice and not in any other tissue tested (Fig.S3F).

Glucose tolerance test (GTT) revealed that an absence of γ-carboxylation in islets does not affect glucose handling in 16-week-old mice (Fig. 2A). However, at 24 weeks of age, *Ggcx^{ff}; Pdx1-Cre* mice showed significantly elevated fasting blood glucose and decreased glucose tolerance (Fig. 2B). This defect was traced to reduced circulating insulin following injection of glucose compared to control (Fig.2C). Insulin sensitivity, assessed by an insulin tolerance test (ITT), appeared to be unaffected (Fig. 2D). Pancreas immunohistochemistry revealed that β-cell area and mass were reduced in *Ggcx^{ff}; Pdx1-Cre* mice at 32 weeks but not at 12 weeks of age (Fig.

2E). Accordingly, total insulin content was diminished in the pancreas of 24-28 weeks old *Ggcx^{ff}; Pdx1-Cre* mice (Fig. 2F). Beta-cell area and β-cell mass were also significantly lower in mice lacking the two vitamin K oxidoreductases, *Vkorc1* and *Vkorc1l1*, in the pancreas only (Fig.S3G-J), confirming the implication of the VK-cycle in the observed phenotype.

By western blot using antibodies against cleaved-caspase-3 and phospho(Ser139)-Histone H2A.X, we detected apoptosis and DNA damage in >32-weeks old *Ggcx^{ff}; Pdx1-Cre* islets, but not in *Ggcx^{ff}* controls (Fig.2G). Beta-cell specific apoptosis was independently confirmed using TUNEL and insulin co-staining on pancreas sections (Fig.2H-I). Importantly, β-cell apoptosis, β-cell mass, and pancreas insulin content were all unaffected in *Pdx1-Cre* mice (Fig.2H and Fig.S3K-L).

Static ex vivo glucose stimulated insulin secretion (GSIS) experiments revealed a significant reduction in the capacity of the *Ggcx*-deficient (*Ggcx^{ff}; Pdx1-Cre*) islets to secrete insulin in response to glucose (Fig.2J), suggesting that γ-carboxylation is not only necessary to maintain a proper β-cell mass, but is also required for an adequate insulin secretion in response to glucose in β-cells.

Pancreas or β-cell specific deletion of *Ggcx* compromises insulin secretion in response to high fat diet

Since the phenotype of the *Ggcx^{ff}; Pdx1-Cre* mice appears to be age-dependent, we hypothesized that GGCX activity would be predominantly required when β-cells need to adapt to stress such as age-related insulin resistance. To test GGCX involvement in acute β-cell stress response, 10-

week-old *Ggcx^{ff}; Pdx1-Cre* mice, which had not developed metabolic and β-cell mass phenotypes yet (Fig.2A and E), were fed a high-fat diet (HFD; 60% kcal from fat) or a matched control low-fat diet (10% kcal from fat) for 7 days. This approach was previously shown to induce in wildtype mice β-cell ER stress, glucose intolerance and hyperinsulinemia without significantly affecting peripheral insulin sensitivity.[37, 38] qPCR analysis of ER-stress markers on isolated islets confirmed that this short bout of HFD induces ER-stress in both control and *Ggcx^{ff}; Pdx1-Cre* islets (Fig.S4A-F). Interestingly, *Ddit3*, *Ppp1r15a* and *Hspa5* were significantly more elevated following short HFD feeding in the *Ggcx^{ff}; Pdx1-Cre* islets, while *sXbp1* was lower, suggesting a dysregulated unfolded protein response (UPR) in the absence of γ-carboxylation. This 7-day HFD feeding was also enough to increase body weight in mice, regardless of the presence of *Ggcx* in their islets (Fig.S4G). However, mice deprived of *Ggcx* expression in islets were not able to maintain their fed blood glucose level following HFD (Fig.3A). The insulinemic response to glucose in absolute value or expressed as a stimulation index (SI: blood insulin concentration at 15 minutes or 30 minutes over T0) was not affected in the absence of *Ggcx* in mice fed the control diet (Fig.3B-C). In contrast, following 7 days on HFD, *Ggcx^{ff}; Pdx1-Cre* mice showed a strong suppression in SI, which was significantly lower than the SI of *Pdx1-Cre* control mice (Fig.3D-E). Of note, this impaired SI was associated with elevated fasting insulin (Fig.3F), while fasting glucose was not reduced and glucose tolerance was moderately impaired (Fig.S4H).

To determine if GGCX affects β-cell function in a cell-autonomous manner, we next analyzed *Ggcx^{ff}; Ins1-Cre* mice. At 10 weeks of age, *Ggcx^{ff}; Ins1-Cre* mice maintained on a regular chow diet had normal glucose tolerance, fasting glucose, and fasting insulin (Fig.S4I-K). When *Ggcx^{ff};*

Ins1-Cre mice were fed a HFD for 7 days, no difference in body weight was noted (Fig.S4L), but their fed glucose level was significantly increased (Fig.3G) and their SI was reduced (Fig.3H-I) in comparison to *Ins1-Cre* control mice fed the same HFD. Remarkably, in the same animals, fasting glucose was significantly increased (Fig.3J), although fasting serum insulin was also increased (Fig.3H). Glucose tolerance assessed through intraperitoneal or oral glucose load was unaffected (Fig.S4M-N), suggesting a compensatory increase in insulin-independent glucose disposal.[39] Fasting hyperglycemia associated with hyperinsulinemia suggests peripheral insulin resistance. Accordingly, the homeostatic model assessment for insulin resistance (HOMA-IR) was increased in *Ggcx^{ff}; Ins1-Cre* mice on HFD (Fig.3K), and insulin sensitivity evaluated by ITT was reduced in the same animals (Fig.3L). Together, these observations indicate that the absence of γ-carboxylation directly impacts β-cells' capacity to adapt their insulin secretion in the face of metabolic stress, resulting in increased fasting insulin, loss of glucose-stimulated insulin secretion and reduced peripheral insulin sensitivity.

To relate these findings to humans, we analyzed *GGCX* and *VKORC1* gene expression in human islets from 15 non-diabetic and diabetic donors and observed that the level of these two enzymes vary widely between donors, but nevertheless strongly correlate with one another (Fig.3M and Table S1). This observation suggests that for certain individuals, the γ-carboxylation machinery in their β-cells might be more active compared to others. Further analysis revealed that *GGCX* expression levels positively and significantly correlate with the capacity of islets to secrete insulin in response to glucose (r=0.7181; *P*=0.0026; Fig.3N). The levels of *VKORC1* also positively correlate with the same parameter although it did not reach statistical significance

(r=0.4677; *P*=0.0787; Fig.3O). These results imply that γ-carboxylation could also impact glucose-stimulated insulin secretion in human β-cells.

Vitamin K attenuates apoptosis induced by ER Ca^{2+} depletion

To determine if VK and γ-carboxylation can protect β-cells from the acute effects of ER stress, INS-1 832/3 β-cells were cultured for 24h in media containing 25mM glucose in the presence or absence of thapsigargin, an inhibitor of the sarco/endoplasmic reticulum Ca^{2+}-ATPase (SERCA), and a pharmacological inducer of ER stress.[38] Doses of thapsigargin (10-40nM) inducing moderate to elevated cell death in INS-1 cell cultures were selected based on previously published data.[40] Induction of Grp78/BiP and phospho(Ser724)-IRE following thapsigargin treatment confirmed the presence of ER stress and UPR (Fig.S5A-B). In addition, western blots showed that thapsigargin dose-dependently induced apoptosis and DNA damage in β-cells, while pre-treatment with VK_1 reduced the deleterious effects of 10 and 20nM of thapsigargin (Fig.4A). Interestingly, in the presence of thapsigargin, GGCX protein level was increased by more than two-fold and its γ-carboxylation was also increased when VK_1 was included in the media (Fig.4B). These results suggest that γ-carboxylation is activated in response to ER stress to protect β-cells from apoptosis.

Glucose regulates vitamin K-dependent carboxylation in β-cells

We next sought to determine if glucose itself, a physiological inducer of ER stress and UPR in β-cells[38], could regulate the VK cycle and γ-carboxylation. *Ggcx* and *Vkorc1* expression was increased both at the mRNA and protein level in response to 15mM glucose in wild type C57BL/6J mouse islets (Fig.4C-D). GGCX expression and γ-carboxylation were also induced

when the rat β-cell line INS-1 832/3 was cultured in the presence of high glucose (25 mM) concentrations (Fig.4E). To confirm that glucose regulates the VK cycle in vivo, 2-month-old Wistar rats were infused with glucose for 3 days, had their islets isolated and gene expression was analyzed by qPCR. Glycemia reached ~15 mM in glucose-infused rats (Fig.4F), and this was sufficient to significantly increase *Ggcx* and *Vkorc1* expression in their islets (Fig.4G) compared to rats infused with saline solution which maintained their blood glucose at ~7 mM. Finally, GGCX expression and global γ-carboxylation were also increased in non-diabetic human islets cultured for 3 days in media containing 15mM glucose (Fig.4H-I, Table S1). These data indicate that glucose positively regulates the level and activity of the VK cycle in rodent and human β-cells.

ERGP is a vitamin K-dependent γ-carboxylated protein expressed in β-cells

In our mouse islet RNAseq dataset, the genes encoding known γ-carboxylated proteins were all expressed at very low levels (Fig.S6A). Together with the detection in islets of multiple γ-carboxylated proteins by western blot (Fig.1F), these observations suggest that β-cells express unknown Gla proteins.

Immunoprecipitation of γ-carboxylated proteins from 5-day old wildtype (WT) mouse liver extracts using our pan-specific α-Gla antibody led to the identification of aspartyl/asparaginyl β-hydroxylase (ASPH) as a putative intracellular Gla protein (Table S4). The *Asph* locus contains two promoters (P1 and P2), undergoes extensive alternative splicing and encodes for three previously characterized ER-resident proteins: aspartyl/asparaginyl β-hydroxylase (ASPH), junctate and junctin (Fig.S6B).[41, 42] ASPH is expressed in several tissues under the control of

P1, while junctate and junctin expressions are controlled from P2 and appear to be restricted to cardiac and skeletal muscles.[43] ASPH is a type II transmembrane protein of ~80 kDa containing three luminal domains: an EF-hand Ca^{2+}-binding domain, a negatively charged Glu rich domain (GRD) containing 39 Glu residues, and an alpha-ketoglutarate dependent hydroxylase domain (Fig.S6B). Junctate and junctin are ER-resident proteins corresponding to shorter variants of ASPH. Junctate and junctin share a different N-terminus cytosolic domain compared to ASPH, and junctin is characterized by a basic luminal domain instead of the acidic GRD domain found in junctate and ASPH (Fig.S6B). Islet RNAseq data indicate that overall *Asph* expression level in islets is comparable to *Ggcx* and higher than any of the other genes encoding known γ-carboxylated proteins (Fig.S6A). Our data also show that promoter P2 is inactive in mouse islets, confirming that junctate and junctin isoforms are not expressed in these cells (Fig.S6B-C). However, we detected a high level of expression for the last unique exon of junctate in islets, indicating that a truncated version of ASPH might be expressed in these cells. This shorter isoform was amplified by PCR on mouse islet cDNA using a pair of oligonucleotides located respectively in the first exon of ASPH (downstream of P1) and in the last exon of junctate. Sequencing of the PCR product identified this transcript as *Asph* variant 4. The protein encoded by this transcript is identical to the first 308 amino acids (a.a.) of ASPH, but lacks the last 433 a.a. including the hydroxylase domain (Fig.S6B). Since this ER-resident protein appears to be γ-carboxylated (Table S4 and see below), we decided to name it Endoplasmic Reticulum Gla Protein (ERGP). The mRNAs encoding ASPH and ERGP are both expressed in pancreatic islets, with ERGP mRNA being at least three times more expressed than ASPH mRNA (Fig.S6C). Publicly available islet transcriptomic data further indicate that the mRNA of ASPH and ERGP, but not of junctate and junctin, are expressed in β-cells

(Fig.S6B).[24] Based on these observations, we decided to determine if ASPH and ERGP are the γ-carboxylated proteins detected in islets and β-cells.

ASPH (A) and ERGP (E) share a GRD that could be prone to γ-carboxylation. To detect these two proteins, we generated and affinity-purified rabbit polyclonal antibodies against the GRD domain; hereafter called α-A/E-GRD (Fig.S6D-E). Importantly, the addition of VK_1 or warfarin did not change the immunoreactivity of α-A/E-GRD antibodies against full-length ASPH and ERGP (Fig.S6E). Anti-Gla immunoprecipitation (IP) followed by α-A/E-GRD western blot or α-A/E-GRD IP followed by α-Gla western blot confirmed that both ASPH and ERGP are γ-carboxylated in one-week-old WT liver but not in the liver of *Vkorc1*$^{-/-}$ mice lacking γ-carboxylation at this age (Fig.S6F-G).[26] Using the same approach, we could show that ASPH and ERGP are expressed and γ-carboxylated in adult control mouse islets, and that their γ-carboxylation was greatly reduced in islets isolated from *Vkorc1*$^{-/-}$;*APOE-Vkorc1l1* mice, which have lower VK oxidoreductase activity and γ-carboxylation in all tissues except the liver (Fig.5A and Fig.S6H).[26] These analyses showed that ERGP expression and γ-carboxylation were respectively ~7 and 8-fold higher than ASPH in control islets (Fig.5B). The same IP analysis performed on *Ggcx*^{ff}*; Ins1-Cre* islets, revealed that ERGP, but not ASPH, is strongly γ-carboxylated in β-cells (Fig.5C). Immunofluorescence on wildtype mouse islets confirmed the expression of ERGP in islet endocrine cells, including β-cells (Fig. 5D). Finally, α-Gla IP followed by LC-MS/MS analyses on INS-1 832/3 cells cultured in 25mM glucose and treated or not with 20nM of thapsigargin indicated that rat ERGP is also carboxylated in a VK-dependent manner in stressed β-cells (Table S5 and Fig.S6I). Together these results establish that ERGP, and to a lesser extent ASPH, are γ-carboxylated proteins expressed in mouse β-cells.

ERGP is γ-carboxylated on several glutamic acid residues located in its Glu-rich domain

To identify the domain(s) and specific glutamic acid residues subjected to γ-carboxylation in ASPH and ERGP, we first expressed full-length ASPH-3XFLAG, or mutants lacking specific domains in HEK293 cells, a cell line which supports VK-dependent carboxylation.[26] Full-length ASPH γ-carboxylation was detected in cells cultured in the presence of VK_1, but not in presence of warfarin or when the GRD was deleted (Fig.S6J). Although the amino acid sequence of the GRD is poorly conserved across mammalian species, the enrichment of glutamic acid residues has been retained throughout evolution (Fig.S6K). Internal deletions within the GRD of ERGP indicated that most of the γ-carboxylation sites are in the region encompassing residues 255 to 310 and/or that the C-terminal domain contains a critical sequence for the recognition by GGCX (Fig.5E-F). We next mutated glutamic acid residues throughout the GRD into aspartic acid residues, which cannot be γ-carboxylated by GGCX (Fig.5E). Using this series of mutant proteins, we found that γ-carboxylated residues are mainly located in the N- and C-terminal regions of the GRD (Fig.5G and Fig.S6L), which was confirmed by LC-MS/MS analysis (Fig.5H-I and Table S6). No Gla containing peptides were identified by the LC-MS/MS approach when ERGP was purified from HEK293 cells treated with warfarin or from E. coli which lack γ-carboxylation machinery (Fig.5H).

We next tested whether γ-carboxylation could modulate the Ca^{2+}-binding capacity of ERGP.[11] Carboxylated and uncarboxylated ERGP-3XFLAG were expressed and purified from HEK293 cells (Fig.5J) and $^{45}Ca^{2+}$ overlay experiments revealed that γ-carboxylated ERGP binds

significantly more Ca^{2+} than its uncarboxylated counterpart (Fig.5K-L), suggesting that the presence of Gla residues in the GRD increases ERGP capacity to bind Ca^{2+}.

Carboxylated ERGP regulates store-operated Ca^{2+} entry

The cellular function of ERGP is unknown and to our knowledge has never been investigated. One study in T cells suggested that junctate acts as a Ca^{2+}-sensing ER protein regulating the formation of Stromal interaction molecule 1 (STIM1) and Orai1 protein complexes to activate store-operated Ca^{2+} entry (SOCE), a cellular response whereby extracellular Ca^{2+} enters the cytosol following ER Ca^{2+} depletion to replete cellular Ca^{2+}.[44]-[45] SOCE is a prominent Ca^{2+} influx mechanism by which several cell types maintain cytosolic and ER Ca^{2+} levels at rest.[46, 47] SOCE has been implicated in the regulation of insulin secretion by β-cells [48], with loss of STIM1 leading to reduced insulin secretion and increased ER stress.[49] These observations prompted us to investigate whether ERGP and γ-carboxylation could affect cellular Ca^{2+} flux and SOCE.

To eliminate potential confounding effects caused by the endogenous human *ASPH* locus, we used CRISPR/Cas-9 genome editing to knockout all *ASPH* encoded isoforms in HEK293 cells (*ASPH*$^{-/-}$ HEK293) (Fig.S7A-B). SOCE machinery was recapitulated in these cells by expressing STIM1-Myc and Orai1-HA in the presence or absence of ERGP-3XFLAG, with or without VK_1 (Fig.S7C). Carboxylated GGCX was detected in VK_1 treated cells regardless of ERGP expression, confirming efficient γ-carboxylation in these cells. Ratiometric cytosolic Ca^{2+} measurement with Fluo-4 and Fura Red Ca^{2+} indicators was next used to assess SOCE, which was triggered first by depleting ER Ca^{2+} with thapsigargin in Ca^{2+} free buffer followed by Ca^{2+}

addback to the buffer (Fig.6A). Using these experimental settings, we observed that cells expressing γ-carboxylated ERGP are characterized by a reduction in their ER Ca^{2+} release and SOCE (Fig.6B-D). In addition, there was a significant reduction in basal cytosolic Ca^{2+} level in the same cells (Fig.6B and 6E), suggesting that ERGP, only when γ-carboxylated, restrains cytosolic Ca^{2+} in cells.

The impact of ERGP and of its carboxylation on ER Ca^{2+} levels was next assessed directly using the D4ER ratiometric ER-targeted Förster resonance energy transfer (FRET) based Ca^{2+} sensor.[50] These analyses confirmed that in the presence of γ-carboxylated ERGP, HEK293 cells have a significantly lower basal ER free Ca^{2+} level and reduced ER Ca^{2+} efflux following thapsigargin treatment (Fig.6F-H). Apparent ER Ca^{2+} levels were restored to the baseline levels found in control cells by treatment with the Ca^{2+} ionophore ionomycin in the presence of 2mM extracellular Ca^{2+}, indicating accurate and efficient D4ER FRET measurement in all conditions (Fig.6F and Fig.S7D).

Activation of SOCE in cells is characterized by the formation of ER-PM junction puncta containing both STIM1 and Orai1, as observed following a 15 minutes thapsigargin treatment (Fig.6I, left panels). In these conditions, VK_1 or ERGP alone did not affect the formation of STIM1-Orai1 puncta, but the presence of γ-carboxylated ERGP significantly reduced the formation of these protein complexes (Fig.6I-J). A FRET assay using YFP-Orai1 and STIM1-CFP was used as an orthogonal validation of the impact of γ-carboxylated ERGP on the formation of these complexes in living cells. Western blot analysis confirmed similar expression level of the STIM1-CFP and YFP-Orai1 constructs in *ASPH*$^{-/-}$ HEK293 cells in all conditions

(Fig.S7E) and live-cell imaging experiments confirmed that γ-carboxylated ERGP restrains the formation of puncta co-expressing STIM1-CFP and YFP-Orai1 following 5-, 10- and 15-minutes thapsigargin treatment (Fig.6K). Accordingly, these experiments revealed that the average corrected FRET signal following thapsigargin addition was significantly reduced in presence of γ-carboxylated ERGP (Fig.6L-N). These results suggest that when γ-carboxylated, ERGP limits the formation of STIM1-Orai1 complexes, thus restraining SOCE.

Ca^{2+} overfilling in *Ggcx*-deficient β-cells causes impaired fasting hyperinsulinemia

We used *Ggcx^{ff}; Ins1-Cre* islets as a genetic model of decarboxylated ERGP in β-cells to determine how γ-carboxylation of this protein affects Ca^{2+} homeostasis in these cells. Cytosolic Ca^{2+} flux was analyzed in partially dissociated islet cells from *Ggcx^{ff}; Ins1-Cre* and *Ins1-Cre* (control) mice by ratiometric live-cell imaging as above. SOCE was monitored with the protocol used for the HEK293 cells (Fig.6A) except that diazoxide, an opener of the ATP sensitive K^+ channel, and verapamil, a voltage gated Ca^{2+} channel (VGCC) blocker, were included in the buffered solution for the duration of imaging to prevent membrane depolarization and Ca^{2+} influx through VGCC.[49] We first noticed that *Ggcx^{ff}; Ins1-Cre* β-cells were characterized by higher cytosolic Ca^{2+} levels at baseline (Fig.7A-B). Moreover, SOCE expressed as absolute value or relative to baseline (ΔF) was increased in the same cells (Fig.7A and C). ER Ca^{2+} release was measured following treatment with a higher dose of thapsigargin (10μM) and was found to be significantly higher in the *Ggcx^{ff}; Ins1-Cre* β-cells (Fig.S7F). We also observed that the number of STIM1 containing puncta at steady state (i.e., 5mM glucose) was more elevated in these cells in comparison to control islets, suggesting that γ-carboxylated ERGP restrains SOCE to maintain proper resting ER Ca^{2+} levels in β-cells (Fig.S7G-H).

Ca^{2+} flux in response to glucose confirmed higher basal cytosolic Ca^{2+} levels in *Ggcx^{ff}; Ins1-Cre* islets in comparison to *Ins1-Cre* islets (Fig.7D-E). Cytosolic Ca^{2+} levels after stimulation with 15mM glucose or KCl were unchanged in the absence of carboxylated ERGP when normalized over the baseline, although they remained elevated in absolute value (Fig.7D and 7F). Altogether, these data in primary β-cells suggest that ERGP γ-carboxylation is necessary to maintain Ca^{2+} homeostasis in β-cells, mainly by suppressing SOCE. In line with the data obtained with HEK293 cells, the increased SOCE present in *Ggcx^{ff}; Ins1-Cre* islet cells appears to result in increased basal cytosolic and ER Ca^{2+} levels.

Chronically elevated cytosolic Ca^{2+} in β-cells has been linked to dysregulated insulin secretion and fasting hyperinsulinemia.[51, 52] We next tested if pharmacologically reducing cytosolic Ca^{2+} in *Ggcx^{ff}; Ins1-Cre* β-cells could restore normal circulating fasting insulin levels in vivo. For this purpose, we selected verapamil, a VDCC blocker and a well-characterized FDA-approved drug. Verapamil treatment of *Ggcx^{ff}; Ins1-Cre* β-cells cultured with 11.1mM glucose ex vivo normalized their cytosolic Ca^{2+} within a few minutes (Fig.7G). In addition, verapamil provided in the drinking water for 5 days to mice fed a short HFD was sufficient to normalize the fasting insulin of the *Ggcx^{ff}; Ins1-Cre* mice (Fig.7H). These results indicate that increased cytosolic Ca^{2+} level in β-cells is likely responsible for the fasting hyperinsulinemia observed in vivo in the *Ggcx^{ff}; Ins1-Cre* mice maintained on HFD (Fig.7I).

DISCUSSION

Link between the VK-cycle and stress in β-cells

Using conditional inactivation of *Ggcx* in mice and unique α-Gla antibodies, we established that the VK cycle is active in pancreatic islets and, more specifically, in β-cells. Supporting a link between γ-carboxylation and β-cell adaptation to stress, we found that glucose regulates γ-carboxylation activity and that VK_1 treatment can protect β-cells from the deleterious effects of high glucose and ER-stress. Together with the observation that mice lacking *Ggcx* in pancreas or in β-cells only failed to adapt their insulin secretion in response to a short HFD feeding, our data suggest that the VK cycle could be part of a mechanism implicated in β-cell survival and function in conditions of adaptation to metabolic stress. Therefore, we could speculate that lower vitamin K intake or diminished γ-carboxylation activity could be a risk factor for the development of diabetes when combined with nutrient excess in humans. In line with our findings, two recent large observational studies indicate that treatment with warfarin compared to direct anticoagulant not targeting carboxylation does significantly increase the risk of new-onset diabetes in male and female patients with atrial fibrillation.[53, 54]

ERGP γ-carboxylation as a regulator of β-cell Ca^{2+} homeostasis

Our results identified ERGP as a γ-carboxylated protein present in islets and β-cells. The data indicate that γ-carboxylated ERGP decreases the formation of STIM1 and Orai1 puncta following ER Ca^{2+} store depletion, thereby partially inhibiting SOCE and reducing baseline cytosolic and ER Ca^{2+} levels. Conversely, decarboxylation of ERGP in *Ggcx^{ff}; Ins1-Cre* β-cells was associated with increased cytosolic and ER Ca^{2+} levels at baseline and following SOCE. The

impacts of SOCE inhibition by γ-carboxylated ERGP on ER and cytosolic Ca^{2+} at steady state is consistent with the notion that SOCE is essential to maintain resting Ca^{2+} levels in the ER and cytosol, as previously reported by others.[46, 47, 55, 56] We cannot exclude that γ-carboxylated ERGP directly controls ER Ca^{2+} levels, but we believe that it is unlikely given that decreased ER Ca^{2+} level will be expected to activate SOCE.[57] Rather, our data suggest that γ-carboxylated ERGP refrains SOCE by acting directly or indirectly on the STIM1 conformational changes elicited by ER Ca^{2+} concentrations, consistent with our observations that both SOCE and ER Ca^{2+} levels are increased in absence of γ-carboxylation. Altogether the data imply that increased SOCE is the primary defect in *Ggcx^{ff}; Ins1-Cre* β-cells.

Junctate, whose luminal domain is identical to ERGP but has a different N-terminal cytosolic sequence, has been reported to interact with and regulate the SERCA2 pump and the inositol 1,4,5 trisphosphate receptors (IP3R), two ER membrane proteins controlling Ca^{2+} flux between the ER and the cytosol.[58, 59] Whether γ-carboxylated ERGP also regulates Ca^{2+} homeostasis in β-cells through a similar mechanism is currently unknown. It is important to note however, that in these earlier publications junctate was studied in its decarboxylated form, since VK was not included in the culture media. It should be also noted that since junctate and ERGP have distinct N-terminal cytosolic domains, these two proteins may affect cellular Ca^{2+} homeostasis through different mechanisms. Finally, since junctate mRNA was not detected in β-cells, we did not further investigate the γ-carboxylation and function of this protein in this cell type.

Previous studies suggest that the acute activation of Ca^{2+} flux between ER and cytosol is critical for several β-cell cellular processes, including survival and insulin secretion,[48, 49, 60] but that

chronic stimulation of Ca^{2+} signaling pathway can induce ER stress, β-cell dysfunction and death.[49, 61, 62] Our data show that the Ca^{2+} binding capacity of ERGP increases when γ-carboxylated and that this modification restrains SOCE suggesting that γ-carboxylation could modulate ERGP ER Ca^{2+} sensing capacity. This process appears to be necessary to avoid Ca^{2+} overfilling and to maintain appropriate cytosolic and ER Ca^{2+} levels in β-cells. Under conditions of chronically elevated intracellular Ca^{2+} levels, reducing Ca^{2+} entry would prove beneficial to prevent β-cell dysfunction and diabetes progression. In humans, insufficient VK intake may therefore contribute to β-cell dysfunction in conditions of β-cell stress by reducing ERGP γ-carboxylation, thereby increasing the risk of T2D.

Fasting hyperinsulinemia as a driver of insulin resistance and T2D

Noteworthily, the mice lacking GGCX in the pancreas or only in β-cells and fed a HFD for 7 days are characterized not only by reduced glucose-stimulated insulin secretion and increased blood glucose, but also by increased fasting serum insulin and reduced insulin sensitivity. These observations are consistent with the notion that in conditions of nutrient excess, chronic elevation of intracellular Ca^{2+} and ER stress in β-cells can lead to uncontrolled hyperinsulinemia which could ultimately result in peripheral insulin resistance.[51] There is a growing number of studies in rodents and humans suggesting that prolonged fasting insulin hypersecretion precedes and promotes insulin resistance and could be the initiating event of T2D.[1, 3] Conversely, reducing insulin secretion can prevent insulin resistance, obesity, and fatty liver disease.[2, 51] The metabolic phenotype of the *Ggcx^{ff}; Ins1-Cre* mice following a short period of HFD suggests that γ-carboxylated ERGP may be required both to prevent uncontrolled insulin secretion by β-cells in the context of nutrient excess and to preserve normal glucose-stimulated insulin secretion.

ERGP as a VK-dependent protein

Since the discovery more than 45 years ago that a group of clotting factors was γ-carboxylated on specific glutamic acid residues in a VK-dependent manner [63], a total of 15 unique Gla proteins have been identified in mammals. They all share a relatively well-conserved "Gla domain" characterized by the presence of 3 to 12 γ-carboxylated glutamic acid residues and two cysteines forming a disulfide bridge. While these proteins are either secreted or localized at the plasma membrane, ERGP and ASPH are ER-resident proteins and their "Gla domain" possesses several unique features. First, the ASPH/ERGP GRD, with more than 190 a.a., is larger than the classical Gla domains which are on average less than 50 a.a. long. Second, the ASPH/ERGP GRD does not contain a disulfide bridge and the Gla residues are distributed in the N- and C-terminal regions instead of being clustered in the center. Third, ERGP and ASPH do not contain a sequence matching the GGCX substrate recognition sequence found in the other Gla proteins. Together, these features suggests that ASPH and ERGP may define a distinct class of γ-carboxylated proteins in mammalian cells.

In conclusion, we propose here that VK-dependent γ-carboxylation is a post-translational modification regulating the capacity of β-cells to adapt to stress. We also identify two mammalian VK-dependent proteins, ERGP and ASPH, and provide evidence that γ-carboxylation regulates β-cell Ca^{2+} homeostasis through ERGP. Together, our findings extend the cellular and physiological function of VK-dependent γ-carboxylation and reveal how this pathway may interact with the development of diabetes.

Limitations of the study

Although we show that γ-carboxylation is present in human islets, it remains to be established if VK-dependent carboxylation is required to prevent Ca^{2+} overfilling in human β-cells. In addition, the precise molecular mechanism by which γ-carboxylated ERGP restricts the formation of the STIM1-Orai1 complex has not been determined here. Finally, we cannot exclude that ERGP may not be the sole γ-carboxylated protein mediating the effect of VK in β-cells.

ACKNOWLEDGEMENTS

We thank Dr. K. Suh for providing the B6.Cg-*Gt(ROSA)26Sor*$^{tm14(CAG-tdTomato)Hze}$/J mice, Dr. D. Pendin and Dr. T. Pozzan for providing the D4ER probe and Dr. G. Karsenty for his critical reading of the manuscript. We also thank the staff of IRCM Core Facilities for their technical support. Human islets for research were provided by the Alberta Diabetes Institute IsletCore at the University of Alberta in Edmonton (http://www.bcell.org/adi-isletcore.html) with the assistance of the Human Organ Procurement and Exchange (HOPE) program, Trillium Gift of Life Network (TGLN) and other Canadian organ procurement organizations. When indicated, human pancreatic islets were provided by the NIDDK-funded Integrated Islet Distribution Program (IIDP) (RRID: SCR_014387) at City of Hope, NIH Grant #2UC4DK098085. This work was supported by funding from the Canada Research Chair program (MF), Diabetes Canada (MF, OG-3-21-5599-MF), Diabète Québec (MF), the Canadian Institutes of Health Research (MF, PJT-169685 and PJT-175025; VP, MOP-77686), the US National Institutes of Health (VP, R01-DK-58096) and the CMDO Network (MF). KG received scholarships from IRCM and the

Natural Sciences and Engineering Research Council of Canada. JL received a fellowship from Diabetes Canada.

Author contributions

J.L. and M.F. conceived the study, designed the experiments, and initiated the project. J.L., K.G., D.F. and M.F. collected and analyzed data. J.B., F.G., S.M.M., and S.H. collected data. A.V. and V.P. prepared islets cDNA from rats perfused with glucose. M.F. and J.L. wrote the manuscript and all authors commented and contributed to editing the final version. M.F. acts as the guarantor of this work and is responsible for data access. J.L. is listed before K.G. as co-first author because she conceived the study, designed the experiments, and wrote the manuscript.

Declaration of interests

The authors declare no conflict of interests.

Inclusion and diversity

We support inclusive, diverse, and equitable conduct of research.

FIGURES

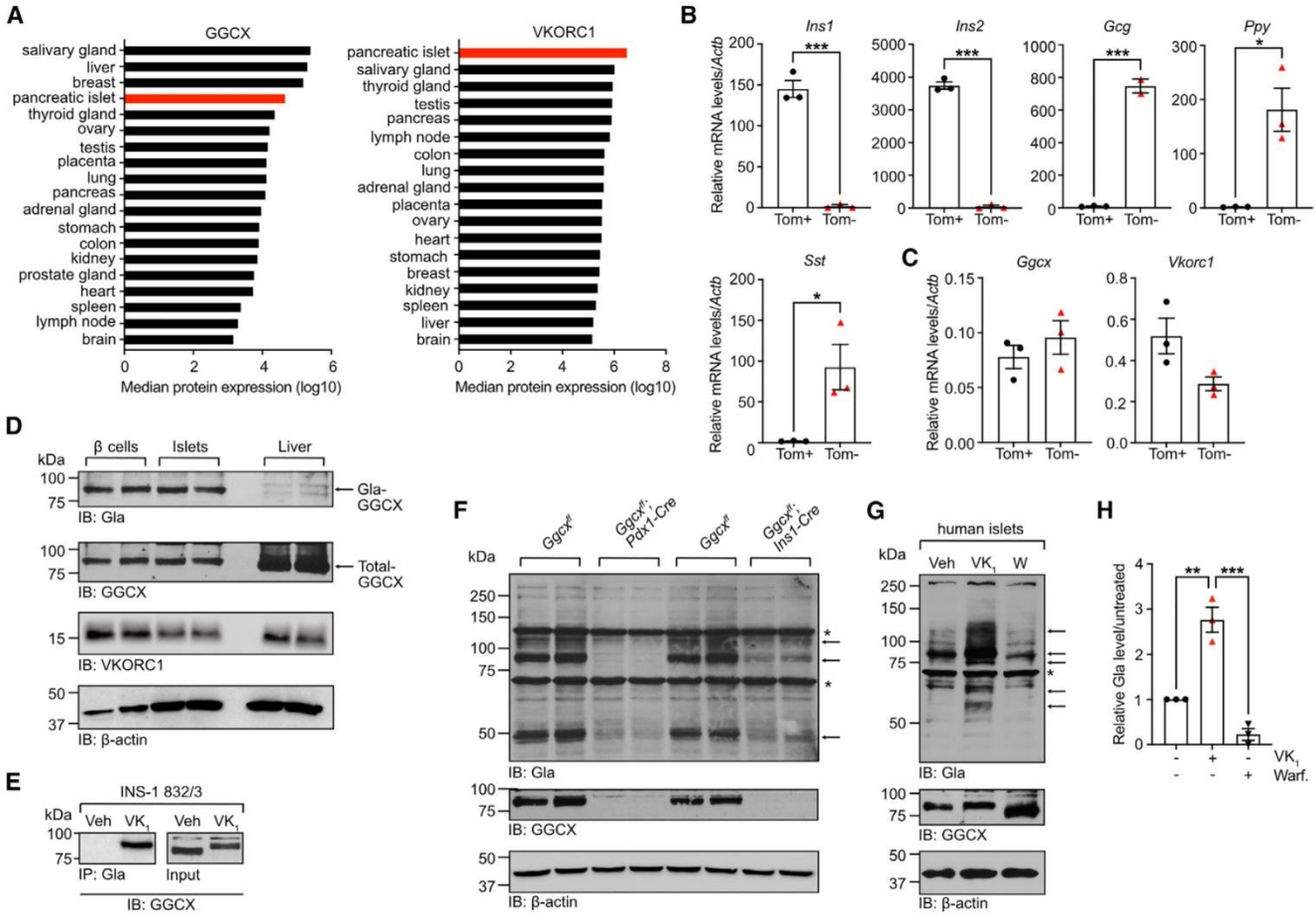

Figure 1: Vitamin K-dependent γ-carboxylation machinery is active in islets and β-cells. (A) GGCX and VKORC1 protein in human tissues expressed as normalized intensity based absolute quantification (iBAQ; www.proteomicsdb.org). **(B-C)** Gene expression analysis by quantitative PCR on sorted β-cells (Tom+) and on the other endocrine islet cells (Tom-) (n=3). **(D)** Protein expression in β-cells, islets and livers from *Ins1*$^{Cre/+}$; *Rosa26*$^{CAG\text{-}lox\text{-}stop\text{-}lox\text{-}tdTomato}$ mice by western blot. **(E)** Gamma-carboxylation in INS-1 832/3 cells cultured with vitamin K_1 (VK_1; 22μM) or vehicle analyzed by anti-Gla immunoprecipitation and western blot. **(F)** Islets from *Ggcx*^{ff}*; Pdx1-Cre* and *Ggcx*^{ff}*; Ins1-Cre* mice and their respective *Ggcx*^{ff} littermates analyzed by western blot. **(G-H)** Human islets from non-diabetic cadaveric donors cultured in presence of VK_1 (22μM),

warfarin (50μM) or vehicle analyzed by western blot. **(G)** Representative western blot experiment with islets from donor R266. **(H)** Gamma-carboxylation quantified using arbitrary densitometry units of Gla signals over β-actin signals. Data from VK_1 and warfarin treated samples were normalized over vehicle treatment (n=3).

Results represent the mean ± SEM; Unpaired, 2-tailed Student's *t* test was used in (B-C); Ordinary one-way ANOVA with Bonferroni's post-tests was used in (H); ***$P < 0.001$; **$P < 0.01$; *$P < 0.05$. See also Figure S1 and Table S1

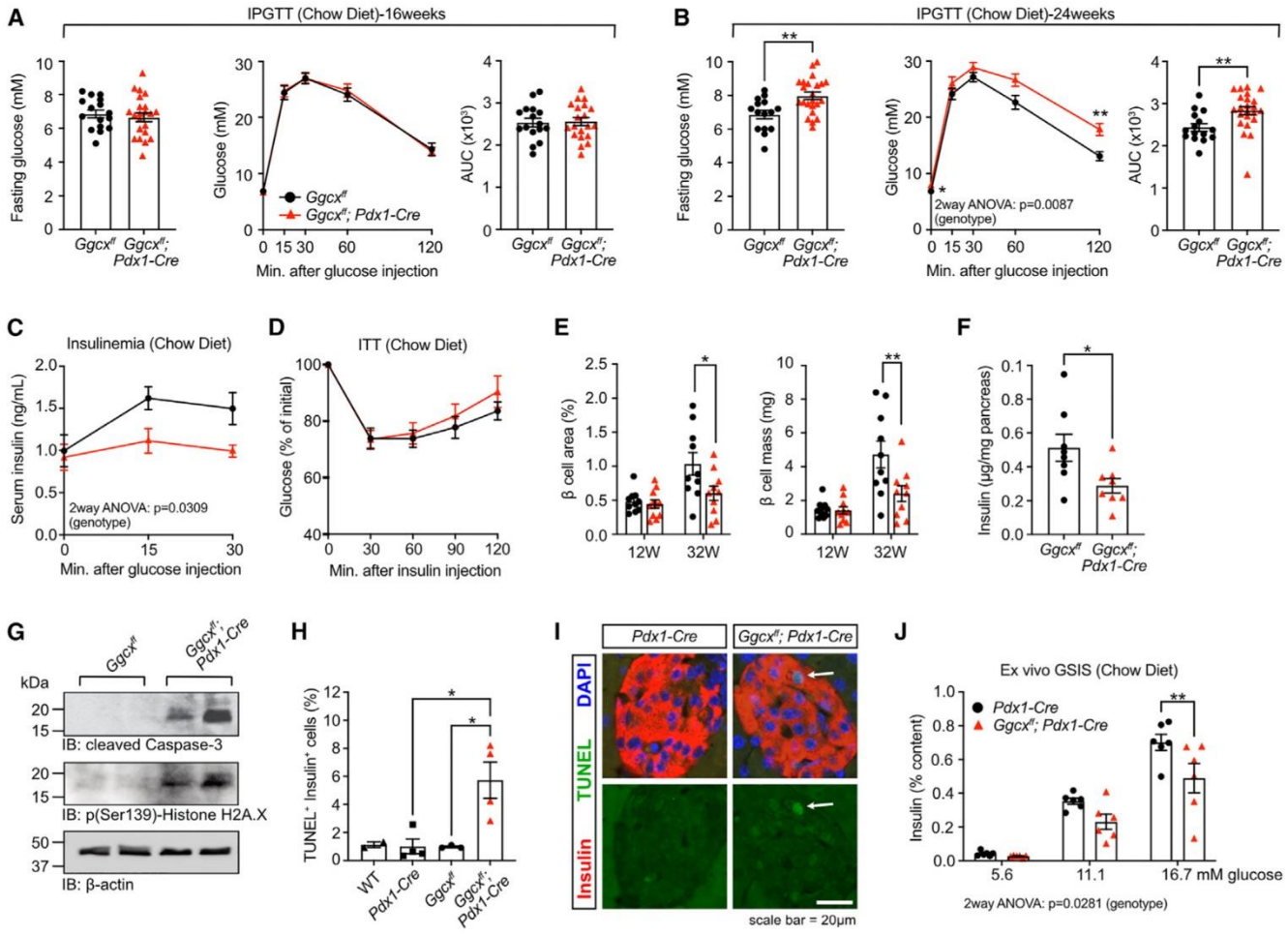

Figure 2: GGCX is necessary for the maintenance of an adequate β-cell mass in adult mice.

(A-B) Intraperitoneal glucose tolerance test (IPGTT) performed on **(A)** 16-weeks-old (n=16-21) and **(B)** 24-weeks-old (n=15-23) *Ggcx^{ff}; Pdx1-Cre* and *Ggcx^{ff}* male mice. **(C)** Insulinemic response to glucose measured in 24-weeks-old male mice (n=10). **(D)** Insulin tolerance test (ITT) in 24-weeks-old male mice (n=9-10). **(E)** Histomorphometric analysis on pancreas section following insulin staining and hematoxylin counterstaining on 12- and 32-weeks-old mice (n=10-11). **(F)** Pancreas insulin content from 24- to 28-weeks old *Ggcx^{ff}; Pdx1-Cre* and *Ggcx^{ff}* male mice (n=8). **(G)** Western blot analysis on islets from *Ggcx^{ff}; Pdx1-Cre* mice. **(H)** TUNEL and insulin co-staining on pancreas sections from 32-weeks old mice (n=2-4). **(I)** Representative picture showing TUNEL^{+} Insulin^{+} β-cells in pancreas section from *Ggcx^{ff}; Pdx1-Cre* mice

(indicated by the white arrow). **(J)** Static ex vivo glucose stimulated insulin secretion (GSIS) test on isolated islets from *Pdx1-Cre* and *Ggcx*^{ff}*; Pdx1-Cre* mice (n=6). Results represent the mean ± SEM; Unpaired, 2-tailed Student's *t* test was used in (A-B) for fasting glucose and AUC and in (F); Two-way ANOVA with Bonferroni's post-tests was used in (A-B) for IPGTTs and in (C-E) and (J); Ordinary one-way ANOVA with Bonferroni's post-tests was used in (H); ***$P < 0.001$; **$P < 0.01$; *$P < 0.05$. See also Figure S2, Figure S3, Table S2 and Table S3.

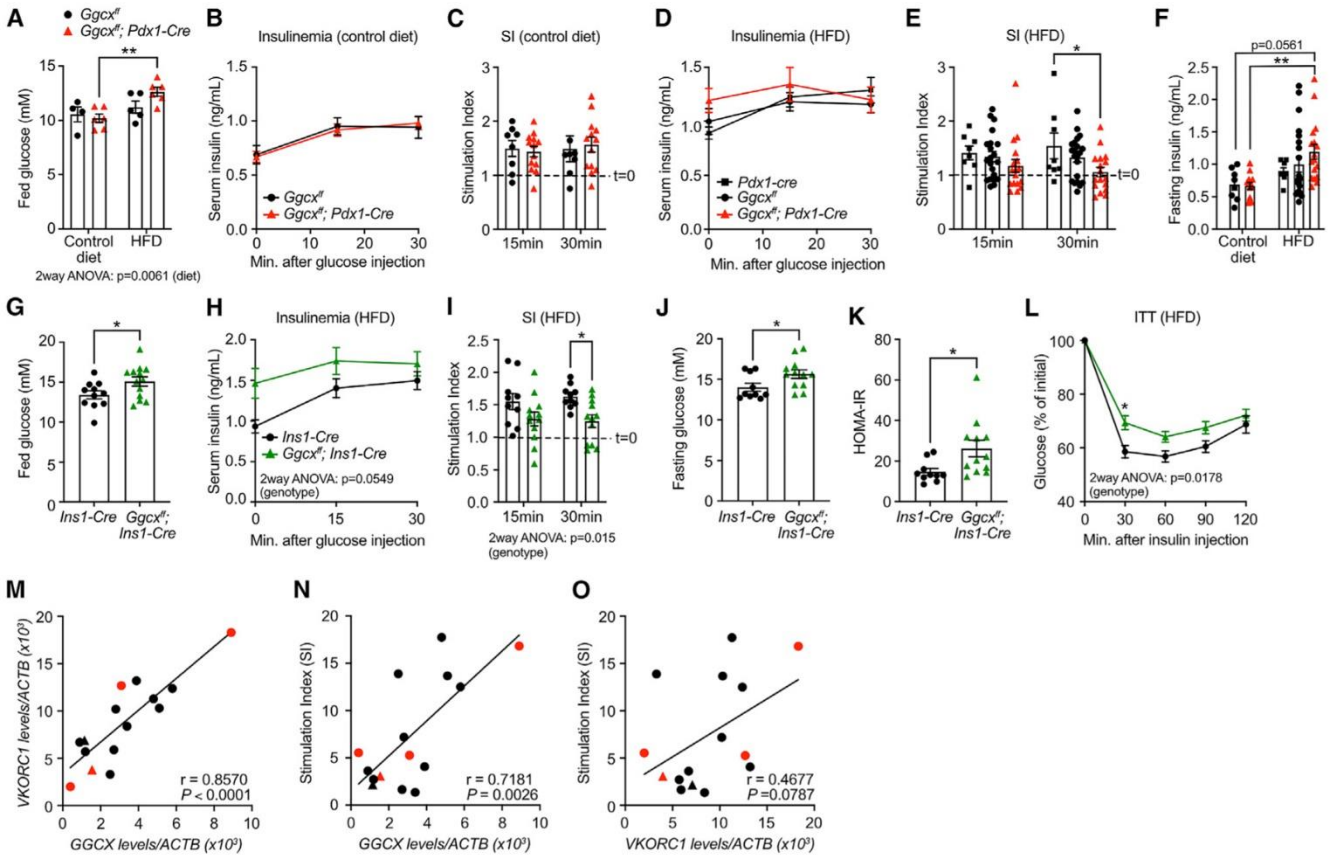

Figure 3: Pancreas or β-cell specific deletion of *Ggcx* compromises insulin secretion in response to high fat diet. (A-L) Ten-weeks old male mice of different genotypes were fed with a high-fat (60%) or a control low-fat (10%) diet for 7 days and metabolic analysis performed. **(A)** Fed blood glucose level for *Ggcx^{ff}; Pdx1-Cre* and *Ggcx^{ff}* male mice (n=4-6). **(B-C)** For the control low-fat diet fed *Ggcx^{ff}; Pdx1-Cre* and *Ggcx^{ff}* mice, the insulinemic response is represented in **(B)** absolute value and **(C)** as stimulation index (blood insulin concentration at 15 or 30 minutes over T0). The dashed line represents a stimulation index of 1 at fasting. **(D-F)** For the high-fat diet fed *Ggcx^{ff}; Pdx1-Cre*, *Ggcx^{ff}* and *Pdx1-Cre* mice, the insulinemic response to glucose is represented in **(D)** absolute value or **(E)** as stimulation index**,** and **(F)** fasting insulin levels are shown (n=8-21). **(G-L)** Metabolic analysis of *Ggcx^{ff}; Ins1-Cre* and *Ins1-Cre* mice following 7 days HFD feeding: **(G)** fed blood glucose, **(H-I)** insulinemic response to glucose, **(J)**

fasting blood glucose, **(K)** HOMA-IR and **(L)** ITT (n=10-13). **(M-O)** Correlation in 15 human islet donor samples between **(M)** *Ggcx* and *Vkorc1* gene expression levels, and between **(N)** *Ggcx* or **(O)** *Vkorc* and each sample's stimulation index (insulin secretion at 10mM over 1mM glucose). Black circles represent non-diabetic male donors, red circles diabetic male donors, black triangle non-diabetic female donor and red triangle diabetic female donor. Results represent the mean ± SEM; Two-way ANOVA with Bonferroni's post-tests was used in (A-E), (H-I) and (L); Ordinary one-way ANOVA with Bonferroni's post-tests was used in (F); Unpaired, two-tailed Student's *t* test was used in (G), (J) and (K); Pearson's correlation was used in (M-O); $^{**}P < 0.01$; $^{*}P < 0.05$. See also Figure S4.

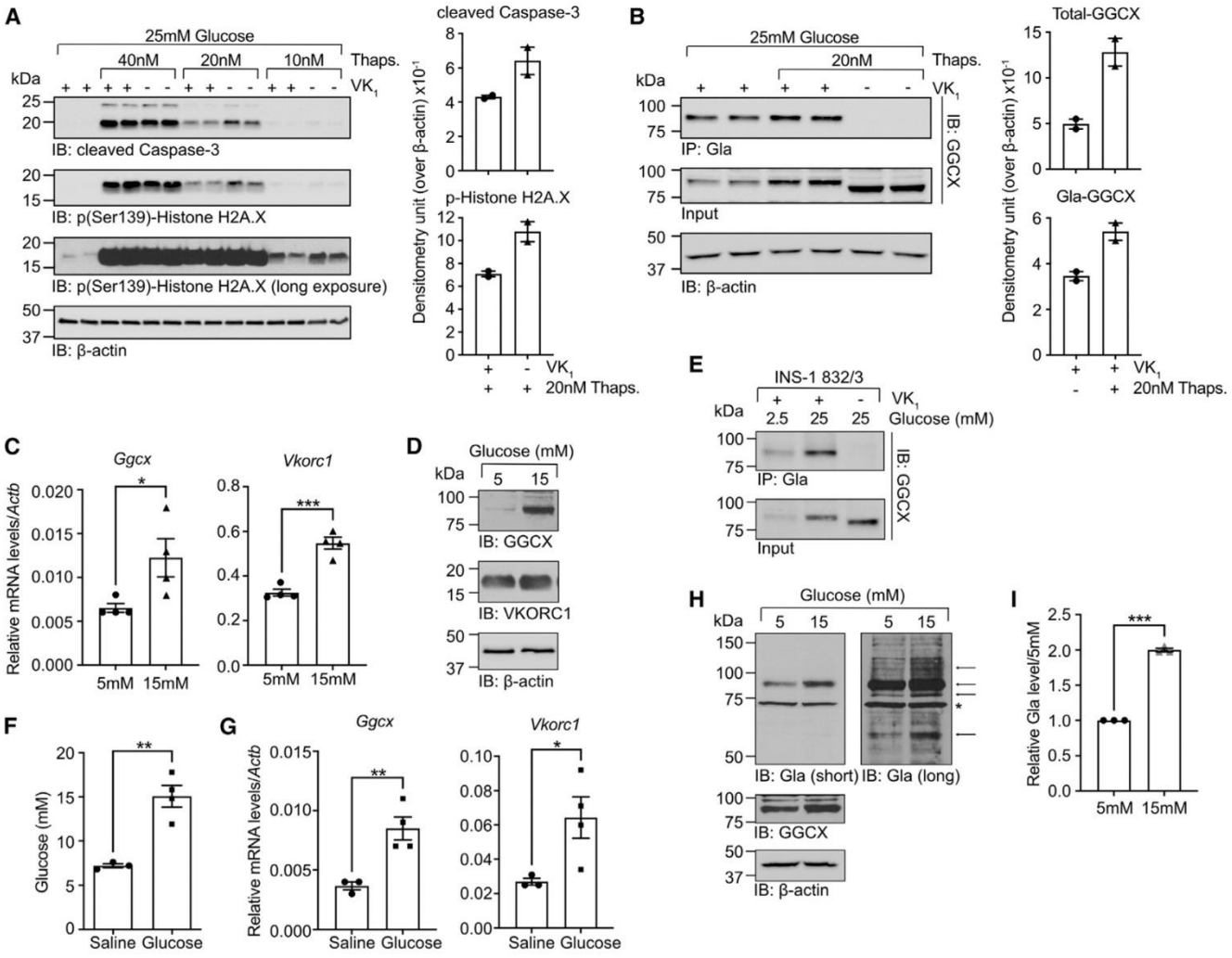

Figure 4: Gamma-carboxylation protects β-cells from ER stress induced cell death and is regulated by glucose. (A-B) INS-1 832/3 cells were cultured with VK_1 (22μM) or vehicle for 48 hours before being cultured for 24 hours in media containing 25mM glucose and thapsigargin. **(A)** Cellular fitness was analyzed by western blot using cleaved-caspase-3 and p(Ser139)-Histone H2A.X antibodies. Quantification was performed using arbitrary densitometry units of cleaved-caspase-3 and p(Ser139)-Histone H2A.X signals obtained in sample treated with 20nM thapsigargin over β-actin signals. **(B)** GGCX γ-carboxylation assessed by anti-Gla immunoprecipitation followed by western blot using anti-GGCX antibodies. Quantification was performed using arbitrary densitometry units of GGCX and Gla-GGCX signals over β-actin

signals. **(C-D)** Islets from C57BL/6J mice were cultured in media containing either 5 or 15mM glucose and expression analyzed by **(C)** qPCR (n=3-4) and **(D)** western blot. **(E)** INS-1 832/3 cells were cultured in media containing 2.5 or 25mM glucose in presence of vitamin K (VK_1; 22μM) or vehicle, and GGCX γ-carboxylation was assessed by anti-Gla immunoprecipitation followed by western blot. **(F-G)** Two-months old Wistar rats were infused during 4 days with saline or glucose. **(F)** Average blood glucose level for each mouse. **(G)** Gene expression analyzed by qPCR (n=3-4). **(H-I)** Human islets from non-diabetic cadaveric donors were cultured in presence of VK_1 (22μM) in media containing either 5 or 15mM glucose for 3 days. **(H)** Representative western blot experiment with islets from donor R288. **(I)** Gamma-carboxylation was quantified using arbitrary densitometry units of Gla signals over β-actin signals. Data from 15mM glucose treated samples were normalized over 5mM glucose treatment (n=3). Results represent the mean ± SEM; Unpaired, two-tailed Student's *t* test was used in (C), (F), (G) and (I); ***$P < 0.001$; **$P < 0.01$; *$P < 0.05$. See also Figure S5 and Table S1.

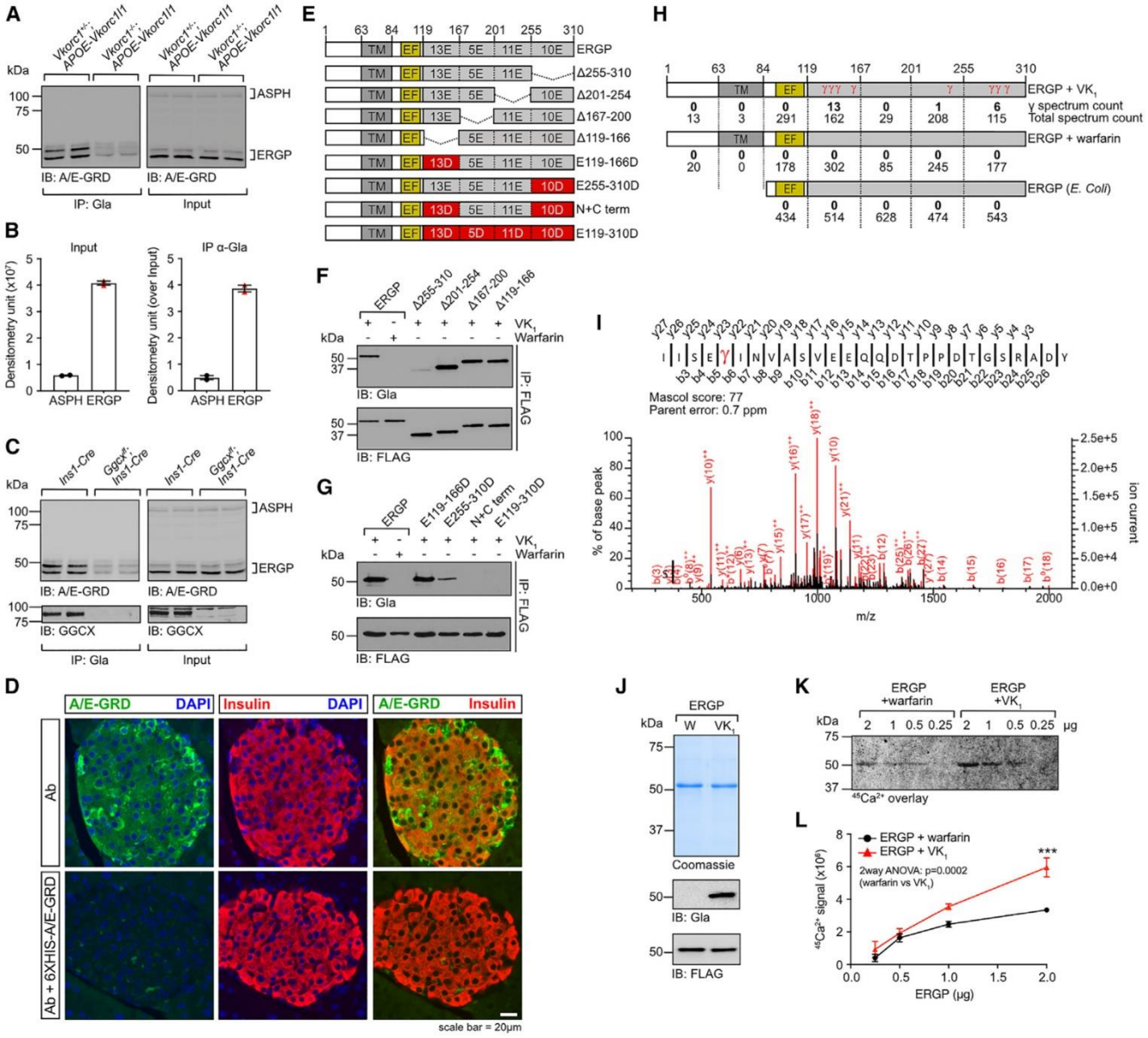

Figure 5: ERGP is a γ-carboxylated protein expressed in β-cells. (A) ASPH and ERGP γ-carboxylation in *Vkorc1*$^{+/-}$*; APOE-Vkorc1l1* and *Vkorc1*$^{-/-}$*; APOE-Vkorc1l1* mouse islets assessed by immunoprecipitation with anti-Gla antibody followed by western blot. **(B)** Expression and γ-carboxylation quantified using arbitrary densitometry units of ASPH and ERGP signals. **(C)** ASPH, ERGP and GGCX γ-carboxylation in *Ggcx*^{ff}*; Ins1-Cre* and *Ins1-Cre* mouse islets assessed by immunoprecipitation with anti-Gla antibody followed by western blot.

(D) Immunofluorescence on pancreas sections from wildtype mice using anti-A/E-GRD and anti-insulin antibodies. Competition with recombinant 6XHIS-A/E-GRD protein was used to demonstrate specificity of the antibody. **(E)** Schematic representation of the constructs used in (F) and (G). **(F-G)** HEK293 cells transfected with the indicated constructs were cultured with VK_1 (22μM) or warfarin (50μM) as specified. FLAG-tagged proteins were immunoprecipitated followed by western blot with anti-Gla or anti-FLAG antibodies. **(H)** Schematic representation of ERGP indicating the total number of γ-carboxylated spectrum counts detected by L-MS/MS. **(I)** Representative LC-MS/MS spectrum showing a γ-carboxylated residue in the peptide ranging from residue 289 to 316 in purified ERGP-3XFLAG expressed in HEK293 grown in presence of VK_1. **(J)** ERGP-3XFLAG purified from HEK293 cells cultured with VK_1 (γ-carboxylated) or warfarin (uncarboxylated) was stained with Coomassie and γ-carboxylation monitored by western blot using anti-Gla antibodies. **(K)** Membrane-immobilized γ-carboxylated and non-carboxylated ERGP-3XFLAG were incubated with $^{45}Ca^{2+}$ and radioactivity detected using a storage phosphorimager screen. **(L)** Ca^{2+} binding quantified using arbitrary densitometry units (n=3). Results represent the mean ± SEM; Two-way ANOVA with Bonferroni's post-tests was used in (L); ***$P < 0.001$. See also Figure S6, Table S4, Table S5 and Table S6.

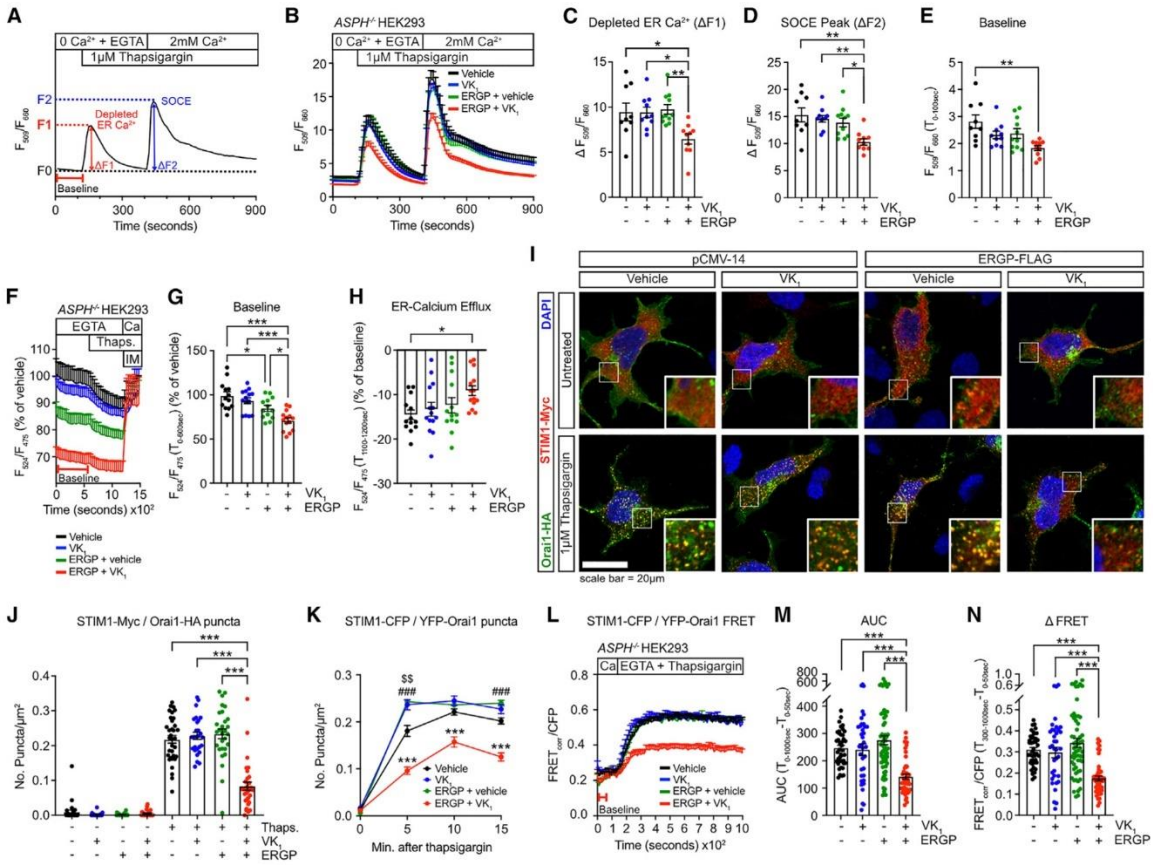

Figure 6: ERGP γ-carboxylation regulates Ca^{2+} flux by modulating STIM1/Orai1 interaction. (A) Representation of the strategy used to measure and quantify store-operated Ca^{2+} entry (SOCE) by live-cell imaging. **(B)** Ca^{2+} imaging traces are represented as the ratio between Fluo-4 and Fura Red emission intensity (F_{509}/F_{660}) for each condition (n=9-11 experimental replicates per condition). **(C-D)** Quantification of **(C)** depleted ER Ca^{2+} and **(D)** SOCE peak are represented as ΔF1 and ΔF2 respectively, as described in (A). **(E)** Baseline cytosolic Ca^{2+} defined as the average F_{509}/F_{660} ratio during the first 100 seconds of recording. **(F-H)** Measurements of ER Ca^{2+} levels in *ASPH*$^{-/-}$ HEK293 cells transfected with the D4ER ratiometric Ca^{2+} probe (n=11-14 experimental replicates per condition). **(F)** Representative experiment showing D4ER Ca^{2+} imaging traces expressed as a ratio between the Citrine FRET emission and CFP emission (F_{524}/F_{475}) for each condition. Data are normalized to the mean of the first

recorded 100 seconds of the vehicle condition and are represented as percentage (%) of vehicle. **(G)** Baseline ER Ca^{2+} defined as the average F_{524}/F_{475} ratio during the 600 seconds of recording before thapsigargin addition. Data are represented as % of vehicle. **(H)** ER Ca^{2+} efflux following thapsigargin corresponding to average F_{524}/F_{475} ratio recorded during the last 100 seconds of the thapsigargin treatment expressed as a % of the average of the F_{524}/F_{475} ratio recorded at baseline. **(I)** Representative confocal immunofluorescence images of *ASPH*$^{-/-}$ HEK293 transfected as in (B) and treated with 1μM thapsigargin or vehicle for 15 minutes. **(J)** Quantification of co-localized STIM1-myc and Orai1-HA puncta from experiment in (I) (n=27-34 cells per condition). **(K)** Quantification of CFP and YFP co-expressing puncta in *ASPH*$^{-/-}$ HEK293 cells transfected with STIM1-CFP and Orai1-YFP plasmids (n=37-61 cells per condition). **(L-N)** STIM1-CFP and YFP-Orai1 SOCE complex formation measured by FRET. STIM1-CFP/YFP-Orai1 complex formation was triggered by the addition of 3mM EGTA and 1μM thapsigargin 120 seconds after starting recording (n=37-61 cells per condition). **(L)** FRET signal traces averaged from individual cells represented as corrected FRET intensity over CFP intensity ($FRET_{corr}$/CFP). **(M)** Area under the curve (AUC) of $FRET_{corr}$/CFP traces in (L) from baseline to thapsigargin FRET signal from individual cells for each condition. **(N)** Average change in $FRET_{corr}$/CFP from baseline (average $T_{0\text{-}50sec}$) to peak after thapsigargin and Ca^{2+} depletion (average $T_{300\text{-}1000sec}$). Results represent the mean ± SEM; Ordinary one-way ANOVA with Bonferroni's post-tests was used in (C-E), (G-H), (J) and (M-N); Two-way ANOVA with Bonferroni's post-tests was used in (K); ***$P < 0.001$; **$P < 0.01$; *$P < 0.05$. In (K), * represents comparison between and ERGP+VK_1 and every other condition, # represents comparison between vehicle and ERGP, and $ represents comparison between vehicle and VK_1. See also Figure S7.

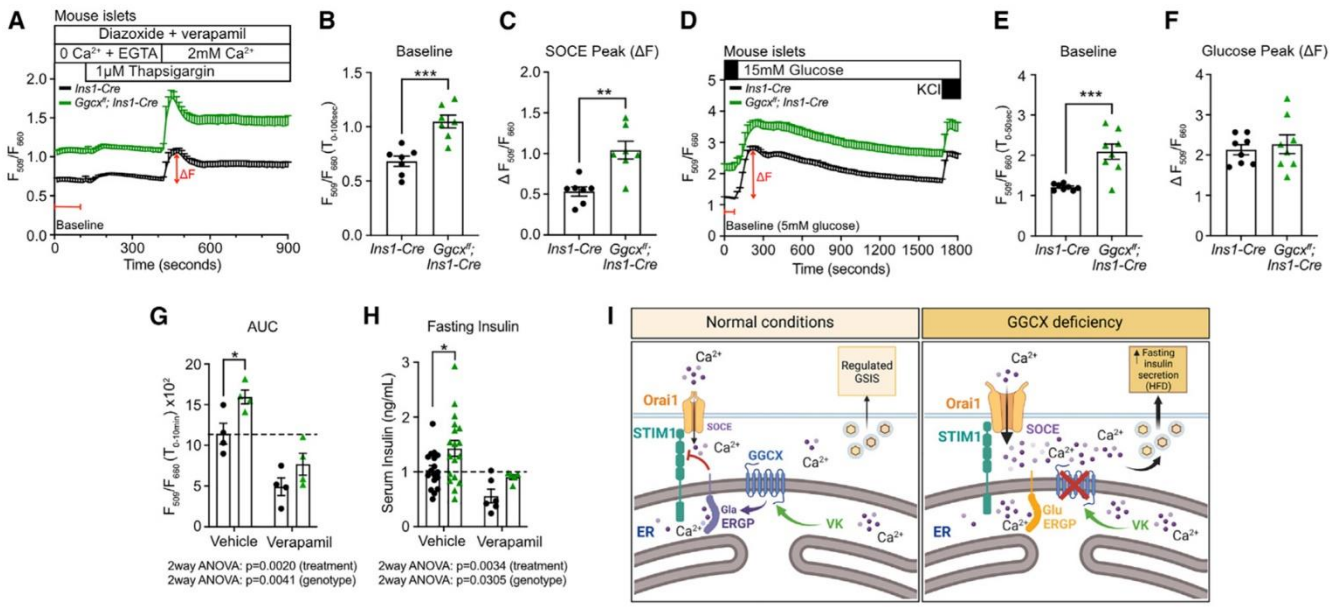

Figure 7: Increased SOCE and basal cytosolic Ca^{2+} in *Ggcx*-deficient β-cells cause impaired fasting hyperinsulinemia. (A) SOCE measured by live-cell Ca^{2+} imaging in semi-dispersed islets from *Ggcx^{ff}; Ins1-Cre* and *Ins1-Cre* mice in buffer containing 5mM glucose (n=7 experimental replicates per condition). **(B-C)** Quantification of **(B)** baseline cytosolic Ca^{2+} level defined as the average F_{509}/F_{660} ratio during the first 100 seconds of recording and **(C)** SOCE peak (ΔF) are represented. **(D)** Cytosolic Ca^{2+} level measured at 5 and 15mM glucose (n=8 experimental replicates per condition). **(E)** Baseline cytosolic Ca^{2+} level during the first 50 seconds of recording and **(F)** glucose-stimulated Ca^{2+} peak (ΔF) quantifications are represented. **(G)** Quantification of Ca^{2+} imaging experiments of semi-dispersed islets from *Ggcx^{ff}; Ins1-Cre* and *Ins1-Cre* mice at 11mM glucose. Data are represented as the area under the curve of the Fluo-4 and Fura Red ratio before and after verapamil addition (n=4). **(H)** Fasting serum insulin level measured in *Ggcx^{ff}; Ins1-Cre* and *Ins1-Cre* mice fed a HFD before and after verapamil treatment (n=5-19). **(I)** Proposed model for the role of γ-carboxylation in β-cells (Created with BioRender.com). Results represent the mean ± SEM; Unpaired, 2-tailed Student's *t* test was used

in (B-C) and (E-F); Two-way ANOVA with Bonferroni's post-tests was used in (G-H); ***P < 0.001; **P < 0.01; *P < 0.05. See also Figure S7.

STAR METHODS

Resource availability

Lead Contact

Further information and requests for resources and reagents should be directed to and will be fulfilled by the lead contact, Mathieu Ferron (mathieu.ferron@ircm.qc.ca).

Materials availability

All unique materials in this study may be made available upon request from the lead contact.

Data and code availability

RNA-seq data have been deposited at GEO and are publicly available as of the date of publication. Accession number is GSE199319.

The mass spectrometry proteomics dataset "Identification of vitamin K-dependent proteins in mouse liver by LC-MS/MS" has been deposited to the ProteomeXchange Consortium via the PRIDE partner repository [64] with the dataset identifier PXD032920 and 10.6019/PXD032920.

The mass spectrometry proteomics dataset "Identification of gamma-carboxyglutamic acid residues in mouse ERGP by LC-MS/MS" have been deposited to the ProteomeXchange

Consortium via the PRIDE partner repository [64] with the dataset identifier PXD032955 and 10.6019/PXD032955.

This paper does not report original code.

Any additional information required to reanalyze the data reported in this paper is available from the lead contact upon request.

Experimental Model and Subject Details

Mice

Ggcx^{ff} mice were generated in our laboratory as described before [13], and maintained on a C57BL/6J genetic background. These mice were bred to the *Pdx1-Cre* (B6.FVB-*Tg(Pdx1-cre)*^{6Tuv}/Nci; National Cancer Institute; Stock 01XL5) [65] or the *Ins1-Cre* (B6(Cg)-*Ins1*$^{tm1.1(cre)Thor}$/J; The Jackson Laboratory; Stock 026801) [66] lines to generate *Ggcx*^{ff}*; Pdx1-Cre* and *Ggcx*^{ff}*; Ins1-Cre* mice. β-cells were labeled with the tdTomato reporter gene by breeding the B6.Cg-*Gt(ROSA)26Sor*$^{tm14(CAG-tdTomato)Hze}$/J (Jackson Laboratory; stock 007914) mice to the *Ins1-Cre* strain. *Vkorc1*^{ff} and *Vkorc1l1*^{ff} mice were generated in our laboratory as described before [13], bred to the *Pdx1-Cre* line to generate *Vkorc1*^{ff}*; Vkorc1l1*^{ff}*; Pdx1-Cre* mice and maintained on a C57BL/6J background. Other previously described mouse strains used in this study include *Vkorc1*$^{-/-}$*; APOE-Vkorc1l1* [26]. Male mice were used in all experiments and littermates with the appropriate genotypes always used as controls. Animals were housed at the IRCM in a pathogen-free facility on a 12h light/dark cycle and fed a normal chow diet (Teklad global 18% protein rodent diet; 2918; Envigo), unless otherwise specified. All animal use complied with the

guideline of the Canadian Committee for Animal Protection and was approved by IRCM institutional animal care committee.

Human islets

Cadaveric human islets were obtained from the IsletCore at the Alberta Diabetes Institute from the University of Alberta (Edmonton, Alberta, Canada)[67] and from the Integrated Islet Distribution Program (IIDP) at City of Hope (Duarte, California, USA). Upon arrival, islets were handpicked and processed for experiments. When needed, human islets were cultured in DMEM (5mM glucose, 10% FBS, penicillin/streptomycin) in an incubator at 37ºC, 5% CO_2. Detailed protocols for islet isolation and static glucose-stimulated insulin secretion are available in the protocols.io repository [68] and on the IIDP website (iidp.coh.org). Donor characteristics are described in Table S1. Islet isolation was approved by the Human Research Ethics Board at the University of Alberta (Pro00013094). All donors' families gave informed consent for the use of pancreatic tissue in research. The IRCM Human Ethics committee approved human islets use.

Cell lines

Rat insulinoma cell line INS-1 832/3 (Millipore Sigma) was cultured in RPMI-1640 supplemented with 2mM L-Glutamine, 1mM sodium pyruvate, 10mM HEPES, 0.05 mM β-mercaptoethanol, 10% fetal bovine serum (FBS) and penicillin/streptomycin as previously described [69]. HEK293 cells (ATCC) were cultured in EMEM supplemented with heat-inactivated 10% FBS and penicillin/streptomycin. Cells were cultured at 37ºC with 5% CO_2.

Generation of *ASPH*$^{-/-}$ HEK 293 cells by CRISPR-Cas9

HEK 293 cells were transfected with single guide RNA (sgRNA; Thermo Fisher) and recombinant *Streptococcus pyogenes* Cas9 protein (SpCas9; Synthego) using Lipofectamine CRISPRMAX Cas9 Transfection reagent (CMAX00001; Thermo Fisher) according to the manufacturer protocol. We selected a sgRNA (Assay ID: CRISPR671774_SGM; Target DNA Sequence: GGACATCTGTAGCTGTCGTT) matching a sequence in the exon 2 of the gene *ASPH* which is shared by all the isoforms encoded by this gene, including ASPH, junctate, junctin and ERGP proteins. Forty-eight hours after the transfection, cells were diluted and seeded in 96-wells plates to establish clonal lines. A total of ninety-six clones were screened by standard Sanger DNA sequencing of the targeted region and the sequence analyzed using the Inference of CRISPR Edits (ICE) Analysis tools of Synthego (https://ice.synthego.com/). Two clones with frameshift-inducing indel on all alleles of *ASPH* were selected and loss of expression of ASPH and ERGP confirmed by western blot experiment and by quantitative PCR (Fig. S7A-B).

Rats and glucose infusions

Two-month-old male Wistar rats (Charles River, Saint-Constant, QC, Canada) underwent catheterization of the jugular vein for infusions and the carotid artery for sampling as described [70]. Animals were randomized into two groups receiving 0.9% saline (Baxter, Mississauga, ON, Canada; SAL) or 70% dextrose (McKesson, Montreal, QC, Canada; GLU) as described [71]. The glucose infusion rate was adjusted to maintain plasma glucose between 13.9 and 19.4 mmol/l throughout the 72h infusion. All procedures were approved by the Institutional Committee for the Protection of Animals at the Centre Hospitalier de l'Université de Montréal.

Method Details

Mouse islet isolation, cell sorting and culture

Mice were anesthetized by intraperitoneal (i.p.) injection of a drug mixture of ketamine hydrochloride and xylazine, sacrificed via cervical dislocation and exsanguinated. The pancreatic duct was perfused with Liberase TL (Roche Applied Science) in Hank's balanced salt solution (HBSS) containing Ca^{2+}/Mg^{2+} and the inflated pancreas was excised and incubated at 37ºC for 30 minutes with firm agitation at the 15-minute mark. The digested pancreas was then washed 4 times by decantation with HBSS containing 0.1% BSA and 20mM HEPES pH 7.4, and islets were isolated using Histopaque-1077 density gradient separation (Millipore Sigma). Islets were then transferred to culture media (RPMI, 10% FBS, penicillin/streptomycin) and handpicked under a stereomicroscope (SteREO Discovery.V12; Zeiss).

Islets from *Ins1*$^{Cre/+}$; *Rosa26*$^{CAG\text{-}lox\text{-}stop\text{-}lox\text{-}tdTomato}$ mice were dissociated by incubating at 37ºC for 2 minutes using 0.05% Trypsin-ETDA and pipetting. β-cells (Tom+) and the other islet endocrine cells (Tom-) were sorted out based on tdTomato expression using the FACSAria III cell sorter (Becton Dickinson). Dead cells were excluded based on DAPI staining and only singlets were sorted. Cells were lyzed directly after sorting either in guanidium thiocyanate lysis solution for RNA extraction or in 1% triton lysis buffer for protein extraction.

INS-1 832/3 and islet treatments

To test the presence of γ-carboxylation, INS-1 832/3 cells and human islets were cultured in their respective culture media containing either VK_1 (22μM; V3501; MilliporeSigma), warfarin (50μM; SC-204941; Santa Cruz Biotechnology), or vehicle during 3 days before analysis. To test the effect of glucose on γ-carboxylation, INS-1 832/3 cells, human islets and wild-type mouse

islets were culture in their respective media containing different concentration of glucose during 3 days before analysis. To test the protective effect of VK_1 on ER stress induced cell death, INS-1 832/3 cells were cultured with VK_1 (22μM) or vehicle for 48 hours before being cultured for 24 hours in media containing 25mM glucose and thapsigargin (10, 20 and 40 nM). The dose of 22 μM (10 μg/ml) of VK_1 was selected based on previous reports showing that maximal γ-carboxylation of known Gla proteins was achieved with VK_1 concentration of >1-20 μM in cell culture [72, 73].

Metabolic analysis

For mice fed a regular chow diet, metabolic analysis was performed as follows. For intraperitoneal glucose tolerance tests (IPGTT), mice were fasted for 16 hours, and blood glucose levels were measured after fasting and at 15-, 30-, 60- and 120-minutes following i.p. injection of glucose (2g/kg of BW). To measure circulating insulin concentration following a bolus of glucose, tail vein blood was collected after a 16-hour fasting and at 15- and 30-minutes post-injection (i.p.) with glucose (3g/kg of BW). Serum insulin was measured using ELISA (Insulin ELISA mouse; Mercodia). Insulin tolerance test (ITT) was performed after 5 hours of fasting following i.p. injection of insulin (1U/kg; Humulin R, Lilly) and blood glucose was measured after fasting and 30-, 60-, 90- and 120-minutes post-injection.

For short high fat diet (HFD) feeding, 10-weeks old mice were fed either a lard-based diet (60% kcal from fat; TD.06414; Envigo) or an ingredient matched control diet (10% kcal from fat; TD.08806; Envigo) for 7 days, after which body weight, random fed blood glucose and metabolic tests were performed. For circulating insulin measurements, tail vein blood glucose

was collected after 5 hours of fasting and at 15- and 30-minutes post-injection (i.p.) with glucose (2g/kg). Serum insulin was measured using ELISA and data represented in absolute value or as stimulation index (insulin concentration at 15 or 30 minutes / insulin concentration at fasting). For IPGTTs, tail vein blood glucose was measured after 5 hours of fasting and at 15-, 30-, 60- and 120-minutes post-injection with glucose (1.5g/kg). For oral glucose tolerance tests (OGTTs), tail vein blood glucose was measured after 5 hours of fasting and at 15-, 30-, 60- and 120-minutes post-gavage with glucose (1.5g/kg). For ITTs, tail vein blood glucose was measured after a 5-hour fasting and at 30-, 60-, 90- and 120-minutes post-injection (i.p.) with insulin (0.75U/kg). Homeostatic model assessment of insulin resistance (HOMA-IR) was calculated as follows: Fasting glucose (mM) x Fasting insulin (μU/mL)/22.5 [74]. When indicated, following 7 days of HFD feeding, verapamil (V4629, Sigma) was added to the drinking water (1mg/mL) of the mice for 5 days while fed an HFD.

O_2 consumption, CO_2 release, food intake and physical activity were analyzed using an 8-chamber Promethion Continuous Metabolic System (Sable Systems International) as before [75]. Briefly, after a 48-hour acclimation period, data were collected for 96 hours. Energy expenditure (kcal/hour) was calculated by indirect calorimetry using the following formula: 60 x (0.003941 x VO_2 (ml/min) + 0.001106 x VCO_2 (ml/min)). Physical activity was measured as beam breaks for the x-, y- and z-axis using infrared beams connected to the system.

Ex vivo glucose-stimulated insulin secretion (GSIS)

Islets from *Ggcx^{ff}; Pdx1-Cre* and *Pdx1-Cre* mice were isolated and left in culture media (RPMI, 10% FBS, penicillin/streptomycin) for recovery for 40 hours. Islets were hand-picked and

quickly washed in Krebs-Ringer bicarbonate HEPES (KRBH) buffer (114mM NaCl, 2.5mM $CaCl_2$, 1.2mM KH_2PO_4, 4.7mM KCl, 1.16mM $MgSO_4$, 25.5mM $NaHCO_3$, 10mM HEPES and 0.1% fatty acid free BSA, pH 7.35) containing 5.6mM glucose, and then pre-incubated two times for 1 hour at 37°C. Groups of 10 similarly sized islets were transferred to microtubes containing 5.6mM glucose KRBH and incubated for 1h at 37°C. Islets were then incubated in KRBH buffer containing 11.1mM glucose, followed by KRBH buffer containing 16.7mM glucose, each incubation for 1 hour at 37°C. After each incubation, supernatant was collected and at the end of the protocol, islets were lyzed in 0.18N HCl, 75% EtOH extraction buffer. Insulin was measured in the different fractions by ELISA (Mercodia). Islets insulin content was used to normalize insulin secretion.

Pancreas immunohistochemistry, immunofluorescence and insulin content

Pancreases were weighed and fixed in 10% formalin for 24 hours at room temperature, embedded in paraffin and sectioned at 5μm. For immunohistochemistry and immunofluorescence experiments, rehydration was followed by an antigen retrieval step (sub-boiling for 10 minutes in 10mM sodium citrate pH 6.0).

For β-cell mass quantifications, insulin was detected using rabbit anti-insulin antibodies (1:200, sc-9168; Santa Cruz Biotechnology), Vectastain Elite ABC-peroxidase kit (Vector Laboratories; PK-6101) and NovaRED Substrate Kit (Vector Laboratories; SK-4800) following manufacturer's instructions. Pancreas tissue was counterstained using Mayer's hematoxylin and histomorphometric analyses were performed using the OsteoMeasure Analysis System

(Osteometrics). β-cell mass was calculated as follows: β-cell area (%) x pancreas weight (mg) / 100.

For immunofluorescence, blocking was performed in PBS containing 5% normal donkey serum and 0.3% Triton for 1 hour at room temperature. Sections were then incubated with antibodies diluted in PBS, 1% BSA and 0.1% Triton, first with goat anti-insulin antibodies (sc-7839; Santa Cruz Biotechnology) and rabbit anti-A/E-GRD antibodies (generated in our laboratory, see below) over-night at 4ºC, and second with Alexa-Fluor 594- conjugated donkey anti-goat (705-585-147; Jackson Immunoresearch Laboratories) and Alexa-Fluor 488-conjugated donkey anti-rabbit (711-545-152; Jackson Immunoresearch Laboratories) antibodies for 1 hour at room temperature. Specificity of anti-A/E-GRD antibodies was assessed by competition with recombinant 6XHIS-A/E-GRD protein (25μg/mL) during incubation with the primary antibodies. Nuclei were stained with DAPI. Volocity 6.0 quantitation module was used to threshold for and select $Insulin^+$ cells and to determine the intensity of the A/E-GRD signal in $Insulin^+$ areas.

For apoptosis detection, the Click-iT Plus TUNEL Assay kit (C10617; Invitrogen) was used following manufacturer's instructions except the proteinase K treatment was replaced by a 10-minute incubation in citrate buffer. Goat anti-insulin antibodies (sc-7839; Santa Cruz Biotechnology) and Alexa-Fluor 594- conjugated donkey anti-goat antibodies (705-585-147; Jackson Immunoresearch Laboratories) were used as described above. Nuclei were stained with DAPI. $Insulin^+$ $TUNEL^+$ cells were detected using the automated DM5500B fluorescence

microscope (Leica) with a Retiga EXi (QImaging) and 40X objective. Volocity 6.0 quantitation module was used to threshold for and count Insulin$^+$ cells with TUNEL$^+$ nuclei.

For pancreatic insulin content measures, each pancreas was weighed and homogenized in an acid-ethanol buffer (1.5% HCl; 70% EtOH) after overnight fasting and 2 hours of refeeding. Samples were neutralized using 1M Tris-HCl pH 7.5 (1:1) and insulin measured by ELISA (Mercodia). Insulin content was normalized to the pancreas weight.

RNA isolation and qPCR

For mouse and human islets gene expression analysis, 20-40 handpicked islets per mouse or donor were lyzed in guanidium thiocyanate lysis solution, and tRNA (20ug) was added before total RNA was isolated as described [76]. Samples were then treated with DNaseI (18068015; Invitrogen), and mRNA reversed transcribed using M-MLV reverse transcriptase (28025013; Invitrogen) and random hexamers and oligo dT primers. Relative gene expression was quantified using PowerUp SYBR Green Master Mix (A25741; Applied Biosystems) and ViiA7 Real-Time PCR System (Applied Biosystems).

DNA constructs and transfections

Mouse ASPH-3XFLAG and ERGP-3XFLAG plasmids were generated by PCR amplification using pENTR223.1-ASPH (Clone ID: BC166658; Transomic Technologies) as a template and cloning in the HindIII and BamHI restriction sites of the p3XFLAG-CMV-14 expression vector (MilliporeSigma). ASPH-3XFLAG and ERGP-3XFLAG deletion mutants were generated by PCR using Q5 High Fidelity DNA polymerase (M0491; NEB) and primers extending in opposite

directions and flanking the region to be deleted. ERGP DNA fragments containing glutamic acid to aspartic acid point mutations were synthesized (Genscript) and cloned into ERGP-3XFLAG plasmid via an internal StuI site and the 3' BamHI site. Mouse Orai-HA was generated in two steps. First, the 3' section of Orai1 ORF was cloned from pCMV-SPORT6-Orai1 (BC023149; Transomic Technologies) in the EcoRI and XbaI restriction sites of a pcDNA3.1-Myc-His B expression vector with an HA tag. The missing 5' section of Orai1 ORF was cloned from mouse osteoblast cDNA in the EcoRI and Orai1 internal ApaI restriction sites. Mouse pcDNA3.1-Stim1-Myc plasmid was obtained from Addgene (17732)[77]. Using the above-mentioned constructs as template, STIM1-CFP and YFP-Orai1 were inserted into the pcDNA3.1-Myc-His B vector using Gibson assembly. pcDNA-D4ER plasmid was previously described and obtained from Dr. Diana Pendin [50].

HEK293 cells were transfected with "tagless" pCDNA3.1-GGCX and pCDNA3.1-VKORC1 to ensure maximal γ-carboxylation, and with the indicated plasmids using Lipofectamine 2000 transfection reagent (11668019; Invitrogen) following manufacturer's instructions. Six hours post-transfection, media was changed and VK_1 (22μM) or warfarin (50μM) was added when specified. Generation of a clonal cell line stably expressing ERGP-3XFLAG was generated via transfection of HEK293 cells with the pERGP-3XFLAG-CMV-14 plasmid previously linearized by digestion with ScaI. Cells with integration of the plasmid were selected using G418 antibiotics and isolated colonies were expanded. ERGP expression was assessed by western blot using anti-FLAG antibodies and immunofluorescence confirming clonality.

Ca^{2+} overlay

HEK293 cells stably expressing mouse ERGP-3XFLAG, and transfected with GGCX and VKORC1, were cultured in the presence of either VK_1 (22μM) or warfarin (10μM). Purified γ-carboxylated and uncarboxylated ERGP-3XFLAG proteins were resolved by SDS-PAGE, transferred to a nylon membrane and cross-linked with 0.5% glutaraldehyde. The membrane was quenched with 50mM glycine and washed 3 times with binding buffer containing 60mM KCl, 5mM $MgCl_2$, 10mM imidazole-HCl, pH 6.8, and then incubated with radiolabelled binding buffer containing 8.8μM $^{45}CaCl_2$ (PerkinElmer) for 1 hour, washed with distilled H_2O and dried. Radioactivity was captured by a storage phosphor screen and detected by a laser scanner imaging system (Typhoon FLA 9500; Cytiva).

Generation of rabbit polyclonal anti-ASPH/ERGP-GRD (anti-A/E-GRD) antibodies

Rabbit ERGP ER luminal domain anti-serum was generated by immunizing rabbits with a 6XHIS tagged protein containing amino acid 85-310 of ERGP (MediMabs). Antibodies specific to the glutamic acid rich domain (GRD) were affinity purified using a GST-tagged protein corresponding to the GRD. The specificity of the antibody towards the GRD of ERGP and ASPH was tested by western blot.

Immunoprecipitation and western blot

Cells or tissues were homogenized in lysis buffer containing 20mM Tris-HCl (pH 7.5), 150mM NaCl, 1mM EDTA (pH 8.0), 1mM EGTA, 2.5mM NaPyrophosphate, 1mM β-glycerophosphate, 10mM NaF, 1% Triton, 1mM phenylmethylsulfonyl fluoride (PMSF) and protease inhibitors (4693132001; Roche Diagnostics). For anti-Gla immunoprecipitation, 200μg of protein extracts was incubated with 10μg of rabbit anti-Gla antibodies overnight with rotation at 4ºC followed by

3 hours incubation with Protein A-Agarose beads (11719408001; Roche Diagnostics) and washed 4 times with lysis buffer. Immunoprecipitated proteins were heated at 70ºC in Laemmli buffer for 10 minutes before resolving on a 7.5% polyacrylamide Tris-Glycine gels. Proteins were detected using standard western blot procedures with rabbit anti-GGCX (16209-1-AP; ProteinTech) or rabbit anti-A/E antibodies generated in our laboratory (see above). For anti-A/E-GRD IP, the same procedure was followed. FLAG-tagged proteins were immunoprecipitated from 100µg of protein extracts using anti-FLAG agarose beads (A2220; MilliporeSigma) incubated for 2 hours with rotation at 4ºC. Densitometry analyses were performed with the Image Lab software (version 5.0; Bio-Rad Laboratories).

Other antibodies used for western blot in this study include rabbit anti-VKORC1 generated in our laboratory and previously reported [13], rabbit anti-cleaved Caspase-3 (9661; Cell Signaling), rabbit anti-phospho(Ser139)-Histone H2A.X (9718; Cell Signaling), rabbit anti-phospho(S724)-IRE1 (ab124945, Abcam), rabbit anti-GRP78/BIP (11587-1-AP, Proteintech), rabbit anti-GFP (50430-2-AP, Proteintech), mouse anti-β-Actin (A1978; MilliporeSigma), rabbit anti-GAPDH (5174; Cell Signaling), mouse anti-Myc (2276; Cell Signaling), rabbit anti-HA (3724; Cell Signaling), mouse anti-FLAG (F1804; MilliporeSigma) and rabbit anti-FLAG (14793; Cell Signaling). To detect VKORC1, cleaved Caspase-3 and p(Ser139)-Histone H2A.X, proteins were resolved on 10% polyacrylamide Tris-Tricine gels.

Ca^{2+} live-cell imaging in *$ASPH^{-/-}$* HEK293 and islets

$ASPH^{-/-}$ HEK 293 cells were transfected with 0.5µg GGCX, 0.5µg VKORC1, 0.44µg STIM1-Myc, 0.22µg Orai1-HA, 0.33µg ERGP-3XFLAG or p3XFLAG-CMV-14 empty vector as

indicated in 35mm culture dishes and the next day cells were plated on poly-L-lysine (P1274; MilliporeSigma) coated glass coverslips (18mm diameter, #1.5 thickness; 72290-08; Electron Microscopy Sciences). Coverslips were coated with 0.1mg/mL poly-L lysine in sterile ddH_2O at room temperature for 1 hour, before being washed three times with sterile ddH_2O and left to dry for 2 hours. *ASPH*$^{-/-}$ HEK 293 cells were loaded with 5μM Fluo-4 AM (F14201; Invitrogen) and 2.5μM Fura Red AM (F3021; Invitrogen) in a HEPES-buffered saline solution (HBSS; 120mM NaCl, 5mM KCl, 0.8mM $MgSO_4$, 2mM $CaCl_2$, 10mM Glucose, 20mM HEPES, pH 7.4) containing 0.02% pluronic F-127 (P6866; Invitrogen) at 37ºC for 30 minutes. Cells were then washed twice with HBSS and incubated for an additional 30 minutes at 37ºC to allow complete de-esterification of intracellular AM esters. Ca^{2+} imaging was performed in Ca^{2+} free HBSS containing 1mM EGTA. Baseline measurements (F0) were recorded for 120 seconds before ER Ca^{2+} stores were depleted by adding thapsigargin (final 1μM) and SOCE was triggered by adding $CaCl_2$ (final [Ca^{2+}] 2mM) 420 seconds after starting recording. For measurements using the D4ER Ca^{2+} probe, *ASPH*$^{-/-}$ HEK293 cells were transfected with 0.2μg D4ER, 0.4μg GGCX, 0.4μg VKORC1, 0.44μg STIM1-Myc and 0.22μg Orai1-HA and 0.33μg ERGP-3XFLAG or p3XFLAG-CMV-14 empty vector. The cells were equilibrated in HBSS for 45 minutes at 37ºC before being imaged in Ca^{2+} free HBSS containing 1mM EGTA. Baseline measurements were recorded for 600 seconds before ER Ca^{2+} stores were depleted by adding thapsigargin (final 1μM). The Ca^{2+} ionophore ionomycin (final 3μM) and $CaCl_2$ (final [Ca^{2+}] 2mM) were added 1200 seconds after starting recording. Imaging of HEK293 cells was performed at 37ºC.

Isolated mouse islets were semi-dispersed by digestion with 0.025% Trypsin-ETDA for 1 minute followed by up and down pipetting then transferred to culture media (RPMI, 10% FBS,

penicillin/streptomycin) containing 22μM VK_1. Semi-dispersed islets enclosed in 200 μL droplets (corresponding to approximately 100 islets) were plated on glass coverslips and allowed to attach for 30 minutes at 37°C, before adding 1mL of culture media for over-night recovery. Islet cells were then loaded with 5μM Fluo-4 AM and 2.5μM Fura Red AM in KRBH buffer (114mM NaCl, 1.2mM KH_2PO_4, 4.7mM KCl, 1.16mM $MgSO_4$, 25.5mM $NaHCO_3$, 2.5mM $CaCl_2$, 5mM Glucose, 20mM HEPES, 0.2% fatty acid free bovine serum albumin [BSA]) for 30 minutes at room temperature. Baseline fluorescence ratio (F0) was measured for 90 seconds and response to 15mM glucose was recorded during 90-1700 seconds before KCl concentration was raised to 30mM. SOCE in islet cells was measured as described above for HEK293 but in KRBH buffer containing 200μM diazoxide (D9035; MilliporeSigma), an opener of the β-cell ATP sensitive K^+ channel in beta cells, and 10μM verapamil (V4629; Millipore Sigma), a voltage gated Ca2+ channel blocker, for the duration of imaging. In other experiments, the effect of verapamil on cytosolic Ca^{2+} levels of semi-dispersed islets was measured as described above, but in KRBH buffer containing 11mM glucose to mimic in vivo conditions. The semi-dispersed islets were first imaged for 600 seconds following vehicle (DMSO) treatment, then were imaged for an additional 600 seconds following treatment with 50μM verapamil. Imaging for islets was performed at 32°C and 5% CO_2 enrichment.

Imaging was performed on a confocal rotary disk inverted microscope from Zeiss equipped with a Yokogawa CSU-1 module using a 20X objective. The microscope stage contained a conduction heater and was enclosed in an incubator to maintain cells at the desired temperature and CO_2 percentage. Fluo-4 was excited with a 488nm laser and emission was recorded at 509nm (ZEN blue software). Laser power was set to 5%, exposure to 250ms, and EM gain to

500. One image was taken every 5 seconds. Fura Red was excited with a 488nm laser and emission was recorded at 660nm. Laser power was set to 20%, exposure to 500ms, and EM gain to 750. One image was taken every 5 seconds. D4ER reports ER Ca^{2+} level via FRET between its CFP and Citrine domains, which come into closer proximity following Ca^{2+} binding of its D4 and calreticulin domains. To record the CFP donor signal, D4ER was excited with a 405nm laser then emission recorded at 475nm. To record the FRET signal from Citrine, D4ER was excited with a 405nm laser then emission recorded at 524nm. Laser power was set to 20%, exposure to 500ms, and EM gain to 750 to record CFP. Laser power was set to 20%, exposure to 500ms, and EM gain to 500 to record Citrine FRET.

Quantification was performed using Fiji [78]. Timelapses were 16-bit greyscale image stacks saved as Carl Zeiss Image data format files. Individual cells or islet clusters were selected as freehand selections to generate regions of interest (ROI). The mean gray value of each ROI was then measured for each image (1 per 5 seconds) for each channel (Fluo-4/Fura Red or Citrine/CFP). Cells that did not stay attached during the entire protocol were excluded from analysis. Fluo-4 fluorescence intensity was divided by Fura Red intensity to generate a ratiometric measurement of cytosolic Ca^{2+} as previously described [79]. Similarly, the intensity of the FRET signal from Citrine was divided by the CFP intensity to generate a ratiometric measurement of ER Ca^{2+} for the experiments using the D4ER probe as previously described [50]. The FRET-Citrine/CFP ratio was then normalized to the mean of the first 100 seconds recorded for the vehicle condition (i.e., without VK_1 and without ERGP) and represented as % of vehicle. A total of n=54-130 *ASPH*$^{-/-}$ HEK 293 cells were averaged together for each experiment for cytosolic or ER Ca^{2+} measurements, and n=9-14 independent experiment per condition were

analyzed. In semi-dispersed islet imaging experiments, 82-240 islet cell clusters were averaged for each experiment, and n=7-8 independent experiment per condition were analyzed.

STIM1/Orai1 puncta quantification by immunofluorescence

ASPH$^{-/-}$ HEK293 cells were transfected with GGCX, VKORC1, STIM1-myc, and Orai1-HA and ERGP-3XFLAG or p3XFLAG-CMV-14 empty vector, and plated on poly-L-lysine coated glass coverslip as detailed in the Ca^{2+} live-imaging section. Two days later, cells were equilibrated in HBSS for 45 minutes and treated with 1μM thapsigargin for 15 minutes in Ca^{2+} free HBSS containing 1mM EGTA. Cells were then fixed in 4% paraformaldehyde in PBS for 15 minutes at room temperature and washed 3 times with PBS. Cells were stained using mouse anti-Myc (Cell Signalling; 2276) and rabbit anti-HA (Cell Signalling; 3724) antibodies as detailed in the immunofluorescence section and imaged with a 63x objective.

Quantification of puncta was performed using the Volocity 6.0 quantitation module. Puncta were determined by adjusting an intensity threshold and including only objects measuring between 0.1-and 1.0μm^2. Saturated pixels were excluded from quantification. STIM1/Orai1 co-expressing puncta in *ASPH*$^{-/-}$ HEK293 cells were defined as areas of overlapping STIM1 and Orai1 expression in objects between 0.1-1.0μm^2 in surface area. On average a cell contains 0-120 puncta in the absence of thapsigargin and 15-413 puncta following thapsigargin treatment. The number of STIM1/Orai1 colocalized puncta per cell was normalized to the cell area in μm^2 (n=27-34 cells per condition, from 3 independent experiments). Islet clusters stained for STIM1 (rabbit anti-STIM1; 5668; Cell Signaling) contained on average 0-57 puncta at steady state (KRBH buffer with 5mM glucose). The number of STIM1 puncta per islet cluster was

normalized to the cluster area in μm^2 (n=116-183 islets clusters per condition, from 2 independent experiments).

STIM1/Orai1 FRET measurements

ASPH$^{-/-}$ HEK293 cells were transfected with 0.4μg GGCX, 0.4μg VKORC1, 0.44μg STIM1-CFP, 0.42μg YFP-Orai1 and 0.33μg ERGP-3XFLAG or p3XFLAG-CMV-14 empty vector and plated on poly-L-lysine coated glass coverslips the next day as detailed in the Ca^{2+} live-cell imaging section. Two days later, cells were washed twice with HBSS and imaged for 120 seconds before 1μM thapsigargin and 3mM EGTA was added to deplete ER Ca^{2+} stores and chelate extracellular Ca^{2+}. Transfection were optimized to get <2-fold difference between STIM1-CFP and YFP-Orai1 expression levels. Images were recorded every three seconds with the 63X objective of a confocal rotary disk inverted microscope as described in the Ca^{2+} live-cell imaging section.

STIM1-CFP was excited with a 405nm laser and emission was recorded at 475nm. Laser power was set to 20%, exposure to 750ms, and EM gain to 750. YFP-Orai1 was excited with a 488nm laser and emission was recorded at 524nm. Laser power was set to 10%, exposure to 250ms, and EM gain to 500. FRET signal was excited with the 405nm laser and emission was recorded at 524nm. Laser power was set to 20%, exposure to 500ms, and EM gain to 500.

Quantification was performed using Fiji [78] as previously described [80, 81]. Time lapse images were 16-bit greyscale image stacks saved as Carl Zeiss Image data format files. Each timepoint contained three images representing the CFP, YFP, and FRET channels. Individual

cells were selected manually using the freehand ROI selection tool. Identical ROIs were used across timepoints and channels for each time lapse. An ROI containing no cells was also selected on each time lapse and used to subtract the background value of each channel. For each imaging experiment, cells transfected with STIM1-CFP or YFP-Orai1 alone were used to calculate bleed-through of the CFP or YFP signals into the FRET channel. The bleed-through coefficient for CFP (A) and YFP (B) were individually calculated, using linear regression of CFP or YFP intensity in their respective channels compared to the signal in the FRET channel.

Corrected FRET signal was defined as follows:

$FRET_{corr} = FRET - ([A \times CFP] + [B \times YFP])$

Where FRET is the fluorescent intensity at 524nm from the FRET channel, CFP is the fluorescent intensity at 475nm from the CFP channel, YFP is the fluorescent intensity at 524nm from the YFP channel, A is the CFP-FRET bleed-through coefficient determined by imaging CFP only cells, and B is the YFP-FRET bleed-through coefficient determined by imaging YFP only cells. Corrected FRET was divided by CFP intensity to control for transfection efficiency ($FRET_{corr}$/CFP). A total of n=37-61 cells, from 3 independent experiments, were averaged together for each condition.

Area under the curve (AUC) of $FRET_{corr}$/CFP traces were calculated with baseline AUC subtraction.

RNA-sequencing

Total RNA from islets was extracted using the RNeasy Plus Mini Kit (74134; Qiagen) following manufacturer's instructions (n=4 for each genotype). RNA integrity was evaluated using the 2100 Bioanalyzer system (Agilent) and samples with RIN >7.5 were used. From 1μg of total RNA, poly(A)+ transcripts were enriched using the NEBNext Poly(A) Magnetic isolation module (E7490; NEB) and libraries prepared using the KAPA stranded RNA-seq library preparation kit (KR0934; Roche Diagnostics) and the TruSeq DNA library Prep LT kit (Illumina) according to the manufacturer's procedures. Clustering of the equimolar libraries in the flowcell was performed using the HiSeq PE cluster kit v4 cBot (PE-401-4001; Illumina) and the cBot cluster generation system (Illumina). Sequencing was performed at the Génome Québec Innovation Center using the Illumina HiSeq 2500 system (average of 56 million paired end reads (PE50) per sample). The quality of the raw reads was assessed with FASTQC v0.11.8. After examining the quality of the raw reads, no trimming was deemed necessary. The reads were aligned to the GRCm38 genome with STAR v2.7.6a with more than 87% of reads uniquely mapped. Raw counts were computed using FeatureCounts v1.6.0 based on Ensembl mouse reference genome v101. Differential expression was performed using the DESeq2 R package and 319 differentially expressed genes (DEGs) were obtained using p-adjusted ≤ 0.05. Gene set enrichment and gene network analyses were performed using StringDB (https://string-db.org/)[82] interrogating Biological Process (Gene Ontology), KEGG Pathways and Annotated Keywords (UniProt). Enrichment was considered significant if the false discovery rate was <0.05 and only networks of 800 or fewer genes were considered for the analysis. Previously published transcriptomic analysis of islets from pre-diabetic (5-weeks old C57BL/6 mice fed a HFD for 8 weeks) or diabetic (8-weeks old *Lepr*$^{db/db}$ and 7-weeks old *Ire1α*^{ff}*; Ins2-Cre*$^{ERT/+}$) mouse models [31-33], were downloaded directly from the publications or from GEO

(https://www.ncbi.nlm.nih.gov/geo/). Up-regulated and down-regulated genes for each model were selected using different p-adjusted values to limit the variability in the total number of genes included in each list: p<0.05 for *Lepr*$^{db/db}$, p<0.01 for HFD and p<0.001 for *Ire1α*^{ff}*; Ins2-Cre*$^{ERT/+}$. Overlap between the various transcriptomes was next determined using jvenn (http://jvenn.toulouse.inra.fr/app/example.html)[83]. The statistical significance between each pair of comparisons was computed using an online tool (http://nemates.org/MA/progs/overlap_stats.html).

Identification of carboxylated proteins by LC-MS/MS

Livers from 5-day old WT and *Vkorc1*$^{-/-}$ mice, or INS-1 832/3 cells cultured with VK_1, 25mM glucose with or without 20nM thapsigargin, were homogenized in lysis buffer and carboxylated proteins immunoprecipitated as described above followed by three washes with 50mM ammonium bicarbonate. Immunoprecipitated proteins were then digested on-bead with trypsin at 37ºC for 18 hours using 0.25ug of Sequencing grade trypsin (Promega). The samples were then reduced with 9 mM dithiothreitol at 37ºC for 30 minutes and, after cooling for 10 minutes, alkylated with 17 mM iodoacetamide at room temperature for 20 minutes in the dark. The supernatants were acidified with trifluoroacetic acid and cleaned from residual detergents and reagents with MCX cartridges (Waters Oasis MCX 96-well Elution Plate) following the manufacturer's instructions. After elution in 10% ammonium hydroxide /90% methanol (v/v), samples were dried with a Speed-vac, reconstituted under agitation for 15 min in 11 µL of 2%ACN-1%FA and 2.4% of each sample was loaded into a 75 µm i.d. × 150 mm Self-Pack C18 column installed in the Easy-nLC II system (Proxeon Biosystems). The buffers used for chromatography were 0.2% formic acid (buffer A) and 90% acetonitrile/0.2% formic acid (buffer

B). Peptides were eluted with a two slopes gradient at a flowrate of 250 nL/min. Solvent B first increased from 2 to 44% in 100 min and then from 44 to 88% B in 20 min. The HPLC system was coupled to Orbitrap Fusion mass spectrometer (Thermo Scientific) through a Nanospray Flex Ion Source. Nanospray and S-lens voltages were set to 1.3-1.7 kV and 50 V, respectively. Capillary temperature was set to 225 °C. Full scan MS survey spectra (m/z 360-1560) in profile mode were acquired in the Orbitrap with a resolution of 120,000 with a target value at 3e5. The 25 most intense peptide ions were fragmented in the HCD cell and analyzed in the linear ion trap with a target value at 2e4 and a collision energy at 29. Target ions selected for fragmentation were dynamically excluded for 30 sec after 2 MS/MS events.

The peak list files were generated with Proteome Discoverer (version 2.3) using the following parameters: minimum mass set to 500 Da, maximum mass set to 6000 Da, no grouping of MS/MS spectra, precursor charge set to auto, and minimum number of fragment ions set to 5. Protein database searching was performed with Mascot 2.6 (Matrix Science) against the UniProt Mus Musculus protein database. The mass tolerances for precursor and fragment ions were set to 10 ppm and 0.6 Da, respectively. Trypsin was used as the enzyme allowing for up to 1 missed cleavage. Cysteine carbamidomethylation was specified as a fixed modification, and methionine oxidation, glutamic acid carboxylation and phosphorylation S/T/Y as variable modifications. Data interpretation was performed using Scaffold (version 4.8) using a peptide threshold of 80%, a protein threshold of 95% and one peptide minimum. We considered a protein as being carboxylated when the average exclusive spectrum count in WT samples was at least double of the *Vkorc1*$^{-/-}$ samples. To minimize the potential identification of proteins non-specifically binding the anti-Gla antibodies or the agarose-beads, we excluded proteins with more than 2

exclusive spectrum counts in the *Vkorc1*$^{-/-}$ samples or with a difference of less than 2 between the WT and *Vkorc1*$^{-/-}$ samples.

Identification of carboxylated residues in ERGP by LC-MS/MS

HEK293 cells stably expressing mouse ERGP-3XFLAG were cultured in the presence of either VK_1 (22μM) or warfarin (10μM) for at least 2 weeks, and carboxylated and uncarboxylated ERGP-3XFLAG were purified with anti-FLAG agarose beads (A2220; MilliporeSigma). On-bead proteins were first diluted in 2M Urea/50mM ammonium bicarbonate, and on-bead chymotrypsin digestion was performed overnight at 37ºC. The supernatants were acidified with trifluoroacetic acid and cleaned from residual detergents and reagents with MCX cartridges (Waters Oasis MCX 96-well Elution Plate) following the manufacturer's instructions. After elution in 10% ammonium hydroxide /90% methanol (v/v), samples were dried with a Speed-vac, reconstituted under agitation for 15 min in 11 µL of 2%ACN-1%FA and loaded into a 75 µm i.d. × 150 mm, Self-Pack C18 column, installed in the Easy-nLC II system (Proxeon Biosystems). Peptides were loaded on-column and eluted with a two-slope gradient at a flow rate of 250 nL/min. Solvent B first increased from 1 to 32% in 86 min and then from 32 to 82% B in 22 min. The HPLC system was coupled to Orbitrap Fusion mass spectrometer (Thermo Scientific) through a Nanospray Flex Ion Source. Nanospray and S-lens voltages were set to 1.3-1.8 kV and 50 V, respectively. Capillary temperature was set to 250 °C. Full scan MS survey spectra (m/z 320-1520) in profile mode were acquired in the Orbitrap with a resolution of 120,000 with a target value at 5e5. The most intense peptide ions were fragmented by ETD, CID and ETciD and analysed in the linear ion trap with a target value at 1e4. The peptide ion fragmentation parameters were as follow: a reaction time of 120 ms, a reagent target of 2.0e5 and a maximum reagent injection time of 200 ms for ETD, a normalized collision energy of 32% for CID,

calibrated charge dependent ETD parameters and normalized supplemental activation at 18% for ETciD. The duty cycle was set to 4 seconds and target ions selected for fragmentation were dynamically excluded for 30 sec after 2 MS/MS scan events. Uncarboxylated bacterially produced His-tagged ERGP was digested in-solution with chymotrypsin in the aforementioned conditions.

The peak list files were generated with Proteome Discoverer (version 2.1 or 2.4) using the following parameters: minimum mass set to 500 Da, maximum mass set to 6000 Da, no grouping of MS/MS spectra, precursor charge set to auto, and the minimum number of fragment ions set to 5. Protein database searching was performed with Mascot 2.6 (Matrix Science) against a user-defined mouse ERGP database. The mass tolerances for precursor and fragment ions were set to 10 ppm and 0.6 Da, respectively. A semi-specific search was performed using chymotrypsin as the enzyme allowing for up to 1 missed cleavage. Methionine oxidation and carboxylation of glutamic acid were specified as variable modifications. Data interpretation was performed using Scaffold (version 4.8).

Quantification and statistical analysis

All the statistical details of experiments can be found in the figure legends. Statistical analyses were performed using GraphPad Prism software (version 9.3.1). Results are given as means ± SEM. For single measurement, unpaired, 2-tailed Student's *t* test was used. Grouped analysis was performed using one-way ANOVA, followed by Bonferroni's multiple comparisons test. For repeated measurements (metabolic tests), two-way ANOVA followed by Bonferroni's post tests were used. Linear correlations were analyzed using Pearson's correlation. In all figures,

*$P < 0.05$; **$P < 0.01$; ***$P < 0.001$. All experiments were repeated at least 3 times or performed on at least 3 independent animals.

Table S2, related to Figure 2: Gene expression in *Ggcx^{ff}; Pdx1-Cre* and *Ggcx^{ff}* islets analyzed by bulk RNA-sequencing. List of significantly up- (*Up in GGCX KO tab*) and down-regulated (*Down in GGCX KO tab*) genes with a false discovery rate (FDR) ≤ 0.05.

Table S6, related to Figure 5: List of peptides for mouse ERGP identified by LC-MS/MS. The first tab (*Carboxy peptides*) lists all the peptides containing carboxylated glutamic acid residues and their manually measured intensity in the ERGP + VK_1 sample. The ratio of intensity of carboxylated over unmodified peptide is also indicated when this was possible. The second tab (*All peptides*) list all the individual peptides identified in the ERGP + VK_1 sample.

Table S7: List of oligonucleotides used in this study.

REFERENCES

1. Hudish, L.I., J.E. Reusch, and L. Sussel, *beta Cell dysfunction during progression of metabolic syndrome to type 2 diabetes.* J Clin Invest, 2019. **129**(10): p. 4001-4008.
2. Mehran, A.E., et al., *Hyperinsulinemia drives diet-induced obesity independently of brain insulin production.* Cell Metab, 2012. **16**(6): p. 723-37.
3. Mittendorfer, B., et al., *beta Cell function and plasma insulin clearance in people with obesity and different glycemic status.* J Clin Invest, 2022. **132**(3).

4. Solis-Herrera, C., et al., *Pathogenesis of Type 2 Diabetes Mellitus*, in *Endotext*, K.R. Feingold, et al., Editors. 2000, MDText.com: South Dartmouth (MA).

5. Srour, B., et al., *Ultraprocessed Food Consumption and Risk of Type 2 Diabetes Among Participants of the NutriNet-Sante Prospective Cohort.* JAMA Intern Med, 2020. **180**(2): p. 283-291.

6. Kaidar-Person, O., et al., *Nutritional deficiencies in morbidly obese patients: a new form of malnutrition? Part A: vitamins.* Obes Surg, 2008. **18**(7): p. 870-6.

7. Hoffman, D.J., et al., *Developmental origins of metabolic diseases.* Physiol Rev, 2021. **101**(3): p. 739-795.

8. Via, M., *The malnutrition of obesity: micronutrient deficiencies that promote diabetes.* ISRN Endocrinol, 2012. **2012**: p. 103472.

9. Lacombe, J. and M. Ferron, *VKORC1L1, An Enzyme Mediating the Effect of Vitamin K in Liver and Extrahepatic Tissues.* Nutrients, 2018. **10**(8): p. E970.

10. Murshed, M., et al., *Extracellular matrix mineralization is regulated locally; different roles of two gla-containing proteins.* J Cell Biol, 2004. **165**(5): p. 625-30.

11. Furie, B., B.A. Bouchard, and B.C. Furie, *Vitamin K-dependent biosynthesis of gamma-carboxyglutamic acid.* Blood, 1999. **93**(6): p. 1798-808.

12. Lee, N.K., et al., *Endocrine regulation of energy metabolism by the skeleton.* Cell, 2007. **130**(3): p. 456-69.

13. Ferron, M., et al., *GGCX and VKORC1 inhibit osteocalcin endocrine functions.* J Cell Biol, 2015. **208**(6): p. 761-76.

14. Pan, Y. and R.T. Jackson, *Dietary phylloquinone intakes and metabolic syndrome in US young adults.* J Am Coll Nutr, 2009. **28**(4): p. 369-79.

15. Beulens, J.W., et al., *Dietary phylloquinone and menaquinones intakes and risk of type 2 diabetes.* Diabetes Care, 2010. **33**(8): p. 1699-705.

16. Ibarrola-Jurado, N., et al., *Dietary phylloquinone intake and risk of type 2 diabetes in elderly subjects at high risk of cardiovascular disease.* Am J Clin Nutr, 2012. **96**(5): p. 1113-8.

17. Ewang-Emukowhate, M., et al., *Vitamin K and other markers of micronutrient status in morbidly obese patients before bariatric surgery.* Int J Clin Pract, 2015. **69**(6): p. 638-42.

18. Dihingia, A., et al., *Vitamin K1 inversely correlates with glycemia and insulin resistance in patients with type 2 diabetes (T2D) and positively regulates SIRT1/AMPK pathway of glucose metabolism in liver of T2D mice and hepatocytes cultured in high glucose.* J Nutr Biochem, 2018. **52**: p. 103-114.

19. Zwakenberg, S.R., et al., *Circulating Phylloquinone Concentrations and Risk of Type 2 Diabetes: A Mendelian Randomization Study.* Diabetes, 2019. **68**(1): p. 220-225.

20. Karamzad, N., et al., *Effects of MK-7 Supplementation on Glycemic Status, Anthropometric Indices and Lipid Profile in Patients with Type 2 Diabetes: A Randomized Controlled Trial.* Diabetes Metab Syndr Obes, 2020. **13**: p. 2239-2249.

21. Rahimi Sakak, F., et al., *Glycemic control improvement in individuals with type 2 diabetes with vitamin K2 supplementation: a randomized controlled trial.* Eur J Nutr, 2021. **60**(5): p. 2495-2506.

22. Schmidt, T., et al., *ProteomicsDB.* Nucleic Acids Res, 2018. **46**(D1): p. D1271-D1281.

23. TabulaMurisConsortium, *Single-cell transcriptomics of 20 mouse organs creates a Tabula Muris.* Nature, 2018. **562**(7727): p. 367-372.

24. DiGruccio, M.R., et al., *Comprehensive alpha, beta and delta cell transcriptomes reveal that ghrelin selectively activates delta cells and promotes somatostatin release from pancreatic islets.* Mol Metab, 2016. **5**(7): p. 449-458.

25. Berkner, K.L. and B.N. Pudota, *Vitamin K-dependent carboxylation of the carboxylase.* Proc Natl Acad Sci U S A, 1998. **95**(2): p. 466-71.

26. Lacombe, J., et al., *VKOR paralog VKORC1L1 supports vitamin K-dependent protein carboxylation in vivo.* JCI Insight, 2018. **3**(1): p. e96501.

27. Haque, J.A., et al., *A cellular system for quantitation of vitamin K cycle activity: structure-activity effects on vitamin K antagonism by warfarin metabolites.* Blood, 2014. **123**(4): p. 582-9.

28. Shen, G., et al., *Warfarin traps human vitamin K epoxide reductase in an intermediate state during electron transfer.* Nat Struct Mol Biol, 2017. **24**(1): p. 69-76.

29. Sharma, R.B., H.V. Landa-Galvan, and L.C. Alonso, *Living Dangerously: Protective and Harmful ER Stress Responses in Pancreatic beta-Cells.* Diabetes, 2021. **70**(11): p. 2431-2443.

30. Johnson, J.S., et al., *Pancreatic and duodenal homeobox protein 1 (Pdx-1) maintains endoplasmic reticulum calcium levels through transcriptional regulation of sarco-endoplasmic reticulum calcium ATPase 2b (SERCA2b) in the islet beta cell.* J Biol Chem, 2014. **289**(47): p. 32798-810.

31. Wang, I.M., et al., *Systems analysis of eleven rodent disease models reveals an inflammatome signature and key drivers.* Mol Syst Biol, 2012. **8**: p. 594.

32. Motterle, A., et al., *Identification of islet-enriched long non-coding RNAs contributing to beta-cell failure in type 2 diabetes.* Mol Metab, 2017. **6**(11): p. 1407-1418.

33. Lee, H., et al., *Beta Cell Dedifferentiation Induced by IRE1alpha Deletion Prevents Type 1 Diabetes.* Cell Metab, 2020. **31**(4): p. 822-836 e5.

34. Ferdaoussi, M., et al., *Isocitrate-to-SENP1 signaling amplifies insulin secretion and rescues dysfunctional beta cells.* J Clin Invest, 2015. **125**(10): p. 3847-60.

35. Brouwers, B., et al., *Impaired islet function in commonly used transgenic mouse lines due to human growth hormone minigene expression.* Cell Metab, 2014. **20**(6): p. 979-90.

36. Oropeza, D., et al., *Phenotypic Characterization of MIP-CreERT1Lphi Mice With Transgene-Driven Islet Expression of Human Growth Hormone.* Diabetes, 2015. **64**(11): p. 3798-807.

37. Stamateris, R.E., et al., *Adaptive beta-cell proliferation increases early in high-fat feeding in mice, concurrent with metabolic changes, with induction of islet cyclin D2 expression.* Am J Physiol Endocrinol Metab, 2013. **305**(1): p. E149-59.

38. Sharma, R.B., et al., *Insulin demand regulates beta cell number via the unfolded protein response.* J Clin Invest, 2015. **125**(10): p. 3831-46.

39. Alquier, T. and V. Poitout, *Considerations and guidelines for mouse metabolic phenotyping in diabetes research.* Diabetologia, 2018. **61**(3): p. 526-538.

40. Weldemariam, M.M., J. Woo, and Q. Zhang, *Pancreatic INS-1 beta-Cell Response to Thapsigargin and Rotenone: A Comparative Proteomics Analysis Uncovers Key Pathways of beta-Cell Dysfunction.* Chem Res Toxicol, 2022. **35**(6): p. 1080-1094.

41. Feriotto, G., et al., *Myocyte enhancer factor 2 activates promoter sequences of the human AbetaH-J-J locus, encoding aspartyl-beta-hydroxylase, junctin, and junctate.* Mol Cell Biol, 2005. **25**(8): p. 3261-75.

42. Dinchuk, J.E., et al., *Aspartyl beta -hydroxylase (Asph) and an evolutionarily conserved isoform of Asph missing the catalytic domain share exons with junctin.* J Biol Chem, 2000. **275**(50): p. 39543-54.

43. Feriotto, G., et al., *Multiple levels of control of the expression of the human A beta H-J-J locus encoding aspartyl-beta-hydroxylase, junctin, and junctate.* Ann N Y Acad Sci, 2006. **1091**: p. 184-90.

44. Srikanth, S., et al., *Junctate is a Ca2+-sensing structural component of Orai1 and stromal interaction molecule 1 (STIM1).* Proc Natl Acad Sci U S A, 2012. **109**(22): p. 8682-7.

45. Lunz, V., C. Romanin, and I. Frischauf, *STIM1 activation of Orai1*. Cell Calcium, 2019. **77**: p. 29-38.

46. Samtleben, S., B. Wachter, and R. Blum, *Store-operated calcium entry compensates fast ER calcium loss in resting hippocampal neurons.* Cell Calcium, 2015. **58**(2): p. 147-59.

47. Palty, R., et al., *SARAF inactivates the store operated calcium entry machinery to prevent excess calcium refilling.* Cell, 2012. **149**(2): p. 425-38.

48. Sabourin, J., et al., *Store-operated Ca2+ Entry Mediated by Orai1 and TRPC1 Participates to Insulin Secretion in Rat beta-Cells.* J Biol Chem, 2015. **290**(51): p. 30530-9.

49. Kono, T., et al., *Impaired Store-Operated Calcium Entry and STIM1 Loss Lead to Reduced Insulin Secretion and Increased Endoplasmic Reticulum Stress in the Diabetic beta-Cell.* Diabetes, 2018. **67**(11): p. 2293-2304.

50. Greotti, E., et al., *Characterization of the ER-Targeted Low Affinity Ca(2+) Probe D4ER.* Sensors (Basel), 2016. **16**(9).

51. Yong, J., et al., *Chop/Ddit3 depletion in beta cells alleviates ER stress and corrects hepatic steatosis in mice.* Sci Transl Med, 2021. **13**(604).

52. Roe, M.W., et al., *Defective glucose-dependent endoplasmic reticulum Ca2+ sequestration in diabetic mouse islets of Langerhans.* J Biol Chem, 1994. **269**(28): p. 18279-82.

53. Liu, X., et al., *Is the Risk of Diabetes Lower in Patients With Atrial Fibrillation Treated With Direct Oral Anticoagulant Compared to Warfarin?* Front Cardiovasc Med, 2022. **9**: p. 874795.

54. Cheung, C.L., et al., *Treatment with direct oral anticoagulants or warfarin and the risk for incident diabetes among patients with atrial fibrillation: a population-based cohort study.* Cardiovasc Diabetol, 2021. **20**(1): p. 71.

55. Schulte, A. and R. Blum, *Shaped by leaky ER: Homeostatic Ca(2+) fluxes.* Front Physiol, 2022. **13**: p. 972104.

56. Mamenko, M., et al., *Defective Store-Operated Calcium Entry Causes Partial Nephrogenic Diabetes Insipidus.* J Am Soc Nephrol, 2016. **27**(7): p. 2035-48.

57. Park, C.Y., et al., *STIM1 clusters and activates CRAC channels via direct binding of a cytosolic domain to Orai1.* Cell, 2009. **136**(5): p. 876-90.

58. Treves, S., et al., *Junctate is a key element in calcium entry induced by activation of InsP3 receptors and/or calcium store depletion.* J Cell Biol, 2004. **166**(4): p. 537-48.

59. Kwon, S.J. and D.H. Kim, *Characterization of junctate-SERCA2a interaction in murine cardiomyocyte.* Biochem Biophys Res Commun, 2009. **390**(4): p. 1389-94.

60. Zhang, I.X., et al., *ER stress increases store-operated Ca(2+) entry (SOCE) and augments basal insulin secretion in pancreatic beta cells.* J Biol Chem, 2020. **295**(17): p. 5685-5700.

61. Sabatini, P.V., T. Speckmann, and F.C. Lynn, *Friend and foe: beta-cell Ca(2+) signaling and the development of diabetes.* Mol Metab, 2019. **21**: p. 1-12.

62. Liang, K., et al., *Alterations of the Ca(2)(+) signaling pathway in pancreatic beta-cells isolated from db/db mice.* Protein Cell, 2014. **5**(10): p. 783-94.

63. Stenflo, J., et al., *Vitamin K dependent modifications of glutamic acid residues in prothrombin.* Proc Natl Acad Sci U S A, 1974. **71**(7): p. 2730-3.

64. Perez-Riverol, Y., et al., *The PRIDE database resources in 2022: a hub for mass spectrometry-based proteomics evidences.* Nucleic Acids Res, 2022. **50**(D1): p. D543-D552.

65. Hingorani, S.R., et al., *Preinvasive and invasive ductal pancreatic cancer and its early detection in the mouse.* Cancer Cell, 2003. **4**(6): p. 437-50.

66. Thorens, B., et al., *Ins1(Cre) knock-in mice for beta cell-specific gene recombination.* Diabetologia, 2015. **58**(3): p. 558-65.

67. Lyon, J., et al., *Research-Focused Isolation of Human Islets From Donors With and Without Diabetes at the Alberta Diabetes Institute IsletCore.* Endocrinology, 2016. **157**(2): p. 560-9.

68. Lyon, J., et al., *ADI IsletCore Protocols for the Isolation, Assessment and Cryopreservation of Human Pancreatic Islets of Langerhans for Research Purposes V.1.* protocol.io, 2019.

69. Ronnebaum, S.M., et al., *Silencing of cytosolic or mitochondrial isoforms of malic enzyme has no effect on glucose-stimulated insulin secretion from rodent islets.* J Biol Chem, 2008. **283**(43): p. 28909-17.

70. Hagman, D.K., et al., *Cyclical and alternating infusions of glucose and intralipid in rats inhibit insulin gene expression and Pdx-1 binding in islets.* Diabetes, 2008. **57**(2): p. 424-31.

71. Moulle, V.S., et al., *Glucose and fatty acids synergistically and reversibly promote beta cell proliferation in rats.* Diabetologia, 2017. **60**(5): p. 879-888.

72. Ghosh, S., et al., *GGCX mutations show different responses to vitamin K thereby determining the severity of the hemorrhagic phenotype in VKCFD1 patients.* J Thromb Haemost, 2021. **19**(6): p. 1412-1424.

73. Tie, J.K., et al., *Functional study of the vitamin K cycle in mammalian cells.* Blood, 2011. **117**(10): p. 2967-74.

74. Lacombe, J., et al., *Measurement of bioactive osteocalcin in humans using a novel immunoassay reveals association with glucose metabolism and beta-cell function.* Am J Physiol Endocrinol Metab, 2020. **318**(3): p. E381-E391.

75. Al Rifai, O., et al., *Proprotein convertase furin regulates osteocalcin and bone endocrine function.* J Clin Invest, 2017. **127**(11): p. 4104-4117.

76. Chomczynski, P. and N. Sacchi, *The single-step method of RNA isolation by acid guanidinium thiocyanate-phenol-chloroform extraction: twenty-something years on.* Nat Protoc, 2006. **1**(2): p. 581-5.

77. Oh-Hora, M., et al., *Dual functions for the endoplasmic reticulum calcium sensors STIM1 and STIM2 in T cell activation and tolerance.* Nat Immunol, 2008. **9**(4): p. 432-43.

78. Schindelin, J., et al., *Fiji: an open-source platform for biological-image analysis.* Nat Methods, 2012. **9**(7): p. 676-82.

79. Ferron, M., et al., *Inositol polyphosphate 4-phosphatase B as a regulator of bone mass in mice and humans.* Cell Metab, 2011. **14**(4): p. 466-77.

80. Picard, M., et al., *Spatial and temporal activation of the small GTPases RhoA and Rac1 by the netrin-1 receptor UNC5a during neurite outgrowth.* Cell Signal, 2009. **21**(12): p. 1961-73.

81. Xia, Z. and Y. Liu, *Reliable and global measurement of fluorescence resonance energy transfer using fluorescence microscopes.* Biophys J, 2001. **81**(4): p. 2395-402.

82. Szklarczyk, D., et al., *The STRING database in 2021: customizable protein-protein networks, and functional characterization of user-uploaded gene/measurement sets.* Nucleic Acids Res, 2021. **49**(D1): p. D605-D612.

83. Bardou, P., et al., *jvenn: an interactive Venn diagram viewer.* BMC Bioinformatics, 2014. **15**(1): p. 293.

viii. <u>Bridging text</u>

The study in chapter 2 detailed the discovery of the role of vitamin K-dependent carboxylation in the functioning of beta cells. Mice specifically lacking GGCX in their beta cells (*Ggcx^{ff};Ins1-Cre*) were found to have fasting hyperinsulinemia and hyperglycemia when placed on a high fat diet for one week. In parallel, ERGP was identified as a novel gamma-carboxylated protein expressed in the beta cells. When carboxylated, ERGP was found to reduce the basal cytosolic calcium, ER calcium efflux, and store-operated calcium entry (SOCE). Strikingly, semi-dispersed islet cells taken from *Ggcx^{ff};Ins1-Cre* mice were found to also have elevated basal cytosolic calcium, ER calcium efflux, and SOCE. Therefore, we proposed that *Ggcx^{ff};Ins1-Cre* mice lacking functional carboxylated ERGP in their beta cells had chronically elevated SOCE, leading to calcium overfilling and hyperinsulinemia.

The effect of ERGP knockout or knockdown was not examined in this study and so the role of ERGP in beta cell calcium overfilling or high fat diet induced hyperinsuliemia was not directly described. Furthermore, the study detailed in chapter 2 examined beta cell calcium dynamics only in the context of semi dispersed islets. Whole islets are known to have coordinated calcium oscillations and the role of gamma-carboxylation in these oscillations remained unknown. Finally, the molecular mechanism by which ERGP regulates SOCE remained uncharacterized. By identifying the interactors of ERGP, we could gain insight into the molecular mechanism by which ERGP regulates beta cell calcium flux and ultimately insulin secretion. In the study presented in chapter 3, we sought to 1) examine the effect of ERGP knockdown on SOCE in beta cells, glucose tolerance, and glucoses stimulated insulin secretion, 2) determine the role of beta cell gamma-carboxylation in whole islet calcium oscillations, and 3) identify potential interactors of ERGP.

Chapter 3: Second manuscript

Endoplamic Reticulum Gla Protein (ERGP) is a novel vitamin K-dependent protein regulating beta cell coordination and ER Ca^{2+} homeostasis

Kevin Guo[1,2], Giada Ostinelli[3], Julie Lacombe[1], Laura Quirion[1], Denis Faubert[1], Jean-Francois Côté[1,4], Guy A. Rutter[3,4,5,6] and Mathieu Ferron[1,2,4]

[1] Institut de recherches cliniques de Montréal, Montréal, Canada

[2] Division of Experimental Medicine, McGill University, Montréal, Canada

[3] Centre de Recherche du Centre Hospitalier de l'Université de Montréal, Montréal, Canada

[4] Department of Medicine, Université de Montréal, Montréal, Canada

[5]Faculty of Medicine, Imperial College London, London, U.K.

[6]LKC School of Medicine, Nanyang Technological College, Singapore

Corresponding author:

Mathieu Ferron, PhD

Institut de Recherches Cliniques de Montréal

110 Ave. des Pins O.

Montréal, QC,

H2W 1R7, Canada

Phone: 514-987-5754

Email: mathieu.ferron@ircm.qc.ca

SUMMARY

Islets from individuals with type 2 diabetes (T2D) have disrupted insulin secretion linked to a breakdown of coordinated islet Ca2+ oscillations. Endoplasmic Reticulum Gla Protein (ERGP) which is gamma-carboxylated by GGCX, has been identified as a potential regulator of beta-cell Ca2+ flux through its role in the suppression of store-operated Ca2+ entry (SOCE). Consequently, ERGP may play a role in the regulation of calcium oscillations throughout the whole islet. In this study, we show that beta-cells with ERGP knocked down (*AsphLacZ/LacZ*) have elevated SOCE and glucose stimulated Ca2+ flux and that islets lacking functional ERGP (*Ggcxff;Ins1-Cre*) have increased period of Ca2+ oscillation and reduced islet cell coactivity. TurboID-based proximity labeling identified the IP3 receptors (ITPR1-3), which are involved in ER Ca2+ efflux, and the SOCE complex proteins STIM1 and STIM2 as interactors of ERGP. Strikingly, STIM1 and STIM2 interaction is increased following ER Ca2+ depletion by thapsigargin while ITPR1 interaction is decreased. We propose that ERGP potentially regulates beta-cell Ca2+ flux via interactions with ER Ca2+ regulators to impacts beta cell connectivity.

INTRODUCTION

Recent evidence has revealed that beta cell failure is necessary for the development of type 2 diabetes (T2D), a metabolic disorder characterized by peripheral insulin resistance and insufficient secretion of insulin [35]. In healthy individuals, insulin is secreted in a pulsatile manner. Disruption of this pulsatile secretion pattern is associated with peripheral insulin resistance and is characteristic of patients with T2D [102, 183]. Exquisite coordination of the metabo- Ca^{2+} oscillation of individual beta-cells is necessary to produce these insulin pulses. This is made evident by the coordinated Ca^{2+} waves which propagate across healthy islets following glucose stimulation [113, 184, 185]. This coordination is made possible through cell-cell communication, via signaling pathways like Slit-Robo [186], and the exchange of ions and other molecules via connexin-36 gap junctions [101, 112, 187]. Such connections are not homogenous, however, as there is increasing evidence for heterogeneity of beta cell function within islets; including, in their role in coordinating whole islet Ca^{2+} oscillation [97, 114, 188]. For instance, a subset of beta cells known as hub cells has been identified to be more highly connected and essential for the coordination of whole islet Ca^{2+} oscillation [111].

Disruption of beta cell endoplasmic reticulum (ER) Ca^{2+} replenishment through store-operated Ca^{2+} entry (SOCE) has also been shown to disrupt whole islet Ca^{2+} oscillation and insulin secretion [142]. Recently, we identified ER Gla protein (ERGP) as a novel regulator of SOCE. ERGP is an ER resident protein encoded by the *ASPH* gene locus which suppresses SOCE and prevents beta cell Ca^{2+} overfilling. ERGP function depends on its carboxylation by the gamma-carboxylase (GGCX) [189]. GGCX uses reduced vitamin K as a co-factor to add an additional

carboxylic acid group onto specific glutamic acid (Glu) residues converting them into gamma-carboxyglutamic (Gla) acid residues in a process called gamma-carboxylation [51].

Semi-dispersed islet cells taken from mice lacking GGCX and hence functional gamma-carboxylated ERGP were characterized by elevated basal cytosolic Ca^{2+} levels, ER Ca^{2+} levels, and SOCE following ER Ca^{2+} depletion. Mice lacking GGCX displayed elevated fasting insulin and peripheral insulin resistance following a one-week high fat diet owing to beta-cell Ca^{2+} overfilling [189]. Despite having established gamma-carboxylation role in beta cell Ca^{2+} regulation and ERGP as a regulator of SOCE in HEK293, direct genetic evidence that ERGP regulates SOCE in beta cell is still lacking. Moreover, the molecular mechanism by which ERGP inhibits SOCE and regulates ER Ca^{2+} levels remain unknown. Finally, the potential impact of gamma-carboxylation on whole islet Ca^{2+} oscillations is also unexplored. We aimed here at addressing these three unanswered questions.

Using a mouse line with ERGP expression knocked down, we demonstrated the direct role of ERGP in negatively regulating SOCE and preventing beta cell Ca^{2+} overfilling. We also explored the whole islet Ca^{2+} oscillation dynamics of islets lacking GGCX and hence functional ERGP and found they had an increased period of oscillation as well as decreased islet cell coactivity and correlation. Next, we identified the interactors of ERGP following ER Ca^{2+} depletion and under basal conditions using TurboID, a molecular tool where the promiscuous biotin ligase mini-Turbo is fused to a protein of interest, resulting in the biotinylation of its interactors [182]. As a result, numerous proteins involved in ER Ca^{2+} homeostasis, the unfolded protein response,

and cell-cell signaling, and transcriptional regulation were identified. We propose that ERGP regulates beta-cell Ca^{2+} flux via its interaction with known regulators of ER Ca^{2+} and may also play a role in beta-cell connectivity as evidenced by its interactions with mediators of cell-cell interactions and impact on whole islet Ca^{2+} oscillations.

RESULTS

Store-operated Ca^{2+} entry (SOCE) and glucose stimulated Ca^{2+} flux is elevated in the beta-cells of ERGP knockdown mice

Vitamin-K (VK) dependent carboxylation of ERGP is required for its role in supressing store-operated Ca^{2+} entry (SOCE) and maintaining lower basal ER and cytosolic Ca^{2+} levels in HEK293 cells [189]. Semi-dispersed islet cells taken from mice specifically lacking GGCX in their beta-cells (*Ggcx^{ff};Ins1-Cre*) in which ERGP is not carboxylated have increased ER Ca^{2+} efflux following the addition of thapsigargin, a SERCA inhibitor, and SOCE. They were also seen to have heightened glucose stimulated Ca^{2+} levels [189].

We sought here to directly examine the effect of ERGP on beta cell SOCE and glucose stimulated Ca^{2+} flux. We generated a gene trap allele of *Asph* in mice (*Asph$^{LacZ/LacZ}$*) targeting all products of *Asph* first promoter, which include ASPH and ERGP (Figure 1A) [180]. ASPH and ERGP expression assessed by immunofluorescence was reduced in beta cell of *Asph$^{LacZ/LacZ}$* mice (Figure 1B). The expression of the mRNA encoding ASPH and ERGP were reduced 80-90% in isolated islets (Figure 1C). However, protein levels of both ASPH and ERGP remained at around 40% of the wild-type (WT) levels (Figure 1D and E). This may be due to a partial rescue of ASPH and ERGP expression from the second promoter through skipping of the gene trapped

exon and transcriptional reinitiation [190]. Therefore, *Asph*$^{LacZ/LacZ}$ represent an hypomorphic allele of ERGP and ASPH in beta cell.

Islets isolated from WT and *Asph*$^{LacZ/LacZ}$ mice were semi-dispersed and loaded with the Ca^{2+} sensitive fluorescent dye Fluo-4 for Ca^{2+} imaging. Following imaging, the cells were immunostained for insulin to identify beta cell clusters. To assess glucose stimulated Ca^{2+} flux, cells were stimulated with 15mM glucose following baseline measurements at 5mM glucose. Maximum Ca^{2+} influx potential was then assessed by depolarizing the cells with 30mM KCl (Figure 1F). Beta cell clusters from *Asph*$^{LacZ/LacZ}$ mice had heightened glucose stimulated Ca^{2+} flux (Figure 1G and H) and maximum Ca^{2+} influx (Figure 1G and I) compared to WT. The SOCE capacity of the semi-dispersed beta cell clusters was next measured using the Ca^{2+} addback protocol (Figure 1J) [152, 159, 164]. Beta cell clusters from *Asph*$^{LacZ/LacZ}$ mice had a tendency, though not significant, for increased thapsigargin induced ER Ca^{2+} depletion (Figure 1K and L) and had increased SOCE (Figure 1K and M) compared to WT.

These results partially recapitulate the Ca^{2+} overfilling phenotype previously reported in the islet clusters from the *Ggcx*^{ff}*;Ins1-Cre* mice [189], suggesting that ERGP is the main carboxylated protein responsible for suppressing SOCE and preventing the Ca^{2+} overfilling in beta cells.

ERGP knockdown is insufficient to cause high fat diet (HFD) induced fasting hyperinsulinemia or insulin resistance

We previously reported that *Ggcx*^{ff}*;Ins1-Cre* mice displayed fasting hyperinsulinemia and peripheral insulin resistance after being fed a high fat diet (HFD) for 1 week [189]. When fed a HFD, *Asph*$^{LacZ/LacZ}$ mice did not display differences in weight gain over the course of 8 weeks

(Figure 2A) when compared to WT. Neither did these mice have differences in glucose tolerance (Figure 2B) or fasting glucose levels (Figure 2C) after 1 week on a HFD. However, *Asph*$^{LacZ/LacZ}$ mice displayed significantly elevated fasting insulin (Figure 2D) after 1 week on a HFD, but did not have significantly different glucose stimulated insulin secretion (GSIS) when compared to WT mice (Figure 2E and F). However, the homeostatic model assessment of insulin resistance (HOMA-IR) was higher in the *Asph*$^{LacZ/LacZ}$ mice after 1 week of HFD, suggesting elevated insulin resistance in these mice (Figure 2G).

After extending the HFD to 4 weeks, the *Asph*$^{LacZ/LacZ}$ mice did not have a difference in fasting glucose or insulin (Figure 2H and I). Even following 8 weeks on a HFD, there was no difference in the fasting glucose or glucose tolerance of the *Asph*$^{LacZ/LacZ}$ mice compared with WT mice (Figure 2J and K). While the beginnings of a metabolic defect seem to be present after 1 week on HFD, the *Asph*$^{LacZ/LacZ}$ mice seem able to compensate for this defect and display no differences in glucose or insulin homeostasis beyond 4 weeks on a HFD.

Beta cell specific knockout of GGCX increases the period of whole islet Ca^{2+} oscillations

Semi-dispersed islets taken from both ERGP knockdown *Asph*$^{LacZ/LacZ}$ mice and carboxylation insufficient *Ggcx*^{ff}*;Ins1-Cre* mice have elevated SOCE, suggesting that functional carboxylated ERGP is essential for regulating SOCE in beta cells. Disruption of SOCE in beta cells has previously been shown to alter whole islet Ca^{2+} oscillation and reduce glucose stimulated insulin secretion [142]. Disruption of coordinated islet Ca^{2+} oscillation is also an early indicator for the development of T2D [183]. Therefore, we hypothesized that beta cell Ca^{2+} overfilling in the absence of functional ERGP may disrupt islet Ca^{2+} oscillations.

To determine the role of carboxylated ERGP in whole islet Ca^{2+} oscillations, islets isolated from *Ggcx^{ff};Ins1-Cre* or control *Ins1-Cre* mice were loaded with the fluorescent Ca^{2+} dye Cal-520 and imaged at 11mM glucose (Figure 3A). Islets that did not display oscillatory activity were excluded from the analysis and amounted to less than 5% of islets from either condition. The majority of islets from both the control *Ins1-Cre* as well as the *Ggcx^{ff};Ins1-Cre* mice displayed "slow" type oscillation, with fewer than 15 peaks recorded throughout the 30 minute recording period. Despite this, islets from the *Ggcx^{ff};Ins1-Cre* mice had significantly more peaks recorded on average ($p<0.0001$) (Figure 3B). As a result, the period of oscillation was higher in the islets taken from the *Ggcx^{ff};Ins1-Cre* mice (Figure 3C). There was no significant difference in the amplitude of oscillation between the two conditions (Figure 3D) and no difference in the size of the islets (Figure 3E). These results suggest that a lack of carboxylated ERGP alters whole islet Ca^{2+} dynamics.

Beta cell specific knockout of GGCX reduces islet connectivity and coactivity

Islets taken from *Ggcx^{ff};Ins1-Cre* mice had an increased period of Ca^{2+} oscillation, suggesting a disruption of the Ca^{2+} imaging dynamics between islet cells. To further dissect this, we examined the Ca^{2+} oscillation of individual cells within selected islets taken from *Ggcx^{ff};Ins1-Cre* and *Ins1-Cre* mice. Twenty-five islets with whole islet oscillatory periods closest to the mean (Figure 3C) were subjected to single islet cell analysis. This revealed an apparent loss of Ca^{2+} oscillatory coordination of the cells within the islets from *Ggcx^{ff};Ins1-Cre* mice (Figure 4A). To quantify this difference, islet cell coactivity was assessed by first binarizing the Ca^{2+} oscillation signal of each cell into "on" or "off states, defined as being more than 25% above the moving baseline or less than 25% above the baseline respectively. The proportion of time that each cell spent in the

same state (“on” or “off”) as another cell, corrected for coactivity by chance, was then used to define coactivity. Cells which had greater than 20% of its connections with a coactivity value >0.9 were defined as “highly connected cells” (Figure 4B).

This analysis demonstrates that islet cells from *Ggcx^{ff};Ins1-Cre* mice spend a lower percentage of time in the “on” state when compared to islet cells from control *Ins1-Cre* mice (Figure 4C). A significantly higher proportion of cells in the islets of *Ggcx^{ff};Ins1-Cre* mice were inactive, meaning their amplitude of oscillation never increased more than 25% above the baseline throughout the duration of the recording (Figure 4D). Finally, the average coactivity between cells of *Ggcx^{ff};Ins1-Cre* islets was lower compared to the *Ins1-Cre* control (Figure 4E), and their activity was less correlated with other cells within the same islet when compared to the control (Figure 4F). Together these analyses indicate that coordinated islets Ca2+ oscillations are disrupted in absence of γ-carboxylation in beta cell.

Establishment of a proximity-dependent biotinylation assay to identify ERGP partners

To better understand the potential mechanism by which ERGP elicits its functions, potential ERGP interactors were identified using a protein-proximity labelling assay. In this method, miniTurbo, a promiscuous version of the biotin ligase BirA, is fused to a protein of interest, in this case ERGP, resulting in the biotinylation of proteins that come into close proximity with the fusion protein. miniTurbo was chosen to be the promiscuous biotin ligase due to its ability to robustly biotinylate interacting proteins even following a short biotin labeling period of 10-30 minutes [182]. This allowed us to identify differences in ERGP protein interactors with or without a 15-minute thapsigargin treatment, which trigers ER Ca^{2+} depletion and activates SOCE.

To identify potential interactors from both the cytosol and ER lumen, fusion proteins with miniTurbo fused to the N-terminal cytosolic side (mT-ERGP) or the C-terminal ER lumen side of ERGP (ERGP-mT) were generated. To exclude non-specific candidates, a similar set of fusion proteins was generated with miniTurbo and CD74, a regulator of MHC class II (mT-CD74 and CD74-mT). CD74, like ERGP, is an ER resident type 2 transmembrane protein of a similar size to ERGP but lacking any sequence homology (Figure 5A). Immunofluorescent staining of HEK293 cells expressing mT-ERGP, ERGP-mT, mT-CD74, or CD74-mT showed that all four miniTurbo fusion constructs were expressed in the ER via costaining with an anti-KDEL antibody (Figure 5B).

ERGP is physiologically active in its carboxylated form and has been shown to regulate SOCE in HEK293 cells [189]. For this reason, the TurboID screen was performed in HEK293 cells cultured with VK and overexpressing the VK cycle proteins GGCX and VKORC1, which are necessary for VK-dependent carboxylation of ERGP [51]. All four miniTurbo fusion proteins were able to robustly biotinylate interactors following a 15-minute biotin pulse (Figure 5C). The presence of VK did not affect the biotinylation pattern for either the ERGP or CD74 miniTurbo fusion proteins. Biotinylation also did not affect the carboxylation of the mT-ERGP or ERGP-mT. Interestingly, the addition of thapsigargin to cells expressing the ER fused ERGP-mT and CD74-mT constructs resulted in the appearance of several new biotinylated interactors, suggesting that ER Ca^{2+} depletion and subsequent SOCE activation may change the ERGP interactome in specific and non-specific ways (Figure 5C).

To confirm that mT-ERGP and ERGP-mT retained ERGP's function suppressing SOCE in a VK-dependent manner, HEK293 cells lacking ERGP expression were transfected with either mT-ERGP or ERGP-mT in the presence or absence of VK then subjected to SOCE measurement via

Ca^{2+} imaging. This showed that both mT-ERGP and ERGP-mT significantly decreased basal cytosolic Ca^{2+}, thapsigargin induced ER Ca^{2+} depletion, and SOCE in the presence of VK when compared to the non-carboxylated control without VK (Figure 5D-K). These results demonstrate that the miniTurbo-ERGP fusion proteins are functional and can biotinylate protein interactors in the presence or absence of VK and thapsigargin.

ER Ca^{2+} depletion alters both the cytosolic and ER lumen interactome of ERGP

Characterization of ERGP's interactome was next achieved by generating HEK293-Flp TRex cell lines inducibly expressing one of the four miniTurbo fusion constructs. This guaranteed the presence of only one gene copy of the fusion construct, reducing the interactor to fusion protein ratio. These cells were first transfected with GGCX and VKORC1 and cultured with VK before having the miniTurbo fusion protein expression induced with tetracyclin. Following this, either biotin with thapsigargin or only biotin was added to the cells for 15 minutes to allow the biotinylation of interactors. Finally, the cells were lysed and the biotinylated proteins pulled down with streptavidin coated beads before being identified with liquid chromatography with tandem mass spectrometry (LC-MS/MS). The proximity interactome of ERGP was determined by performing Significance Analysis of INTeractome (SAINT) against condition matched CD74 screens. For example, interactors identified in the ERGP-mT with thapsigargin condition underwent SAINT analysis with the CD74-mT with thapsigargin condition as its control. Interactors were deemed significant if SAINT analysis produced a Bayesian false discovery rate of less than 0.0001, an average probability greater than 0.95, if the interactor was detected in the ERGP condition of every experimental replicate, and if the average detection intensity was at least two times greater in the ERGP condition when compared to the CD74 condition (Figure

6A). In total, 735 proximity interaction were identified for mT-ERGP without thapsigargin, 736 for mT-ERGP with thapsigargin, 438 for ERGP-mT without thapsigargin, and 297 for ERGP-mT with thapsigargin (Figure 6B).

SAINT analysis comparing the ERGP conditions with or without thapsigargin was also performed to identify proximal interactions that are increased or decreased by thapsigargin (Figure 6C-F). 83 proteins were seen to significantly interact with mT-ERGP without thapsigargin and have significantly reduced interaction with mT-ERGP in the presence of thapsigargin as determined by SAINT analysis. Among the top 10 interactions with mT-ERGP most decreased by thapsigargin, 4 are involved in vesicular trafficking between intracellular compartments (RAB14, CSE1L, SAR1B) [191-193]. In addition to these, several proteins involved in autophagy also have significantly less interaction with mT-ERGP in the presence of thapsigargin (TMEM208, ATG2B) [194, 195] (Figure 6C). 77 proteins are significant interactors of mT-ERGP with thapsigargin and are seen to have significantly more interaction with mT-ERGP in the presence of thapsigargin. Interestingly, one of the top 10 interactions most increased by thapsigargin is MRPS16, a mitochondrial ribosome subunit [196]. A notable cluster of proteins identified to have increased interaction with mT-ERGP in the presence of thapsigargin is the eukaryotic translation initiation factor proteins (EIF4H, EIF3L, EIF3J) [197-199], suggesting ERGP may have a role in transcriptional regulation following ER Ca^{2+} depletion (Figure 6D). Despite having less significant interactors identified in total compared to the cytosolically fused mT-ERGP condition, the ER fused ERGP-mT without thapsigargin condition identified 101 ERGP interactions decreased by thapsigargin treatment. This suggests that ER Ca^{2+} depletion has a greater impact on ERGP interactors in the ER lumen. RAB14 was again identified as a protein whose interaction with ERGP-mT was significantly decreased by thapsigargin. Importantly, IP_3

receptor 1 (ITPR1), a main cellular mediator of ER Ca^{2+} efflux [152], was found to have significantly decreased ERGP-mT interaction in the presence of thapsigargin (Figure 6E). 26 significant interactors of ERGP-mT were identified to have increased interaction with thapsigargin. Despite this relatively smaller number, many of the interactors are directly implicated in the known functions of ERGP; such as, the SOCE complex proteins STIM1 and STIM2 [152]. In addition, ASPH, the full-length enzymatically active isoform of ERGP [180] was found to have increased interaction with ERGP-mT in the presence of thapsigargin (Figure 6F).

This screen revealed proximal interactions between ERGP and regulators of SOCE and ER Ca^{2+} in a thapsigargin dependent manner. In addition, it suggests that ERGP may play a role in cellular trafficking, autophagy, and mitochondrial function.

ERGP may connect ER Ca^{2+} regulation with the unfolded protein response and transcriptional regulation

Proximal interactions identified both the cytosolic mT-ERGP screen and ER luminal ERGP-mT miniTurbo screen can be considered “high confidence” interactors due to their appearance in several TurboID screens with differing conditions. However, due to the fact that these proteins need to be able to be biotinylated via exposed lysine residues from both the cytosolic and ER luminal sides to be identified in both the mT-ERGP and ERGP-mT screens, they are limited to ER transmembrane proteins with sufficient amino acid exposure in both compartments. In all, 91 proteins were shown by SAINT analysis to be significant interactors of ERGP in at least one of

the mT-ERGP TurboID screens and one of the ERGP-mT TurboID screens. Of these 30 were shown to be significant interactors in every screen (Figure 5B and 6A).

IP_3 receptor 1, 2, and 3 (ITPR1, 2, and 3) are among these 30, further providing evidence for a role of ERGP in the regulation of ER Ca^{2+}. ERGP may also play a role in regulating the unfolded protein response (UPR) as seen by the fact that ATF6B [200], MBTPS1 (SKI-1) [201], and CREB3L2 [202] are also among these 30 proteins. These proteins also include the SUN-domain containing proteins SUN1, SUN2, and SUCO. SUN1 and 2 are components of the LINC (LInker of Nucleoskeleton and Cytoskeleton) complex, involved in the connection between the nuclear lamina and the cytoskeleton [203, 204], while the function of SUCO has not yet been characterized. In addition to these, the nuclear envelope proteins LMNB2 [205] and LEMB3 [206] were also identified in every screen, further providing evidence for potential transcriptional regulatory roles of ERGP (Figure 6A).

Excluding the 30 interactors found in every condition, 38 proteins were found to be significant interactors of both mT-ERGP and ERGP-mT in the absence of thapsigargin. These proteins include ITPR1, LMNB2, and LEMD3. They also include the Notch signaling proteins ADAM17, NOTCH2, and JAG2 [207] as well as ASPH, which hydroxylates both NOTCH2 and JAG2 [180]. Interestingly, ERGP-mT interaction with NOTCH2 and ASPH is increased in the presence of thapsigargin. However, NOTCH2 and ASPH are not seen as significant interactors of mT-ERGP in the presence of thapsigargin. This suggests that NOTCH2 and ASPH may interact with ERGP on different parts of the protein based on the ER Ca^{2+} concentration. ER membrane complex (EMC) proteins EMC4, 8, and 10, which are involved in protein translocation through the ER membrane, were also significant interactors of both mT-ERGP and ERGP-mT in the absence of thapsigargin [208] (Figure 6B). This may be caused by a disruption of ERGP

insertion into the ER membrane when ER Ca^{2+} is depleted, suggesting that ERGP folding may be ER Ca^{2+} concentration dependent. Alternatively, ERGP may be a regulator of the EMC complex. Relatively few proteins were found to be significant interactors of both mT-ERGP and ERGP-mT only following thapsigargin treatment with 18 proteins fitting this definition. Of these, is the UPR protein CREB3L2 (Figure 6C).

The beta-cell expression of this list of 30, 38, and 18 proteins was determined using Tabula Muris, a single cell RNA sequencing (RNAseq) database of various murine tissues including islets [209], to determine the TurboID screen's relevance to islet and beta cell biology. From this, we determined that all proteins for which data was available were expressed in beta cells, with the exception of LEPR (Figure 6D-F).

DISCUSSION

Knockdown of ERGP is sufficient to induce Ca^{2+} overfilling of beta-cells but does not cause fasting hyperinsulinemia after a short high fat diet

In this study, we utilized the *Asph*$^{LacZ/LacZ}$ mouse line which had the expression of all products of *Asph* promoter 1 knocked down. Ca^{2+} imaging of the beta-cells of these mice showed elevated basal cytosolic Ca^{2+}, SOCE, glucose stimulated Ca^{2+} flux, and KCl induced Ca^{2+} flux; much like the beta-cell specific GGCX knockout (*Ggcx*^{ff}*;Ins1-Cre*) previously reported [189]. However, *Asph*$^{LacZ/LacZ}$ mice failed to have significant persistent fasting hyperinsulinema or impaired glucose tolerance even after being placed on a high fat diet for up to 8 weeks. The *Asph*$^{LacZ/LacZ}$ ES cell line was initially procured to create a global knockout of ERGP and ASPH. However, despite significant reduction in mRNA expression, the protein expression of both ERGP and

ASPH remained at around 30% of wild-type levels. Notably, the mice did not display any of the phenotype previously reported for mice lacking ASPH enzymatic activity; such as a foreshortened snout and fusion of the digits [166]. The complicated gene locus of *Asph* likely hinders gene trap attempts as multiple promoters and isoforms may favor skipping of the gene trap containing exon and result in the rescue of protein expression [190].

Regardless, this knockdown was sufficient in producing a Ca^{2+} overfilling phenotype in the beta cells ex vivo. Fasting insulin and HOMA-IR were significantly elevated after one week on a high fat diet, consistent with the metabolic phenotype of *Ggcx^{ff};Ins1-Cre* mice on the same diet [189]. However, no significant difference was seen after the mice continued on a high fat diet for up to 8 weeks. This may have been caused by unknown compensation mechanisms, which allow for the normal functioning of the beta cells even following lowered ERGP expression. It is also possible that beta cell levels of ERGP were not sufficiently reduced In contrast to *Ggcx^{ff};Ins1-Cre* mice, *Asph$^{LacZ/LacZ}$* mice had a global knockdown of ERGP and ASPH. It is possible that such a non-targeted knockdown produced confounding effects that allowed for beta cell compensation against the metabolic stress induced by the high fat diet. A beta cell specific knockout of ERGP could serve to more thoroughly investigate the role of ERGP in protecting against high fat diet induced fasting hyperinsulinemia.

Islets of *Ggcx^{ff};Ins1-Cre* mice have altered Ca^{2+} oscillations caused by a loss of islet cell coordination

Ggcx^{ff};Ins1-Cre islets had an increased period of Ca^{2+} oscillation and impaired coordination of islet Ca^{2+} oscillations propagating throughout the islet. Coordinated islet Ca^{2+} oscillations are

known to be necessary for efficient glucose stimulated insulin secretion [111, 183]. A loss of islet Ca^{2+} coordination may underly the impaired stimulation index previously reported in the *Ggcx^{ff};Ins1-Cre* mice [189]. There is evidence that slow-type oscillations represent the Ca^{2+} oscillation pattern of properly functioning islets in vivo [100, 210]. Most islets taken from mice of either genotype had a period of oscillation of greater than 120 seconds, suggesting that the islets were not excessively stressed. Single-cell RNA sequencing of mouse islets has shown that ERGP is expressed in only about 50% of beta cells [209]. Despite this, disruption of ERGP carboxylation in beta cells was sufficient to produce a breakdown of coordinated Ca^{2+} oscillations throughout the islets. ERGP may be essential in beta cells which have specialized roles in coordinating islet Ca^{2+} oscillations; such as, the hub and leader cells [111, 113].

Strikingly, there is an absence of highly connected cells which may be hub cells in the islets from *Ggcx^{ff};Ins1-Cre* mice. This suggests a loss of either the presence of hub cells in the islets from *Ggcx^{ff};Ins1-Cre* mice or a reduction in their connectivity. Previous studies have shown that the disruption of cell-cell communication between beta-cells produced a similar reduced connectivity phenotype. Beta cell specific knockout of Robo1 and Robo2 has been shown to disrupt islet connectivity and decrease the number of hub cells within islets [186]. Interestingly, the Robo ligand SLIT2, which is also a substrate of ASPH, was identified as a significant interactor of ERGP, providing a potential mechanism by which ERGP may regulate islet connectivity. Disruption of the gap junction protein connexin-36 has also been shown to cause a loss of islet Ca^{2+} oscillation connectivity [187]. Connexin-43, a gap junction protein expressed in HEK293 cells, was identified as an interactor of ERGP by SAINT analysis but was not

considered a significant interactor because it was not detected in one of the 3 experimental replicates. Further studies in beta-cells are necessary to confirm the mechanism by which ERGP regulates islet Ca^{2+} oscillation connectivity and hub cells.

ERGP may play roles in ER Ca^{2+} flux, cell-cell signaling, the unfolded protein response, and gene expression

The results of the TurboID screens have further suggested a role for ERGP in regulating ER Ca^{2+} levels through interaction with the SOCE complex proteins STIM1 and STIM2 and the IP_3 receptors ITPR1, ITPR2, and ITPR3, providing a potential mechanism by which ERGP may regulate Ca^{2+} flux and ultimately insulin secretion in beta-cells. STIM and ITPR proteins have functionally opposite roles where one ultimately serves to bring Ca^{2+} back into the ER and the other triggers efflux of Ca^{2+} from the ER, respectively [141, 211]. We have shown that ER Ca^{2+} depletion by thapsigargin regulates ERGP's interaction with the STIM proteins and ITPR1 in opposite ways, where interaction with STIM1 and STIM2 is increased and interaction with ITPR1 is decreased. While previous studies have identified ERGP as a negative regulator of SOCE [189], it is not known how ERGP may regulate IP_3 receptor function. Follow-up studies examining the role of ERGP in IP_3 receptors activity must be conducted to confirm their interaction.

Beyond ER Ca^{2+} flux, the interactors of ERGP include numerous cell-cell signaling proteins; such as proteins involved in Notch and Slit-Robo signaling. Interestingly, many of these proteins contain Ca^{2+v} binding EGF-like domains, which is the substrate of ASPH [170]. Notch signaling has been shown to play an important role in beta cell proliferation and protection against

apoptosis [117, 212]. Notch signaling may even play a role in cellular Ca^{2+} regulation [213]. Communication between beta cells is essential for maintaining coordinated Ca^{2+} oscillations [185, 186, 188, 214]. By being directly involved in beta-cell Ca^{2+} flux as well as cell-cell signaling, ERGP may serve as a master regulator of islet connectivity. The specific role of ERGP in these signaling pathways remains unknown.

ER Ca^{2+} levels are intimately linked with the function of numerous ER chaperones; such as, calnexin and calreticulin [121, 215]. ER Ca^{2+} depletion by thapsigargin is known to cause ER stress by preventing proper protein folding and activating the UPR [216, 217]. ATF6, identified as a highly significant interactor of ERGP, is a master regulator of UPR related gene expression [200, 218]. Interestingly, ERGP was found to interact with numerous proteins found in the outer nuclear membrane; such as, sun-domain containing proteins and the eukaryotic initiation factors. The ER is continuous with the outer nuclear membrane and connected to the outer mitochondrial membrane through the mitochondria associated ER membranes [219, 220], providing avenues for ERGP, an integral ER resident membrane protein, to interact with proteins which may localize to the nucleus and mitochondria. STRING analysis of the significant ERGP interactors yielded few identifiable pathways outside of an enrichment in Ca^{2+} binding EGF-like domains and the SOCE complex proteins following ER Ca^{2+} depletion. This may be due to a lack of characterization of the pathways regulated by ERGP. Notably, the UPR protein CREB3L2 has significantly increased interaction with ERGP following depletion of ER Ca^{2+} by thapsigargin, suggesting that ERGP's role in UPR regulation may be Ca^{2+} dependent. Mechanistically, ERGP may serve fundamentally as an ER Ca^{2+} regulator which is involved in a signaling cascade linking ER Ca^{2+} levels to UPR activation and subsequent transcriptional regulation.

In conclusion, ERGP has been confirmed to be the carboxylated protein regulating SOCE and preventing Ca^{2+} overfilling in beta-cells. This function is required to coordinate islet Ca^{2+} oscillations and maintain beta-cell connectivity, possibly through ERGP's regulation of Slit-Robo signaling. ERGP may also play a role in UPR regulation and transcriptional regulation in a Ca^{2+} dependent manner.

FIGURES

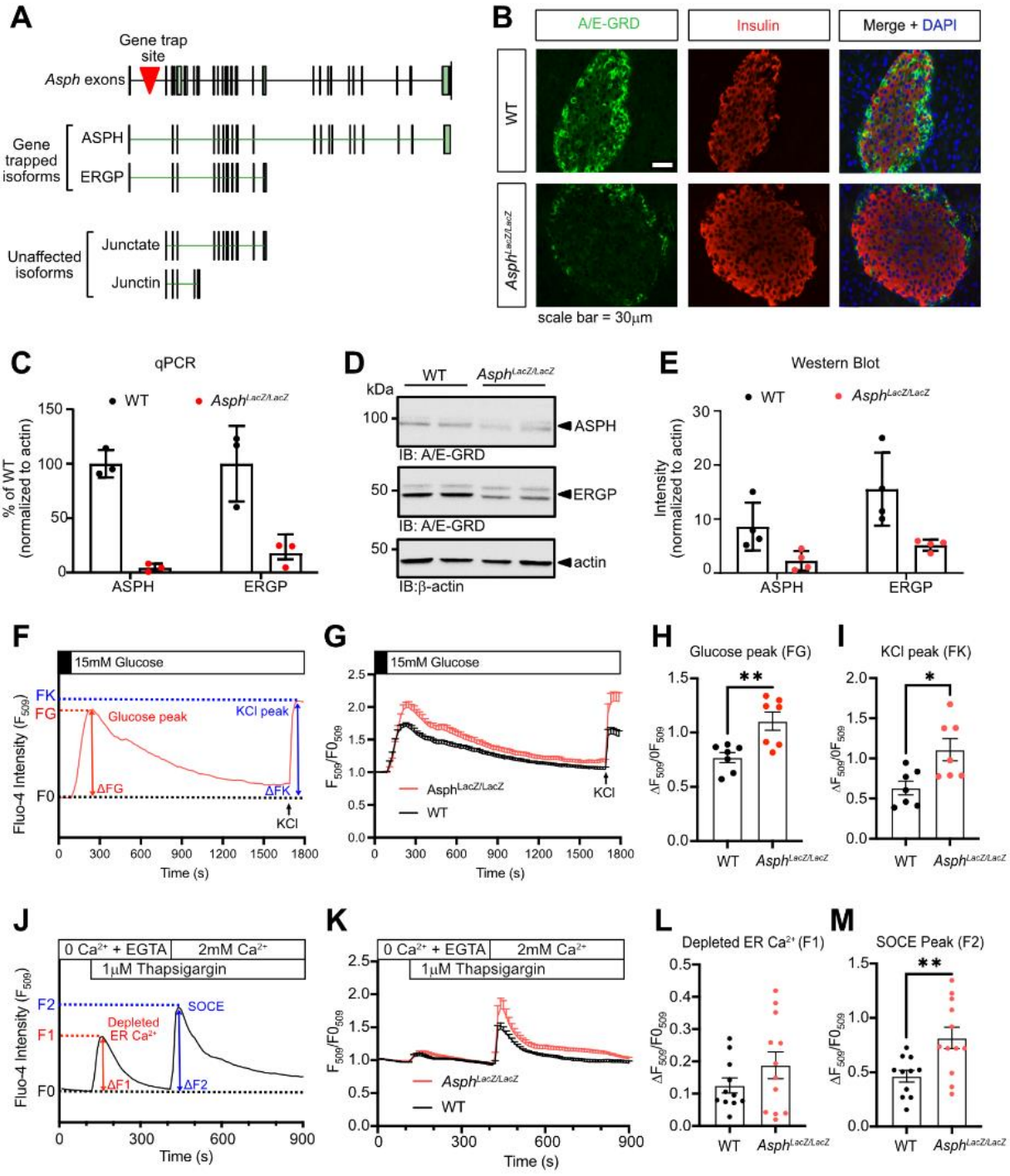
A
Gene trap site
Asph exons
Gene trapped isoforms
ASPH
ERGP
Unaffected isoforms
Junctate
Junctin
B
A/E-GRD
Insulin
Merge + DAPI
WT
AsphLacZ/LacZ
scale bar = 30μm
C
qPCR
WT
AsphLacZ/LacZ
% of WT (normalized to actin)
ASPH
ERGP
D
kDa
WT
AsphLacZ/LacZ
ASPH
IB: A/E-GRD
ERGP
IB: A/E-GRD
actin
IB:β-actin
E
Western Blot
Intensity (normalized to actin)
F
15mM Glucose
FK
FG
Glucose peak
KCl peak
ΔFG
ΔFK
F0
KCl
Fluo-4 Intensity (F509)
Time (s)
G
15mM Glucose
AsphLacZ/LacZ
WT
KCl
F509/F0509
Time (s)
H
Glucose peak (FG)
ΔF509/0F509
I
KCl peak (FK)
J
0 Ca2+ + EGTA
2mM Ca2+
1μM Thapsigargin
F2
F1
F0
Depleted ER Ca2+
SOCE
ΔF1
ΔF2
Fluo-4 Intensity (F509)
Time (s)
K
0 Ca2+ + EGTA
2mM Ca2+
1μM Thapsigargin
AsphLacZ/LacZ
WT
F509/F0509
Time (s)
L
Depleted ER Ca2+ (F1)
ΔF509/F0509
M
SOCE Peak (F2)
ΔF509/F0509

Figure 1. SOCE and glucose stimulated Ca^{2+} flux is elevated in semi-dispersed beta-cells isolated from *Asph*$^{LacZ/LacZ}$ mice

A) Schematic of the *Asph*$^{LacZ/LacZ}$ gene locus depicting the insertion site of the pGT0Lxf gene trap vector and expected "gene-trapped" isoforms. B) Immunofluorescence on pancreas sections from WT or *Asph*$^{LacZ/LacZ}$ mice using anti-A/E-GRD and anti-insulin antibodies. C) mRNA expression analysis of ASPH and ERGP by qPCR on isolated islets from WT or *Asph*$^{LacZ/LacZ}$ mice (n=3). D) Protein expression in isolated islets from WT and *Asph*$^{LacZ/LacZ}$ mice by Western blot. E) Quantification of ASPH and ERGP from D (n=4). F) Schematic for Ca^{2+} imaging of semi-dispersed beta-cells in Kreb-Ringer's solution with 5mM glucose, 15mM glucose, and high KCl (30mM). G) Fluo-4 measurement of cytosolic Ca^{2+} in semi-dispersed beta-cells taken from WT or *Asph*$^{LacZ/LacZ}$ mice using protocol depicted in F (n=7). H and I) Peak cytosolic Ca^{2+} level recorded at (H) 15mM glucose and (I) 30mM KCl normalized to the baseline at 5mM glucose (n=7). J) Schematic of the Ca^{2+} addback protocol, the strategy used to measure and quantify store-operated Ca^{2+} entry (SOCE) by live-cell imaging. K) SOCE measured by Ca^{2+} imaging of semi-dispersed beta-cells from WT or *Asph*$^{LacZ/LacZ}$ mice (n=11-12). L and M) Peak cytosolic Ca^{2+} level recorded following addition of (L) 1mM Thapsigargin and M) 2mM Ca^{2+} normalized to baseline in Ca^{2+} free buffer (n=11-12)

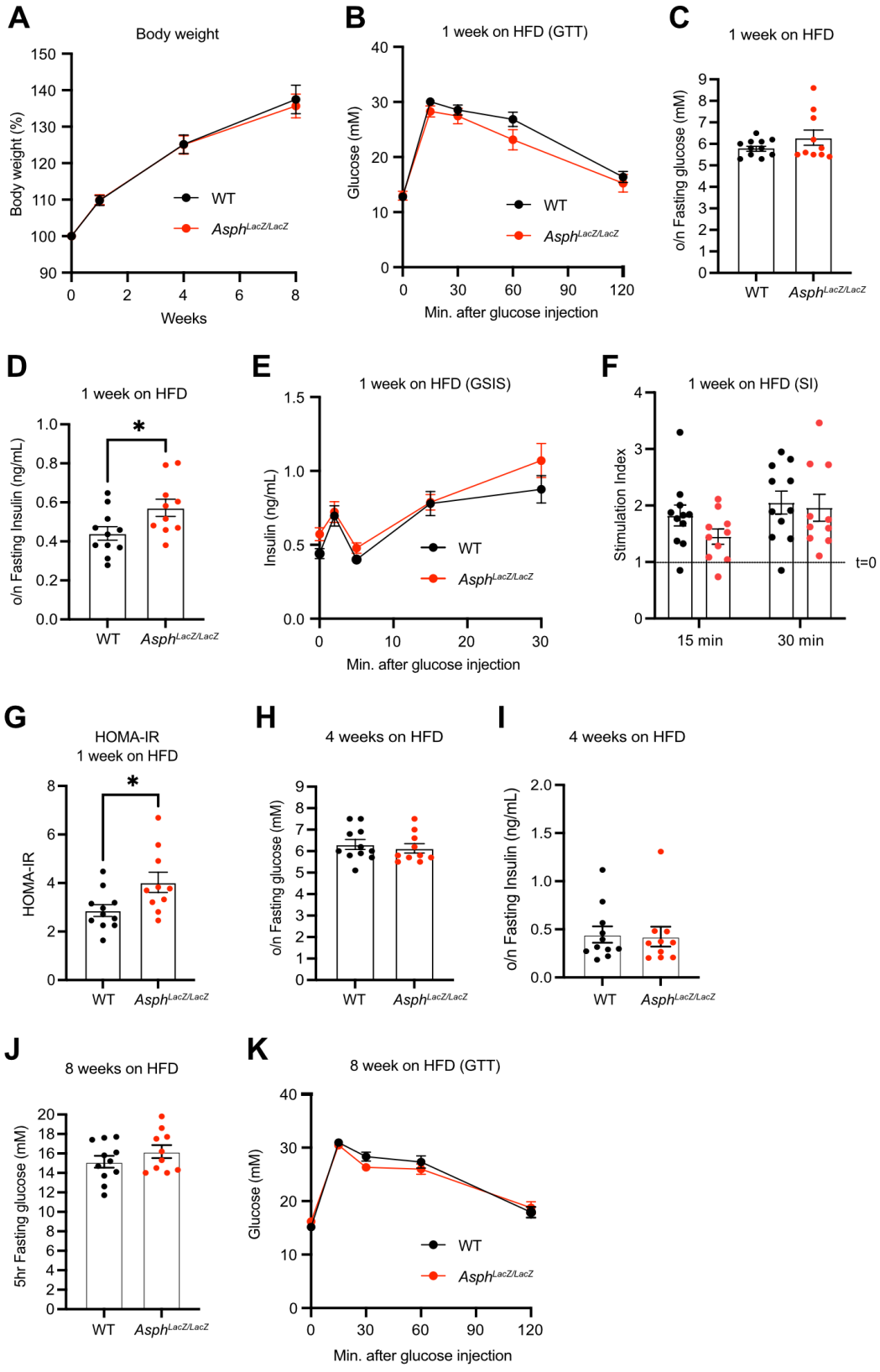
A
Body weight
Body weight (%)
Weeks
WT
Asph LacZ/LacZ
B
1 week on HFD (GTT)
Glucose (mM)
Min. after glucose injection
C
1 week on HFD
o/n Fasting glucose (mM)
D
1 week on HFD
o/n Fasting Insulin (ng/mL)
E
1 week on HFD (GSIS)
Insulin (ng/mL)
F
1 week on HFD (SI)
Stimulation Index
t=0
15 min
30 min
G
HOMA-IR
1 week on HFD
H
4 weeks on HFD
I
4 weeks on HFD
J
8 weeks on HFD
5hr Fasting glucose (mM)
K
8 week on HFD (GTT)

Figure 2. *Asph*$^{LacZ/LacZ}$ mice do not have significantly altered glucose tolerance or glucose stimulated insulin secretion (GSIS) compared to WT mice

A) Body weight of male WT and *Asph*$^{LacZ/LacZ}$ mice fed a high fat diet (HFD) over 8 weeks (n=10-11). B) Intraperitoneal glucose tolerance test (GTT) performed on mice fed a HFD for 1 week (n=10-11). C and D) Blood (C) glucose and (D) insulin levels of mice fed HFD for 1 week following overnight fasting (n=10-11). E) GSIS of mice fed HFD for 1 week (n=10-11). F) Stimulation index (SI) calculation at 15min and 30 min from E (n=10-11). G) HOMA-IR of mice fed HFD for 1 week (n=10-11). H and I) Blood (H) glucose and (I) insulin levels of mice fed HFD for 4 weeks following overnight fasting (n=10-11). J) Blood glucose levels of mice fed HFD for 8 weeks following overnight fasting (n=10-11). K) GTT performed on mice fed a HFD for 8 weeks (n=10-11).

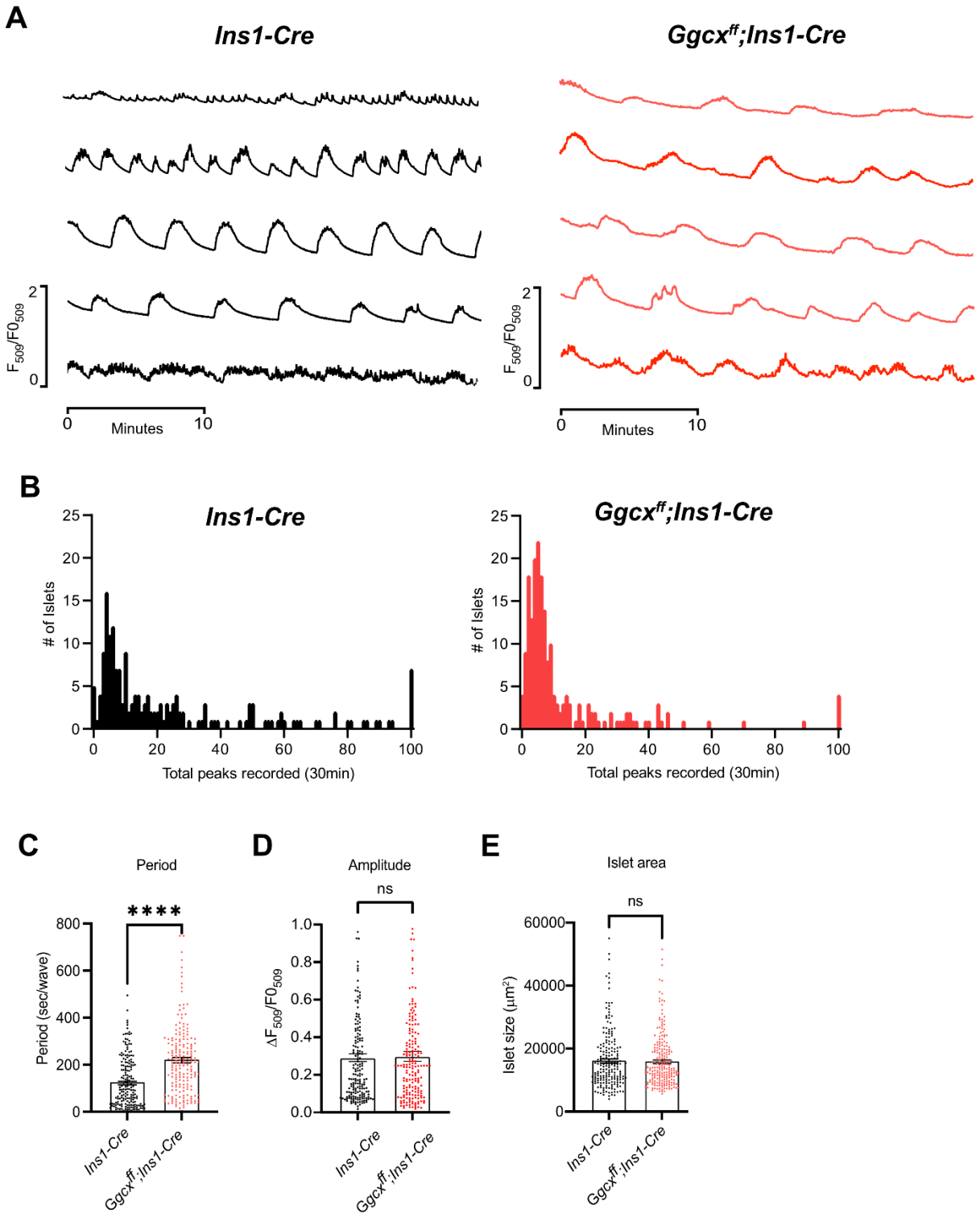
A
Ins1-Cre
Ggcx^ff;Ins1-Cre
F509/F0509
2
0
0
Minutes
10
B
Ins1-Cre
Ggcx^ff;Ins1-Cre
# of Islets
25
20
15
10
5
0
0
20
40
60
80
100
Total peaks recorded (30min)
C
Period
****
Period (sec/wave)
800
600
400
200
0
Ins1-Cre
Ggcx^ff;Ins1-Cre
D
Amplitude
ns
ΔF509/F0509
1.0
0.8
0.6
0.4
0.2
0.0
Ins1-Cre
Ggcx^ff;Ins1-Cre
E
Islet area
ns
Islet size (μm2)
60000
40000
20000
0
Ins1-Cre
Ggcx^ff;Ins1-Cre

Figure 3. Beta-cell specific knockout of GGCX increases the period of whole islet Ca^{2+} oscillations

A) Representative Cal-520 cytosolic Ca^{2+} traces taken from 5 islets isolated from *Ins1-Cre* and *Ggcx^{ff};Ins1-Cre* mice at 11mM glucose. B) Histogram depicting distribution of number of peaks detected throughout the 30 minute recording period for islets from *Ins1-Cre* and *Ggcx^{ff};Ins1-Cre* mice (n=182-189). C-E) Quantification of the average (C) oscillatory period, (D) amplitude of oscillation, and (E) surface area of the islets (n=182-189).

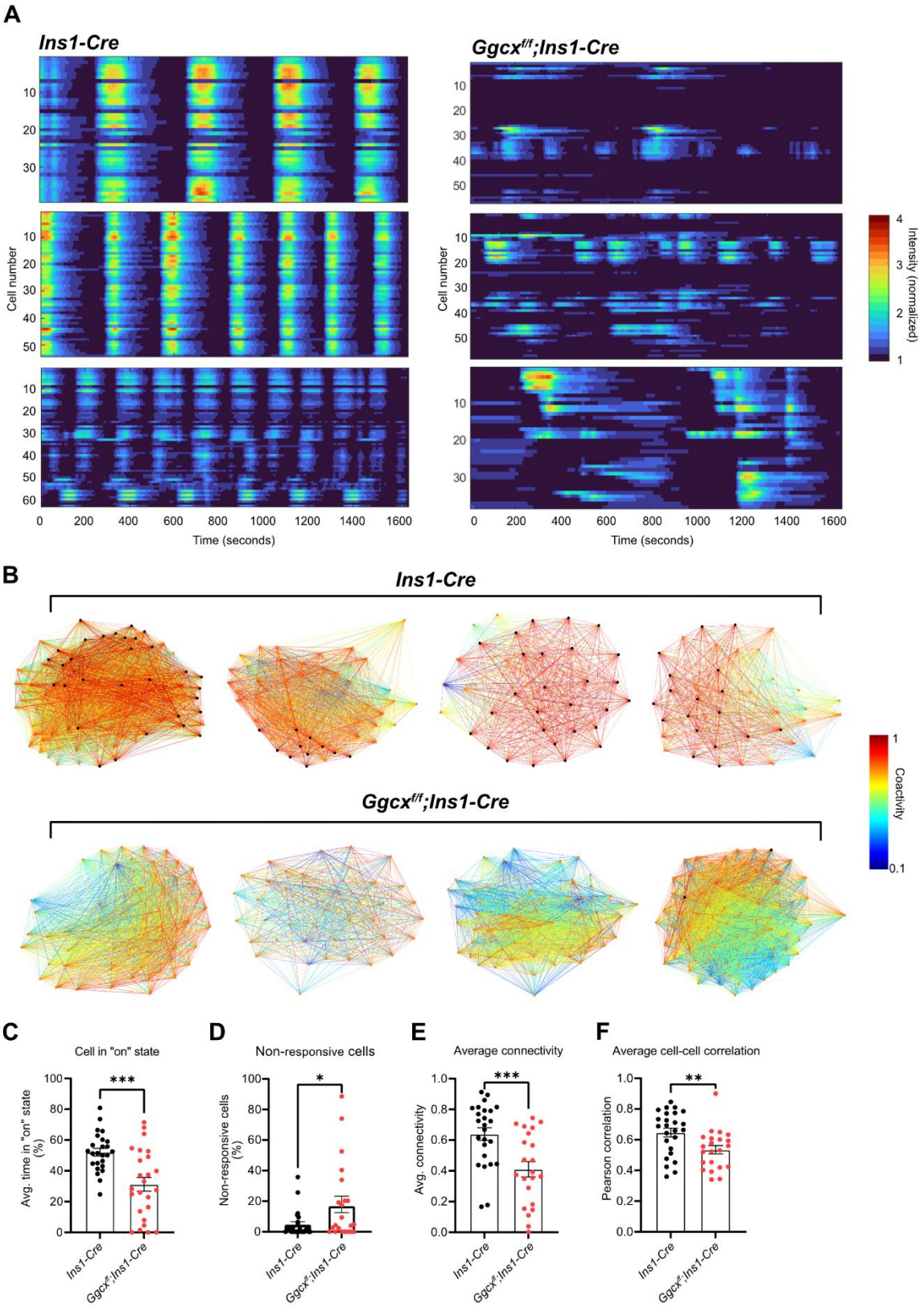
A
Ins1-Cre
Ggcx^f/f;Ins1-Cre
Cell number
Time (seconds)
Intensity (normalized)
B
Ins1-Cre
Ggcx^f/f;Ins1-Cre
Coactivity
C
Cell in "on" state
Avg. time in "on" state (%)
D
Non-responsive cells
Non-responsive cells (%)
E
Average connectivity
Avg. connectivity
F
Average cell-cell correlation
Pearson correlation
Ins1-Cre
Ggcx^f/f;Ins1-Cre

Figure 4. Beta-cell specific knockout of GGCX reduces islet connectivity and coactivity

A) Temporal raster plots of individual cells from 3 islets taken from *Ins1-Cre* or *Ggcx^{ff};Ins1-Cre* mice. B) Islet cell connectivity analysis. Nodes represent cells and lines represent coactivity >0.1. Black nodes represent highly connected cells. C-F) Summary for the average values from individual cells in each islet (n=25): (C) percentage of time spent in "on" state, (D) percentage of non-responsive cells, (E) coactivity of cells, (F) Pearson correlation

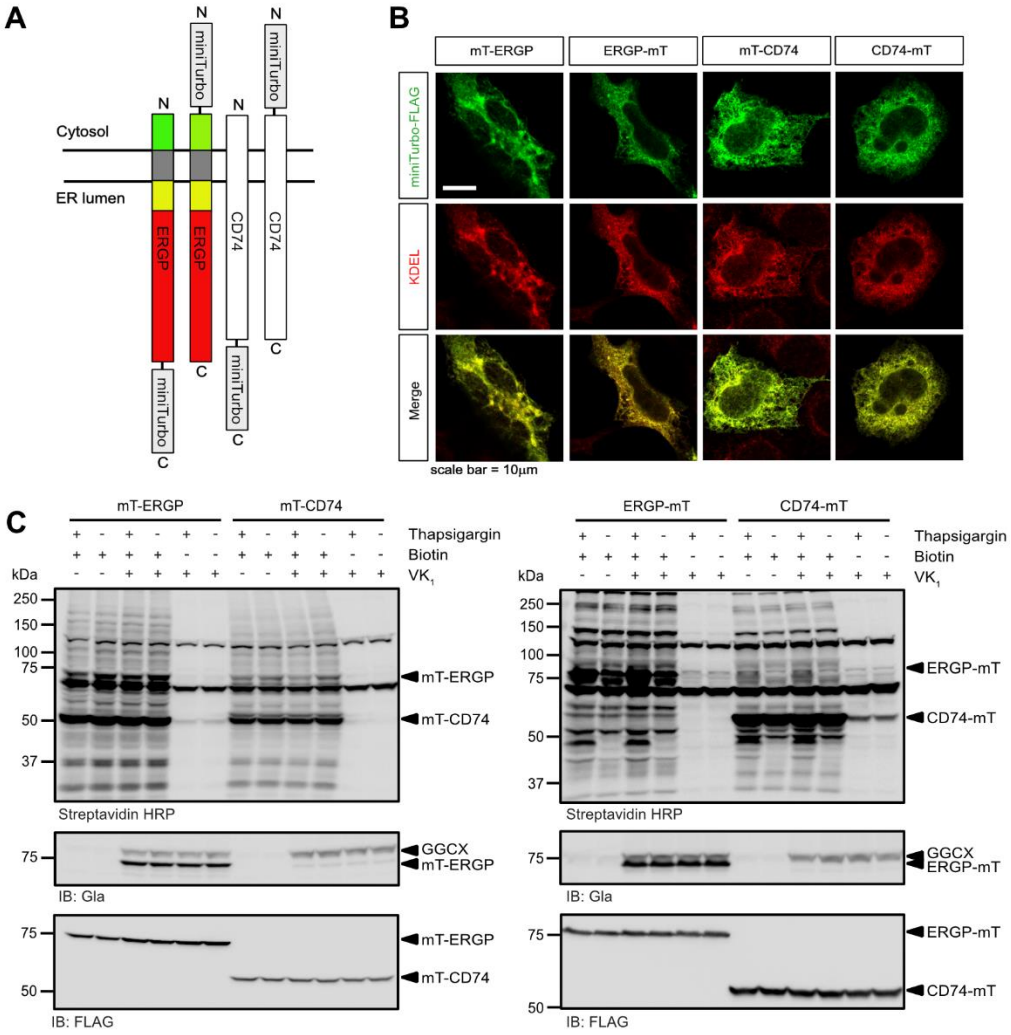
A
N
miniTurbo
N
miniTurbo
N
Cytosol
ER lumen
ERGP
ERGP
CD74
CD74
C
C
miniTurbo
C
miniTurbo
C
B
mT-ERGP
ERGP-mT
mT-CD74
CD74-mT
miniTurbo-FLAG
KDEL
Merge
scale bar = 10μm
C
mT-ERGP
mT-CD74
ERGP-mT
CD74-mT
Thapsigargin
Biotin
VK1
kDa
250
150
100
75
50
37
mT-ERGP
mT-CD74
ERGP-mT
CD74-mT
Streptavidin HRP
GGCX
IB: Gla
IB: FLAG
D
0mM Ca2+ +EGTA
2mM Ca2+
1μM Thapsigargin
mT-ERGP
mT-ERGP +VK
F509/F660
Time (s)
E
Baseline Ca2+ (F0)
mT-ERGP
F
Depleted ER Ca2+ (F1)
mT-ERGP
G
SOCE Peak (F2)
mT-ERGP
ΔF509/F660
VK1
H
0mM Ca2+ +EGTA
2mM Ca2+
1mM Thapsigargin
ERGP-mT
ERGP-mT +VK
I
Baseline Ca2+ (F0)
ERGP-mT
J
Depleted ER Ca2+ (F1)
ERGP-mT
K
SOCE Peak (F2)
ERGP-mT

Figure 5. ERGP-miniTurbo fusion proteins generated and validated for use in TurboID screen

A) Schematic of constructs used in Turbo ID screen. From left to right, mT-ERGP, ERGP-mT, mT-CD74, CD74-mT. ERGP fusion schematics depict the cytosolic tail (green), transmembrane domain (grey), putative EF hand domain (yellow), and Glu rich domain (red). B) Immunofluorescent staining of HEK293 cells expressing each TurboID construct with anti-FLAG antibody and anti-KDEL antibody. C) Expression, carboxylation, and biotinylating activity of TurboID constructs by Streptavidin HRP and Western blot. Cells were treated with or without thapsigargin (1mM), VK_1 (22 mM), and biotin (50mM). D) SOCE measured by ratiometric Ca^{2+} imaging of HEK293 transfected with mT-ERGP with Fluo-4 and Fura Red in the presence or absence of 22mM VK_1 (n=5). E) Quantification of average fluorescent ratio at baseline (0-100 seconds) in D (n=5). F and G) Quantification of peak fluorescent ratio during (F) thapsigargin induced ER Ca^{2+} efflux (120-400 seconds), and G) SOCE peak (420-900 seconds) in D (n=5). H) SOCE measured by ratiometric Ca^{2+} imaging of HEK293 transfected with ERGP-mT as in D (n=4). I-K) Quantification of (I) baseline, (J) ER Ca^{2+} efflux, and (K) SOCE peak for H as in E-G (n=4).

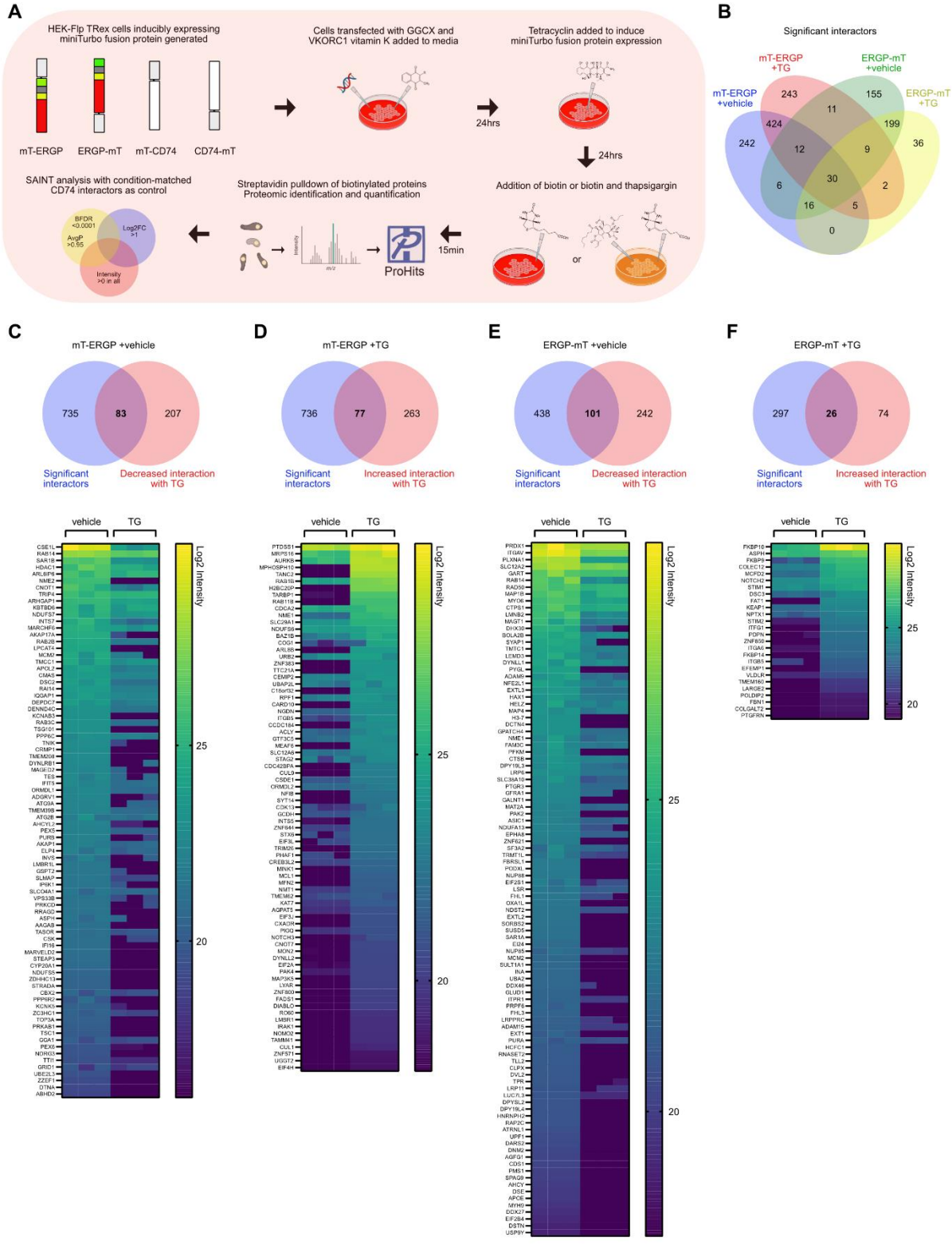
A
HEK-Flp TRex cells inducibly expressing miniTurbo fusion protein generated
mT-ERGP
ERGP-mT
mT-CD74
CD74-mT
Cells transfected with GGCX and VKORC1 vitamin K added to media
24hrs
Tetracyclin added to induce miniTurbo fusion protein expression
24hrs
Addition of biotin or biotin and thapsigargin
or
15min
Streptavidin pulldown of biotinylated proteins
Proteomic identification and quantification
ProHits
SAINT analysis with condition-matched CD74 interactors as control
BFDR <0.0001
AvgP >0.95
Log2FC >1
Intensity >0 in all
B
Significant interactors
mT-ERGP +TG
ERGP-mT +vehicle
mT-ERGP +vehicle
ERGP-mT +TG
243
155
11
424
199
242
12
9
36
6
30
2
16
5
0
C
mT-ERGP +vehicle
735
83
207
Significant interactors
Decreased interaction with TG
D
mT-ERGP +TG
736
77
263
Significant interactors
Increased interaction with TG
E
ERGP-mT +vehicle
438
101
242
Significant interactors
Decreased interaction with TG
F
ERGP-mT +TG
297
26
74
Significant interactors
Increased interaction with TG
vehicle
TG
Log2 Intensity
25
20

Figure 6. ERGP specific interactors modulated by ER Ca^{2+} depletion with thapsigargin identified with TurboID

A) Schematic depicting workflow of TurboID experiment. Cells are transfected with GGCX and VKORC1 and supplemented with VK_1 before miniTurbo fusion protein expression is induced with tetracyclin 24 hours later. Biotin is then added with or without thapsigargin for 15 minutes before cells are harvested, lysed, and the biotinylated proteins pulled down with streptavidin coated beads. The pulled down proteins are then identified with LC-MS/MS and SAINT analysis is used to identify ERGP specific interactors via comparison with condition matched CD74 controls. B) Venn diagram of significant interactors identified for mT-ERGP or ERGP-mT with or without thapsigargin (n=3). C-F) Venn diagram overlap of. significant interactors (blue) which are modulated by thapsigargin (red). Normalized intensities of significant interactors modulated by thapsigargin (overlap) plotted on heatmap below (n=3). C and D) Significant interactors of mT-ERGP which are (C) downregulated or (D) upregulated by thapsigargin. E and F) Significant interactors of ERGP-mT which are (E) downregulated or (F) upregulated by thapsigargin

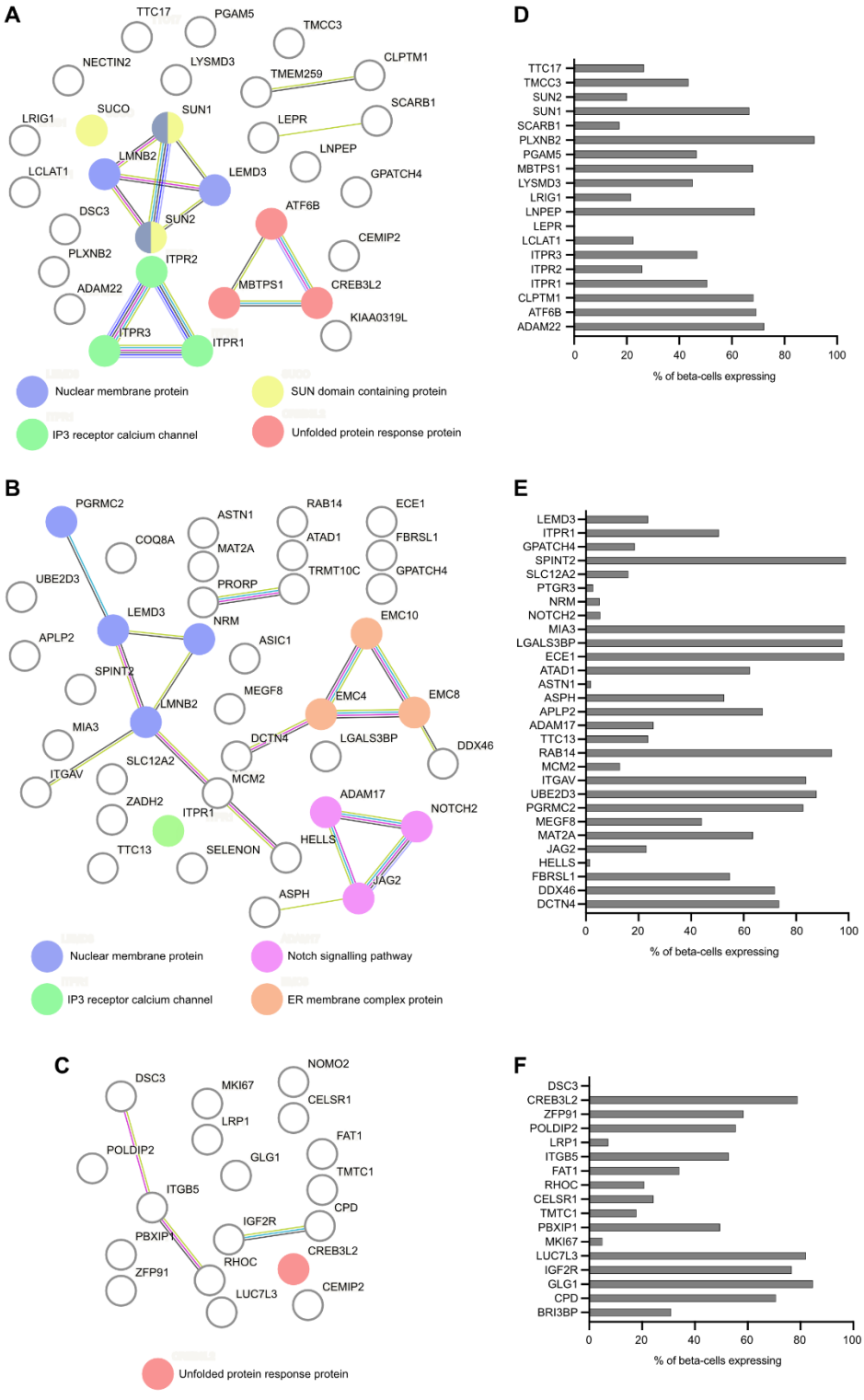
A
TTC17
PGAM5
TMCC3
NECTIN2
LYSMD3
CLPTM1
TMEM259
SCARB1
SUCO
SUN1
LRIG1
LEPR
LNPEP
LMNB2
LCLAT1
LEMD3
GPATCH4
DSC3
ATF6B
SUN2
CEMIP2
PLXNB2
ITPR2
ADAM22
MBTPS1
CREB3L2
KIAA0319L
ITPR3
ITPR1
Nuclear membrane protein
SUN domain containing protein
IP3 receptor calcium channel
Unfolded protein response protein
B
PGRMC2
ASTN1
RAB14
ECE1
COQ8A
MAT2A
ATAD1
FBRSL1
UBE2D3
TRMT10C
GPATCH4
PRORP
LEMD3
NRM
EMC10
APLP2
ASIC1
SPINT2
MEGF8
EMC4
EMC8
LMNB2
MIA3
DCTN4
LGALS3BP
DDX46
SLC12A2
ITGAV
MCM2
ZADH2
ADAM17
NOTCH2
ITPR1
HELLS
TTC13
SELENON
JAG2
ASPH
Nuclear membrane protein
Notch signalling pathway
IP3 receptor calcium channel
ER membrane complex protein
C
NOMO2
DSC3
MKI67
CELSR1
LRP1
FAT1
POLDIP2
GLG1
TMTC1
ITGB5
CPD
IGF2R
PBXIP1
CREB3L2
RHOC
ZFP91
CEMIP2
LUC7L3
Unfolded protein response protein
D
TTC17
TMCC3
SUN2
SUN1
SCARB1
PLXNB2
PGAM5
MBTPS1
LYSMD3
LRIG1
LNPEP
LEPR
LCLAT1
ITPR3
ITPR2
ITPR1
CLPTM1
ATF6B
ADAM22
0
20
40
60
80
100
% of beta-cells expressing
E
LEMD3
ITPR1
GPATCH4
SPINT2
SLC12A2
PTGR3
NRM
NOTCH2
MIA3
LGALS3BP
ECE1
ATAD1
ASTN1
ASPH
APLP2
ADAM17
TTC13
RAB14
MCM2
ITGAV
UBE2D3
PGRMC2
MEGF8
MAT2A
JAG2
HELLS
FBRSL1
DDX46
DCTN4
0
20
40
60
80
100
% of beta-cells expressing
F
DSC3
CREB3L2
ZFP91
POLDIP2
LRP1
ITGB5
FAT1
RHOC
CELSR1
TMTC1
PBXIP1
MKI67
LUC7L3
IGF2R
GLG1
CPD
BRI3BP
0
20
40
60
80
100
% of beta-cells expressing

Figure 7. ERGP interacts with proteins involved in ER Ca^{2+} regulation, unfolded protein response (UPR), and cell-cell signalling

A-C) Schematics depicting proteins identified as significant interactors of ERGP in (A) all conditions, (B) significantly downregulated by thapsigargin in both the mT-ERGP and ERGP-mT conditions, and (C) significantly upregulated by thapsigargin in both the mT-ERGP and ERGP-mT conditions. D-F) Percentage of beta-cells expressing significant interactors depicted in in (D) A, (E) B, or (F) C as determined by single cell RNA sequencing (n=449). No data was available for missing proteins

MATERIALS AND METHODS

Asph gene trap mouse line generation

The mouse embryonic stem (ES) cell containing the pGT0Lxf gene trap vector between the first and second exon of *Asph* was procured (BayGenomics; $Asph^{Gt(YTC425)Byg}$) and added to blastocytes of C57B6/J mice via microinjection before transplantation into a pseudo-pregnant female. Transmission of the genetrap vector was confirmed using PCR and mice were backcrossed with C57B6/J mice for 9 generations before use in experiments.

Mouse islet isolation

Mouse islets were isolated as previously described [189]. Following perfusion with Liberase TL (Roche Applied Science; 05401020001) through the pancreatic duct and subsequent digestion at 37ºC, islets were isolated using Histopaque-1077 density gradient separation (Millipore Sigma) before being handpicked under a steromicroscope (SteREO Discovery.V12;Zeiss).

Immunofluorescent staining

The pancreases were fixed in 10% formalin at room temperature for 24 hours, then embedded in paraffin and sliced into 5µm sections. The sections were rehydrated and subjected to antigen retrieval by boiling in 10mM sodium citrate pH 6.0 for 10 minutes before immunofluorescent staining. HEK293 cells or semi-dispersed islets were fixed in 4% paraformaldehyde in PBS for 15 minutes at room temperature and washed 3 times with PBS before immunofluorescent staining.

This was done by first blocking in PBS containing 5% normal donkey serum and 0.3% Triton for 1 hour at room temperature. Sections or cells were then incubated with primary antibodies diluted in PBS containing 1% BSA and 0.1% Triton overnight at 4ºC. Primary antibodies used

were goat anti-insulin (sc-7839; Santa Cruz Biotechnology), rabbit anti-A/E-GRD antibody generated by our laboratory to detect ASPH and ERGP [189], rabbit anti-FLAG antibody (14793; Cell Signaling), and mouse anti-KDEL antibody (ab12223; Abcam). Next, sections or cells were incubated with corresponding fluorescent secondary antibodies in PBS containing 1% BSA and 0.1% Triton for 1 hour at room temperature. Secondary antibodies used were Cy3-conjugated donkey anti-mouse (715-165-150; Jackson Immunoresearch Laboratories), Alexa-Fluor 488-conjugated donkey anti-rabbit (711-545-152; Jackson Immunoresearch Laboratories), and Alexa-Fluor 594-conjugated donkey anti-goat (705-585-147; Jackson Immunoresearch Laboratories). Nuclei were stained with DAPI where indicated.

Pancreas sections were imaged using the DM5500B fluorescence microscope (Leica) with a 40x objective. HEK293 cells were imaged using the scanning confocal LSM710 (Zeiss) with a 63x oil immersion objective.

Islet qPCR analysis

qPCR analysis of islets was done as previously described [189]. 20-40 islets were taken from each mouse and each experimental replicate represents the pooled islets from a single mouse.

Western blot

Islets were homogenized in a Triton based lysis buffer (20mM Tris-HCl (pH 7.5), 150mM NaCl, 1mM EDTA (pH 8.0), 1mM EGTA, 2.5mM NaPyrophosphate, 1mM b-glycerophosphate, 10mM NaF, 1% Triton, 1mM phenylmethylsulfonyl fluoride (PMSF) and protease inhibitors (4693132001; Roche Diagnostics)). HEK293 cells were homogenized then sonicated in RIPA buffer (1% NP-40, 0.1% SDS, 50mM Tris-HCl (pH 7.5), 150mM NaCl, 12mM sodium deoxycholate, 1mM EDTA, 0.1mM DTT, 1mM PMSF and protease inhibitors).

Islet or cell lysates were then denatured at 70ºC in Laemmli buffer for 10 minutes before resolving on 7.5% polyacrylamide Tris-Glycine gels. Proteins were then detected using standard Western blot procedures and revealed by horseradish peroxidase (HRP)-conjugated secondary antibodies and luminol solution on a ChemiDoc Imaging System (BioRad). Primary antibodies used were rabbit anti-A/E-GRD antibody, mouse anti-beta-actin antibody (A1978; Millipore Sigma), rabbit anti-Gla antibody generated by our laboratory [56], and rabbit anti-Flag antibody. Biotinylated proteins were detected using HRP-conjugated streptavidin (N100; ThermoFisher).

Metabolic analysis

10 week old male mice were placed on a high fat diet (HFD) comprised of 60% kcal from fat for up to 8 weeks (TD.06414; Envigo). In addition to metabolic tests, measurements of fasting glucose, insulin, and body weight were taken during this time. To examine glucose stimulated insulin secretion (GSIS), blood glucose was measured from blood taken from the tail vein after an over-night fast at 2, 5, 15, and 30 minute intervals following glucose injection (3g/kg). Serum insulin was quantified using ELISA. The stimulation index was defined as the fold change in serum insulin at 15 and 30 minutes divided by the fasting serum insulin level. Glucose tolerance tests (GTT) involved blood glucose measurements at 15, 30, 60, and 120 minute intervals following an (5h fasting) post-glucose injection (1.5g/kg, i.p.). Homeostatic model assessment of insulin resistance (HOMA-IR) was calculated using the following equation: fasting glucose (mM) x fasting insulin (mU/mL)/22.5

Semi-dispersed islet and HEK293 cell Ca^{2+} imaging

Islets were isolated as previously described and semi-dispersed by brief digestion with 0.025% Trypsin-EDTA for 1 minute followed by up and down pipetting until islets are just dispersed.

Cells are then washed twice with culture medium (RPMI, 10%FBS, penicillin/streptomycin) to remove Trypsin-EDTA. Islets are then dropped in 200μL drops onto glass coverslips (18mm diameter, #1.5 thickness; 72290-08; Electron Microscopy Sciences) and allowed to attach for 30 minutes at 37ºC. 1mL of culture media is then added to each coverslip and the dispersed islet cells are allowed to recover overnight where they will form clusters. The islet cells are then loaded with 5μM Fluo-4 AM in Kreb-Ringer's solution (114mM NaCl, 1.2mM KH_2PO_4, 4.7mM KCl, 1.16mM $MgSO_4$, 25.5mM $NaHCO_3$, 2.5mM $CaCl_2$, 5mM glucose, 20mM HEPES, 0.2% fatty acid free BSA) for 30 minutes at room temperature before being washed twice and the AM dye allowed to esterify for 30 more minutes at room temperature.

For SOCE measurements with Ca^{2+} addback protocol, cells were transferred to Ca^{2+} free Kreb-Ringer's solution with 1mM EGTA, 200μM diazoxide (D9035; MilliporeSigma), and 10μM verapamil (V4629; MilliporeSigma) for 5 minutes before baseline measurements (F0) were recorded for 120 seconds. Thapsigargin was then added to 1μM and at 420 seconds $CaCl_2$ added to a free Ca^{2+} concentration of 2mM.

For glucose stimulated Ca^{2+} flux measurements, cells were left in the Kreb-Ringer's solution following the esterification step and baseline measurements (F0) were made for 90 seconds before glucose was raised to 15mM. The islet cells were then recorded from 90-1700 seconds before the KCl concentration was raised to 30mM.

HEK293 cells were plated on glass coverslips coated with poly-L-lysine (P1274; MilliporeSigma). Glass coverslips were coated as previously described [189]. HEK 293 cells were loaded with 5μM Fluo-4 AM and 2.5μM Fura Red AM (F3021; Invitrogen) in a HEPES-buffered saline solution (HBSS; 120mM NaCl, 5mM KCl, 0.8mM MgSO4, 2mM CaCl2, 10mM

Glucose, 20mM HEPES, pH 7.4) containing 0.02% pluronic F-127 (P6866; Invitrogen) at 37°C for 30 minutes. Cells were then washed twice with HBSS and incubated for an additional 30 minutes at 37°C to allow complete de-esterification of intracellular AM esters. Ca2+ imaging for SOCE measurements was performed in Ca2+ free HBSS containing 1mM EGTA. Ca^{2+} addback protocol was performed as described above.

Imaging was performed on a confocal rotary disk inverted microscope from Zeiss equipped with a Yokogawa CSU-1 module using a 20X objective as previously described [189]. Cells were imaged at a frequency of 5 seconds per image. The microscope is equipped with a mounted incubator and warmed imaging chamber, which was heated to 37ºC during imaging.

Whole islet Ca^{2+} imaging

Islets were isolated as described above and allowed to recover in culture media containing 22μM VK overnight. Islets were then transferred to 1.5mL eppendorph tubes and washed with Kreb-Ringer's solution with 11mM glucose before being loaded with 5μM Cal-520 AM in 11mM glucose Kreb-Ringer's solution containing 0.02% pluronic F-127 at 37ºC for 1 hour. The islets were then washed twice with 11mM glucose Kreb-Ringer's solution before being placed into the imaging chamber.

Islets were them imaged on the confocal rotary disk inverted microscope described above at 37ºC at a frequency of 1 second per image.

Ca^{2+} imaging analysis

Timelapses were taken using the confocal spinning disk as described above and saved as Carl Zeiss Image files. Files were then imported to Fiji [221] as 16-bit greyscale timelapses. Where multiple dyes were used for ratiometric Ca^{2+} measurements, multiple channels all in greyscale

were used to represent each dye. Regions of interest (ROIs) were selected manually depending on the experiment (individual islet cells, whole islets, or individual HEK293 cells). Mean grey values were taken for each frame of the timelapse as fluorescence intensity. SOCE and glucose stimulated Ca^{2+} flux measurement analysis was performed as previously described [189].

The peaks, troughs, average period, and amplitude of oscillation for the whole islet Ca^{2+} oscillation traces was assessed using a custom MatLab script generated by the Merrins' lab (script available at: https://github.com/hrfoster/Merrins-Lab-Matlab-Scripts).

Islet coactivity and the presence of highly connected cells were determined as follows: Matlab scripts were employed to ascertain the proportion of time each cell within a given islet was "on" at the same time as other cells. To achieve this, the Ca^{2+} signal from each cell underwent smoothing by averaging the fluorescence values of 20 frames, equivalent to about 7 seconds. A moving baseline was utilized to establish the "off" state, defined as the minimal 20-frame fluorescence value achieved in a time frame of 140 seconds. An islet cell was considered "on" if the 20-frame moving average rose 20% higher than the previously defined baseline. Coactivity, indicating the time two cells spent being active together, was computed according to previously published papers [222], resulting in a value between 0 (never active simultaneously) and 1 (essentially the same cell). Statistical significance was determined by assessing if the value could be obtained by chance through permutation. Identification of "hubs," highly connected cells, followed specific criteria: a cell qualified as a hub if at least 20% of its connections exhibited a coactivity value equal to or greater than 0.9, representing the strength of the connections. Correlation was computed by determining the Pearson correlation smoothed fluorescence data and significance was assessed by bootstrapping for each islet cell with every other islet cell.

DNA constructs, transfection, and cell line generation

miniTurbo fusion constructs were all generated using Gibson assembly with the NEBuilder® HiFi DNA Assembly Master Mix (M5520;New England Biolabs). ERGP-mT was assembled from the PCR product of the previously described ERGP-3xFLAG construct [189] and the pcDNA5-pDEST-FRT-MiniTurboID-Flag-c-term vector [223]. mT-ERGP was assembled with the first 11 amino acids of ERGP preceding miniTurbo-Flag followed by the rest of ERGP to ensure proper ER localization of the protein. mT-ERGP was also assembled from the PCR product of ERGP-3xFLAG and the pcDNA5-pDEST-FRT-MiniTurboID-Flag-n-term vector [223]. CD74-mT was assembled from the PCR product of the Str-Ii_neomycin construct (65312;Addgene) and the pcDNA5-pDEST-FRT-MiniTurboID-Flag-c-term vector. mT-CD74 was assembled with the first 22 amino acids of CD74 preceding miniTurbo-Flag followed by the rest of CD74 to ensure proper ER localization of the protein. It was assembled from the Str-Ii_neomycin construct and the pcDNA5-pDEST-FRT-MiniTurboID-Flag-n-term vector.

Flp-In T-Rex HEK293 (R78007, Thermo Fisher Scientific) stable cell lines were generated by transfection of the pDEST-FRT vector (1 μg) and the Flp recombinase containing vector (pOG44) (V600520, Thermo Fisher Scientific) (2 μg) with Lipo2000 (11668019, Thermo Fisher Scientific) according to the manufacturer. Cells were then selected with 200 μg/mL of Hygromycin B (10687010, Thermo Fisher Scientific) for 2-3 weeks.

Interactor biotinylation, streptavidin pulldown, and mass spectrometry analysis

$1x10^6$ cells were plated onto 10cm tissue culture dishes. 3 days later, cells were transfected with 5μg each of previously generated “tagless” pcDNA3.1-GGCX and pcDNA3.1-VKORC1 for a total of 10μg of DNA, as described above. The next day, 1μg/mL of tetracyclin was added to the media to induce expression of the miniTurbo fusion protein. 24 hours later, either 1μM

thapsigargin and 50μM biotin or only 50μM biotin was added to the media for 15 minutes. The media was then aspirated and the cells scraped into cold PBS before being washed twice with cold PBS. PBS was then aspirated and the cell pellet frozen at -80ºC until all replicates were ready to be processed.

Cell pellets were lysed in 1mL RIPA buffer (1% NP-40, 0.1% SDS, 50mM Tris-HCl pH 7.4, 150mM NaCl, 0.5% sodium deoxycholate, 1mM EDTA, 1mM DTT, 1mM PMSF, protease inhibitors) by sonication. Protein concentrations were then measured using the Pierce™ BCA protein assay kit (23225;ThermoFisher). 2.29mg of protein in 1mL of RIPA buffer was then added to 10μL of streptavidin sepharose beads (GE17-5113-01;SigmaAldrich) and incubated for 3 hours at 4ºC with rotation. The beads were then washed 3 times with RIPA buffer and washed 5 more times with 50mM ammonium bicarbonate pH 8.0.

The on-bead proteins were digested with 0.5 ug Sequencing Grade Modified Trypsin (Promega) overnight at 37ºC with agitation. The supernatants were collected, and the beads were washed two times with 100 ul water. The supernatants of each wash were pooled and then reduced and alkylated. The reduction step was done with 9 mM dithiothreitol at 37ºC for 30 minutes and, after cooling for 10 minutes, the alkylation step was done with 17 mM iodoacetamide at room temperature for 20 minutes in the dark. The supernatants were acidified with trifluoroacetic acid for desalting and removal of residual detergents by MCX (Waters Oasis MCX 96-well Elution Plate) following the manufacturer's instructions. After elution in 10% ammonium hydroxide /90% methanol (v/v), samples were dried with a Speed-vac, reconstituted under agitation for 15 min in 15 μL of 5%FA and loaded into a 75 μm i.d. × 150 mm Self-Pack C18 column installed in the Easy-nLC II system (Proxeon Biosystems). The buffers used for chromatography were 0.2% formic acid (buffer A) and 90% acetonitrile/0.2% formic acid (buffer B). Peptides were eluted

with a three-slope gradient at a flowrate of 250 nL/min. Solvent B first increased from 2 to 20% in 47 min, then from 20 to 37% B in 25 min and finally from 37 to 70% B in 7 minutes. The HPLC system was coupled to Orbitrap Fusion mass spectrometer (Thermo Scientific) through a Nanospray Flex Ion Source. Nanospray and S-lens voltages were set to 1.3-1.8 kV and 50 V, respectively. Capillary temperature was set to 250 °C. Full scan MS survey spectra (m/z 360-1550) in profile mode were acquired in the Orbitrap with a resolution of 120,000 with a target value at $8x10^5$. The 30 most intense peptide ions were fragmented in the HCD collision cell and analyzed in the linear ion trap with a target value at $2x10^4$ and a normalized collision energy at 29. Target ions selected for fragmentation were dynamically excluded for 40 sec after two MS/MS spectra.

SAINT analysis for TurboID

Raw mass spectrometry files were transformed to the .mzML format using ProteoWizard's MSConvert tool version 3.0.22055 [224] and analyzed by FragPipe (version 21.1) [225]. To prevent MBR (Match Between Runs) biases, searches were performed for each bait using LFQ-MBR default workflow settings. Searches were executed against the Uniprot's mouse non-redundant reference proteome (UP000000589 2022_12 release) [226], which was supplemented with the universal contaminant library [227] and reverse decoy sequences. The MSFragger parameters were set to default with trypsin specificity (two missed cleavage sites allowed), oxidation (M) and N-terminal acetylation as variable modifications, and cysteine carbamidomethyl as a fix modification. We discarded identified preys showing a protein probability lower than 0.7. To assess reproducibility and batch effects among bait replicates, we performed in R (r-project.org) multidimensional scaling (MDS) with the limma package (Ritchie et al, 2015), hierarchical clustering with the pvclust package (form Canberra distances and the

Ward.D2 clustering method) [228], and Spearman correlation analyses with the stats package using MS1 intensities from identified preys. Upon investigation, we corrected batch effects with the limma package and its removeBatchEffect function on Log2-transformed and median normalized data. Protein interactions were scored using the SAINTq algorithm [229] by compressing the control and bait samples based on the two highest MS1 intensity values, while preventing control normalization.

Statistical analysis

All statistical analysis was done using Graphpad Prism (version 9.3.1). Error bars in all figures denote standard error mean. For single measurements, an unpaired, 2-tailed Student's t-test was utilized. Grouped analysis involved one-way ANOVA, followed by Bonferroni's multiple comparisons test. For repeated measurements (metabolic tests), a two-way ANOVA followed by Bonferroni's post-tests was employed.

REFERENCES

1. Prentki, M. and C.J. Nolan, *Islet beta cell failure in type 2 diabetes.* J Clin Invest, 2006. **116**(7): p. 1802-12.
2. Lang, D.A., et al., *Brief, irregular oscillations of basal plasma insulin and glucose concentrations in diabetic man.* Diabetes, 1981. **30**(5): p. 435-9.
3. Satin, L.S., et al., *Pulsatile insulin secretion, impaired glucose tolerance and type 2 diabetes.* Mol Aspects Med, 2015. **42**: p. 61-77.
4. Benninger, R.K., et al., *Intrinsic islet heterogeneity and gap junction coupling determine spatiotemporal Ca^{2+} wave dynamics.* Biophys J, 2014. **107**(11): p. 2723-33.

5. Benninger, R.K., et al., *Gap junction coupling and calcium waves in the pancreatic islet.* Biophys J, 2008. **95**(11): p. 5048-61.

6. Salem, V., et al., *Leader β-cells coordinate Ca(2+) dynamics across pancreatic islets in vivo.* Nat Metab, 2019. **1**(6): p. 615-629.

7. Adams, M.T., et al., *Reduced synchroneity of intra-islet Ca(2+) oscillations in vivo in Robo-deficient β cells.* Elife, 2021. **10**.

8. Ravier, M.A., et al., *Loss of connexin36 channels alters beta-cell coupling, islet synchronization of glucose-induced Ca2+ and insulin oscillations, and basal insulin release.* Diabetes, 2005. **54**(6): p. 1798-807.

9. Head, W.S., et al., *Connexin-36 gap junctions regulate in vivo first- and second-phase insulin secretion dynamics and glucose tolerance in the conscious mouse.* Diabetes, 2012. **61**(7): p. 1700-7.

10. Farnsworth, N.L., et al., *Fluorescence recovery after photobleaching reveals regulation and distribution of connexin36 gap junction coupling within mouse islets of Langerhans.* J Physiol, 2014. **592**(20): p. 4431-46.

11. Camunas-Soler, J., et al., *Patch-Seq Links Single-Cell Transcriptomes to Human Islet Dysfunction in Diabetes.* Cell Metab, 2020. **31**(5): p. 1017-1031.e4.

12. MacDonald, M.J., *Differences between mouse and rat pancreatic islets: succinate responsiveness, malic enzyme, and anaplerosis.* Am J Physiol Endocrinol Metab, 2002. **283**(2): p. E302-10.

13. Benninger, R.K.P. and V. Kravets, *The physiological role of β-cell heterogeneity in pancreatic islet function.* Nature Reviews Endocrinology, 2022. **18**(1): p. 9-22.

14. Johnston, N.R., et al., *Beta Cell Hubs Dictate Pancreatic Islet Responses to Glucose.* Cell Metab, 2016. **24**(3): p. 389-401.

15. Kono, T., et al., *Impaired Store-Operated Calcium Entry and STIM1 Loss Lead to Reduced Insulin Secretion and Increased Endoplasmic Reticulum Stress in the Diabetic β-Cell.* Diabetes, 2018. **67**(11): p. 2293-2304.

16. Lacombe, J., et al., *Vitamin K-dependent carboxylation regulates Ca(2+) flux and adaptation to metabolic stress in β cells.* Cell Rep, 2023. **42**(5): p. 112500.

17. Stafford, D.W., *The vitamin K cycle.* J Thromb Haemost, 2005. **3**(8): p. 1873-8.

18. Branon, T.C., et al., *Efficient proximity labeling in living cells and organisms with TurboID.* Nat Biotechnol, 2018. **36**(9): p. 880-887.

19. Dinchuk, J.E., et al., *Aspartyl beta -hydroxylase (Asph) and an evolutionarily conserved isoform of Asph missing the catalytic domain share exons with junctin.* J Biol Chem, 2000. **275**(50): p. 39543-54.

20. Hosur, V., et al., *Genes adapt to outsmart gene-targeting strategies in mutant mouse strains by skipping exons to reinitiate transcription and translation.* Genome Biol, 2020. **21**(1): p. 168.

21. Emrich, S.M., et al., *Omnitemporal choreographies of all five STIM/Orai and IP(3)Rs underlie the complexity of mammalian Ca(2+) signaling.* Cell Rep, 2021. **34**(9): p. 108760.

22. Martínez-Martínez, E., et al., *PKC-Mediated Orai1 Channel Phosphorylation Modulates Ca(2+) Signaling in HeLa Cells.* Cells, 2022. **11**(13).

23. Palty, R., et al., *SARAF inactivates the store operated calcium entry machinery to prevent excess calcium refilling.* Cell, 2012. **149**(2): p. 425-38.

24. Linford, A., et al., *Rab14 and its exchange factor FAM116 link endocytic recycling and adherens junction stability in migrating cells.* Dev Cell, 2012. **22**(5): p. 952-66.

25. Kutay, U., et al., *Export of importin alpha from the nucleus is mediated by a specific nuclear transport factor.* Cell, 1997. **90**(6): p. 1061-71.

26. Wang, X., et al., *Receptor-Mediated ER Export of Lipoproteins Controls Lipid Homeostasis in Mice and Humans.* Cell Metab, 2021. **33**(2): p. 350-366.e7.

27. Zhao, Y., et al., *Transmembrane protein 208: a novel ER-localized protein that regulates autophagy and ER stress.* PLoS One, 2013. **8**(5): p. e64228.

28. Osawa, T., Y. Ishii, and N.N. Noda, *Human ATG2B possesses a lipid transfer activity which is accelerated by negatively charged lipids and WIPI4.* Genes Cells, 2020. **25**(1): p. 65-70.

29. Miller, C., et al., *Defective mitochondrial translation caused by a ribosomal protein (MRPS16) mutation.* Ann Neurol, 2004. **56**(5): p. 734-8.

30. Lee, A.S., P.J. Kranzusch, and J.H. Cate, *eIF3 targets cell-proliferation messenger RNAs for translational activation or repression.* Nature, 2015. **522**(7554): p. 111-4.

31. Lee, A.S., et al., *eIF3d is an mRNA cap-binding protein that is required for specialized translation initiation.* Nature, 2016. **536**(7614): p. 96-9.

32. Rogers, G.W., Jr., et al., *Modulation of the helicase activity of eIF4A by eIF4B, eIF4H, and eIF4F.* J Biol Chem, 2001. **276**(33): p. 30914-22.

33. Haze, K., et al., *Identification of the G13 (cAMP-response-element-binding protein-related protein) gene product related to activating transcription factor 6 as a transcriptional activator of the mammalian unfolded protein response.* Biochem J, 2001. **355**(Pt 1): p. 19-28.

34. Okada, T., et al., *A serine protease inhibitor prevents endoplasmic reticulum stress-induced cleavage but not transport of the membrane-bound transcription factor ATF6.* J Biol Chem, 2003. **278**(33): p. 31024-32.

35. Kondo, S., et al., *BBF2H7, a novel transmembrane bZIP transcription factor, is a new type of endoplasmic reticulum stress transducer.* Mol Cell Biol, 2007. **27**(5): p. 1716-29.

36. Stewart-Hutchinson, P.J., et al., *Structural requirements for the assembly of LINC complexes and their function in cellular mechanical stiffness.* Exp Cell Res, 2008. **314**(8): p. 1892-905.

37. King, M.C., *Dynamic regulation of LINC complex composition and function across tissues and contexts.* FEBS Lett, 2023. **597**(22): p. 2823-2832.

38. Parry, D.A., et al., *Heterozygous lamin B1 and lamin B2 variants cause primary microcephaly and define a novel laminopathy.* Genet Med, 2021. **23**(2): p. 408-414.

39. Pan, D., et al., *The integral inner nuclear membrane protein MAN1 physically interacts with the R-Smad proteins to repress signaling by the transforming growth factor-{beta} superfamily of cytokines.* J Biol Chem, 2005. **280**(16): p. 15992-6001.

40. Zhou, B., et al., *Notch signaling pathway: architecture, disease, and therapeutics.* Signal Transduction and Targeted Therapy, 2022. **7**(1): p. 95.

41. Hegde, R.S., *The Function, Structure, and Origins of the ER Membrane Protein Complex.* Annu Rev Biochem, 2022. **91**: p. 651-678.

42. *Single-cell transcriptomics of 20 mouse organs creates a Tabula Muris.* Nature, 2018. **562**(7727): p. 367-372.

43. Dinchuk, J.E., et al., *Absence of post-translational aspartyl beta-hydroxylation of epidermal growth factor domains in mice leads to developmental defects and an increased incidence of intestinal neoplasia.* J Biol Chem, 2002. **277**(15): p. 12970-7.

44. Luciani, D.S., S. Misler, and K.S. Polonsky, *Ca2+ controls slow NAD(P)H oscillations in glucose-stimulated mouse pancreatic islets.* J Physiol, 2006. **572**(Pt 2): p. 379-92.

45. Merrins, M.J., et al., *Phase Analysis of Metabolic Oscillations and Membrane Potential in Pancreatic Islet β-Cells.* Biophys J, 2016. **110**(3): p. 691-699.

46. Taylor, C.W. and S.C. Tovey, *IP(3) receptors: toward understanding their activation.* Cold Spring Harb Perspect Biol, 2010. **2**(12): p. a004010.

47. Prakriya, M. and R.S. Lewis, *Store-Operated Calcium Channels.* Physiol Rev, 2015. **95**(4): p. 1383-436.

48. Stenflo, J., et al., *Hydroxylation of aspartic acid in domains homologous to the epidermal growth factor precursor is catalyzed by a 2-oxoglutarate-dependent dioxygenase.* Proc Natl Acad Sci U S A, 1989. **86**(2): p. 444-7.

49. Bartolome, A., et al., *Notch signaling dynamically regulates adult β cell proliferation and maturity.* J Clin Invest, 2019. **129**(1): p. 268-280.

50. Dror, V., et al., *Notch signalling suppresses apoptosis in adult human and mouse pancreatic islet cells.* Diabetologia, 2007. **50**(12): p. 2504-15.

51. Song, S., et al., *Notch enhances Ca(2+) entry by activating calcium-sensing receptors and inhibiting voltage-gated K(+) channels.* Am J Physiol Cell Physiol, 2020. **318**(5): p. C954-c968.

52. Speier, S., et al., *Cx36-mediated coupling reduces beta-cell heterogeneity, confines the stimulating glucose concentration range, and affects insulin release kinetics.* Diabetes, 2007. **56**(4): p. 1078-86.

53. Bergeron, J.J., et al., *Calnexin: a membrane-bound chaperone of the endoplasmic reticulum.* Trends Biochem Sci, 1994. **19**(3): p. 124-8.

54. Kozlov, G. and K. Gehring, *Calnexin cycle - structural features of the ER chaperone system.* Febs j, 2020. **287**(20): p. 4322-4340.

55. Sehgal, P., et al., *Inhibition of the sarco/endoplasmic reticulum (ER) Ca(2+)-ATPase by thapsigargin analogs induces cell death via ER Ca(2+) depletion and the unfolded protein response.* J Biol Chem, 2017. **292**(48): p. 19656-19673.

56. Denmeade, S.R. and J.T. Isaacs, *The SERCA pump as a therapeutic target: making a "smart bomb" for prostate cancer.* Cancer Biol Ther, 2005. **4**(1): p. 14-22.

57. Read, A. and M. Schröder, *The Unfolded Protein Response: An Overview.* Biology (Basel), 2021. **10**(5).

58. English, A.R. and G.K. Voeltz, *Endoplasmic reticulum structure and interconnections with other organelles.* Cold Spring Harb Perspect Biol, 2013. **5**(4): p. a013227.

59. Degechisa, S.T., Y.T. Dabi, and S.T. Gizaw, *The mitochondrial associated endoplasmic reticulum membranes: A platform for the pathogenesis of inflammation-mediated metabolic diseases.* Immun Inflamm Dis, 2022. **10**(7): p. e647.

60. Lacombe, J., et al., *VKOR paralog VKORC1L1 supports vitamin K-dependent protein carboxylation in vivo.* JCI Insight, 2018. **3**(1).

61. Schindelin, J., et al., *Fiji: an open-source platform for biological-image analysis.* Nat Methods, 2012. **9**(7): p. 676-82.

62. Yu, V., et al., *Differential CpG methylation at Nnat in the early establishment of beta cell heterogeneity.* Diabetologia, 2024. **67**(6): p. 1079-1094.

63. Couzens, A.L., et al., *Protein interaction network of the mammalian Hippo pathway reveals mechanisms of kinase-phosphatase interactions.* Sci Signal, 2013. **6**(302): p. rs15.

64. Chambers, M.C., et al., *A cross-platform toolkit for mass spectrometry and proteomics.* Nat Biotechnol, 2012. **30**(10): p. 918-20.

65. Yu, F., S.E. Haynes, and A.I. Nesvizhskii, *IonQuant Enables Accurate and Sensitive Label-Free Quantification With FDR-Controlled Match-Between-Runs.* Mol Cell Proteomics, 2021. **20**: p. 100077.

66. UniProt, C., *UniProt: the Universal Protein Knowledgebase in 2023.* Nucleic Acids Res, 2023. **51**(D1): p. D523-D531.

67. Frankenfield, A.M., et al., *Protein Contaminants Matter: Building Universal Protein Contaminant Libraries for DDA and DIA Proteomics.* J Proteome Res, 2022. **21**(9): p. 2104-2113.

68. Suzuki, R. and H. Shimodaira, *Pvclust: an R package for assessing the uncertainty in hierarchical clustering.* Bioinformatics, 2006. **22**(12): p. 1540-2.

69. Teo, G., et al., *SAINTq: Scoring protein-protein interactions in affinity purification - mass spectrometry experiments with fragment or peptide intensity data.* Proteomics, 2016. **16**(15-16): p. 2238-45.

Chapter 4. Discussion and conclusions

4.1. ERGP is a gamma-carboxylated protein found in beta-cells which may partially mediate the protective effect of vitamin K against diabetes

This study represents the first descriptions of the potential molecular mechanisms underlying the protective effect of vitamin K against diabetes. We discovered the beta cells of the pancreatic islets highly expressed the vitamin K cycle enzymes GGCX and VKORC1 and, through our pan-specific anti-Gla antibody and beta cell specific GGCX knockout mouse model (*Ggcx^{ff};Ins1-Cre*), confirmed the presence of Gla proteins in beta cells. The *Ggcx^{ff};Ins1-Cre* mouse model, in particular, displayed fasting hyperinsulinemia and insulin resistance following a one week high fat diet, suggesting that gamma-carboxylation is important for beta cell adaptation to metabolic challenges. Also included in this study, was a mouse model with GGCX specifically knocked out of the entire pancreas (*Ggcx^{ff};Pdx1-Cre*), which displayed an even more severe phenotype where ER stress induced beta cell apoptosis caused a 50% reduction in beta cell mass by six months of age on a normal chow diet. This suggests that vitamin K plays a role in other pancreatic cell types to promote the survival of beta cells.

The use of conditional knockouts for GGCX is necessary to study its function outside of blood coagulation, as mice with global GGCX knockout will rapidly die of hemorrhage with 50% dying as embryos between E9 and E18.5 and the rest dying shortly after birth [183]. Up until the 1970s, with the discovery of osteocalcin, vitamin K-dependent gamma-carboxylation was not known to have a function outside of blood coagulation [184]. Since then several more Gla proteins have been discovered including matrix Gla protein [70], Gas6 which is involved in cell-cell communication via the TAM receptors and may play a role in cancer and immune cell signaling and insulin resistance [28, 185-187], and PRRG1-4 whose functions remain undefined

[188]. Of these proteins, none had previously been shown to be expressed in beta cells. Furthermore, Western blotting of islet extracts with our anti-Gla antibody showed more protein bands than number of known Gla proteins (disappearance of these bands following pancreas specific GGCX knockout confirmed they were not non-specific artifact bands). Therefore, we hypothesized that there must exist previously uncharacterized Gla proteins which are expressed in the beta cells, leading to the discovery of ERGP as a vitamin K dependent gamma-carboxylated protein expressed in the beta cells.

4.2. ERGP is a novel gamma-carboxylated protein

ERGP was initially identified as a novel gamma-carboxylated protein alongside ASPH in the context of another project from liver extracts. The anti-Gla antibody was used to pull down Gla proteins which were subsequently identified via liquid chromatography tandem mass spectrometry (LC-MS/MS). Subsequent immunoprecipitation of Gla proteins from mouse islet extracts determined that ERGP was the primary gamma-carboxylated form of *Asph* expressed in the pancreatic islets. The Gla residues in both ERGP and ASPH were found to be localized to their shared Glu-rich domain (GRD) containing 39 glutamic acid residues. The GRD is poorly conserved between species with only 54% identity shared between the mouse and human GRD. Interestingly, the portions of the GRD that are the best conserved are the N and C-terminal extremities where the majority of the Gla residues were identified. Deletion of the putative EF-hand domain or serine rich cytosolic tail of ASPH did not affect the carboxylation of ASPH while deletion or mutation of the Glu residues on either the N and C-terminal extremities of the GRD reduced the carboxylation of ERGP by around 50% in each case as seen by immunoprecipitation with anti-Gla. This evidence suggests that there may exist non-canonical GGCX recognition sequences in the N and C-terminal regions of the GRD.

ERGP and ASPH may also represent vitamin K dependent proteins with evolutionarily ancient functions than the blood clotting factors. Homologues of the vitamin K cycle proteins GGCX and VKORC1 are found in numerous animal species lacking blood coagulation; such as, *Drosophila* and *Placozoa* [189, 190]. However, these species do possess homologues of ASPH and ERGP [190, 191]. As mentioned previously, the GRD is poorly conserved between species and is often similar only in that the domain is a the C-terminal ER luminal domain, contains a high number of glutamic acid residues, and is predicted to have a disorganized folding structure. Our group has also identified several other ER resident novel gamma-carboxylated proteins. Work is ongoing in the characterization of the role of gamma-carboxylation in the function of these proteins.

4.3. ERGP may buffer calcium in the ER

Inputting the amino acid sequence of both human and mouse ERGP into alpha fold [192] reveals that the GRD is predicted to be disorganized. However, the presence of Gla residues and calcium ions is not considered in this prediction, both of which may endow more organized structures to the GRD. Appropriate calcium ion concentration in the ER lumen is known to be essential for the folding of numerous secreted proteins [122-125, 193] and ERGP may be no different. Previously, it was determined that junctate, the *Asph* isoform expressed from promoter 2 which lacks the serine rich cytosolic tail but contains the GRD, binds around 21mol of calcium ion per 1mol of protein [194]. The radioactive calcium overlay assays described in this study found that carboxylated ERGP bound roughly twice as much calcium as non-carboxylated ERGP, meaning that 1 carboxylated ERGP molecule may bind as many as 42 calcium ions. However, the effect of carboxylation on the kinetics of calcium ion binding was not directly

studied. Calcium-binding proteins play a myriad of roles in the cell, ranging from signaling and protein folding to extracellular matrix formation [67, 195-197].

Calcium-binding proteins can also serve to buffer calcium in the cell, with BiP, calreticulin, and calsequestrin all known to buffer calcium in the ER, helping to maintaining the free calcium ion concentration at around 200μM while the total calcium ion concentration is around 1mM [198]. BiP has been shown to bind 1-2mol of calcium ion [199] while calreticulin binds 25mol [200] and calsequestrin binds up to 80mol of calcium ions per mol of protein [201]. This study found that free ER calcium ion concentration is decreased in cells expressing non-carboxylated ERGP and even further decreased in cell with carboxylated ERGP, as shown by experiments with the ER specific fluorescent calcium probe D4ER. This suggests that ERGP may play an important role in directly buffering calcium within the ER lumen.

4.4. ERGP's role in SOCE regulation is dependent on gamma-carboxylation

Previous studies have suggested that junctate is a positive regulator of SOCE [168, 169], leading us to initially hypothesize that ERGP may be a positive regular of SOCE as well. However, there was no significant difference in the SOCE response of HEK293 cells following overexpression of ERGP. Knocking out ERGP from HEK293 cells using CRISPR/Cas9 still, by itself, did not produce a significant difference in the SOCE response. Only when vitamin K was added to the cell culture media after rescuing the expression of ERGP, resulting in the gamma-carboxylation of ERGP, did we discover that carboxylated ERGP was in fact a negative regulator of SOCE. In addition to negatively regulating SOCE, it was also discovered that carboxylated

ERGP also decreases basal cytosolic calcium levels and thapsigargin triggered ER calcium efflux.

This may be caused by carboxylated ERGP's role in regulating both STIM1 and STIM2. The SOCE complex protein STIM1 is primarily responsible for triggering the large influx of calcium traditionally associated with SOCE following acute depletion of ER calcium stores, as is seen following thapsigargin treatment or opening of the IP_3 receptors [148, 158, 202]. STIM2, on the other hand, does not play a significant role in SOCE following acute ER calcium store depletion, with the thapsigargin triggered SOCE response largely unaltered following knockout of STIM2 [152]. Instead, STIM2 has been shown to regulate basal cytosolic and ER calcium levels by triggering smaller SOCE influx following more minor decreases in ER calcium concentration. An siRNA screen of the human proteome found STIM2 to be the strongest positive regulator of basal cytosolic calcium concentration [154]. The TurboID screen detailed in chapter 3 identified both STIM1 and STIM2 as potential interactors of ERGP whose interactions with ERGP increase following depletion of ER calcium stores with thapsigargin. Western blotting for STIM1 after streptavidin of proteins biotinylated by ERGP-mT showed increased biotinylated STIM1 following treatment with thapsigargin (Figure 1). It is also possible that ERGP decreases ER free calcium stores by binding to and sequestering calcium within the ER.

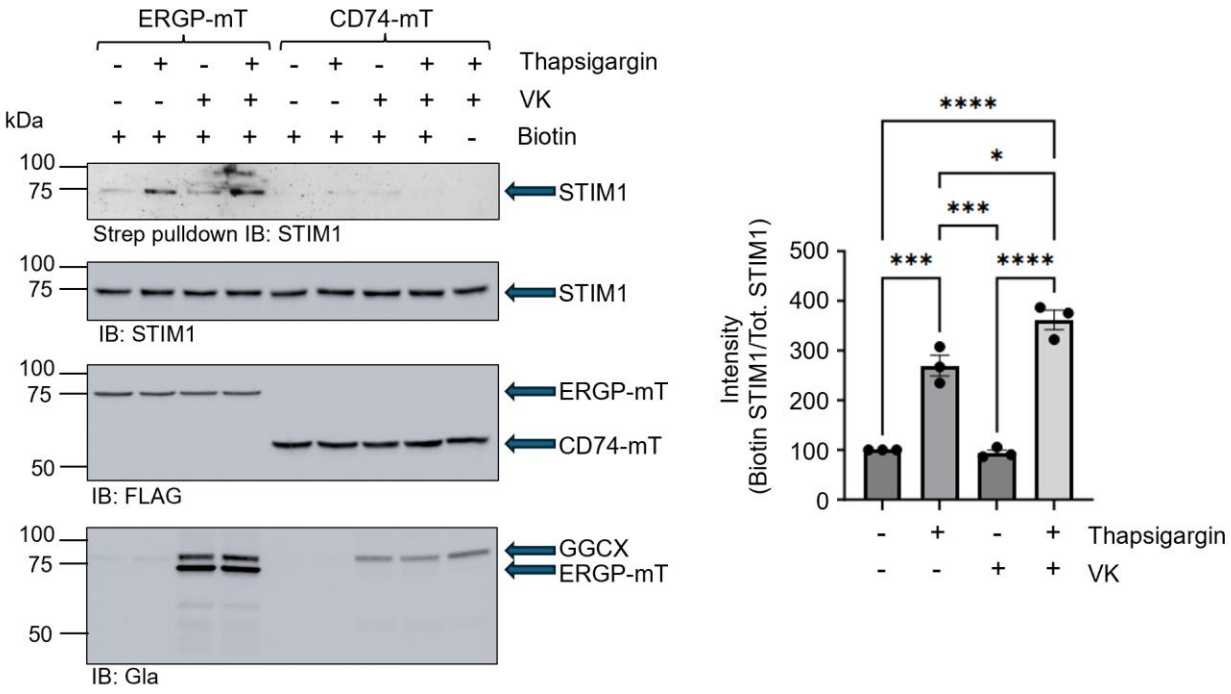

Figure 1. (left) Western blot depicting STIM1 biotinylated by ERGP-mT in the presence or absence of thapsigargin. Cells expressing ERGP-mT and transiently transfected with GGCX and VKORC1 and cultured in the presence or absence of vitamin K (22μM) overnight. Cells were then treated with biotin (50μM) and thapsigargin (1μM) or just biotin for 15 minutes before lysis and analysis. (right) Quantification of biotinylated STIM1 normalized to total STIM1 from the input (n=3). * $p < 0.05$, *** $p < 0.001$, **** $p < 0.0001$

Previous studies on ERGP (then called humbug) were likely unable to uncover its function in SOCE regulation possibly owing to the lack of vitamin K supplementation of the cell culture media. ERGP is expressed in many cell lines commonly used to study cellular calcium flux; such as, HEK293 cells, Hela cells, and Jurkat T cells [203]. However, the lack of vitamin K in the culture medium and serum means that ERGP is seldom if ever carboxylated in these other studies. Addition of vitamin K into the media of these cell cultures may be important for the

study of calcium flux in these cell systems to ensure the proper functioning of ERGP and a more accurate reflection of physiological ER calcium store dynamics.

4.5. Gamma-carboxylation in beta cells is required for coordinated islet calcium oscillations

Islets taken from *Ggcx^{ff};Ins1-Cre* mice had increased periods of whole islet calcium oscillation and a loss of coordination in the oscillatory patterns of individual islet cells. Previous studies have shown that knockout or pharmacological inactivation of SOCE in pancreatic islets increases the period and decreases the amplitude of whole islet calcium oscillations. Importantly, this change in oscillation was accompanied by a decrease in ex vivo glucose stimulated insulin secretion [142]. Semi-dispersed islets taken from *Ggcx^{ff};Ins1-Cre* mice were seen to have elevated SOCE. Despite this, islets taken from *Ggcx^{ff};Ins1-Cre* mice had an increased period of islet calcium oscillations. This suggests that the changes in islet oscillation and islet cell coordination seen in the from *Ggcx^{ff};Ins1-Cre* islets are not solely driven by ERGP's effect on SOCE.

Calcium waves propagate across the islet via the connexin-36 gap junctions [101]. The TurboID screens showed some evidence that connexin-43, the gap junction expressed in HEK293 cells, is an interactor of ERGP. However, it is not known whether or not connexin-36 interacts with ERGP. As gap junctions are expressed on the plasma membrane, it is unlikely that ERGP, an ER resident protein has a direct effect on the functioning of individual gap junctions themselves. Rather, ERGP may be involved in the expression, trafficking, or localization of gap junctions. Cell-cell signaling via the Slit-Robo pathway has also been shown to be essential for the coordination of islet calcium oscillations [204]. Strikingly, SLIT2 was identified as an

interactor of ERGP. SLIT2 is also a substrate of ASPH. Follow up studies are necessary to elucidate the precise mechanism by which ERGP regulates islet calcium oscillations.

4.6. ERGP may regulate ER calcium homeostasis and play a role in cell-cell signaling and the unfolded protein response (UPR)

Through the use of TurboID, numerous potential interactors of ERGP were identified. All three of the IP_3 receptors (ITPR1, ITPR2, and ITPR3) were identified as an interactor of ERGP in every screen. Of note, the interaction of ITPR1 with ERGP was decreased in the presence of thapsigargin while the interaction of STIM1 and STIM2 with ERGP was increased in the presence of thapsigargin. The functions of the IP_3 receptors and STIM proteins are diametrically opposed with ITPR1 involved in the efflux of calcium out of the ER and the STIM1 and STIM2 involved in the influx of calcium into the ER [144, 152]. Following depletion of the ER calcium stores, ERGP seems to switch between interacting with the IP_3 receptors and STIM proteins. While we have established that carboxylated ERGP is a negative regulator of SOCE, the effect of ERGP's interaction with ITPR1 and the role that the carboxylation of ERGP plays in IP_3 receptor function remains unknown.

The potential interactors of ERGP include proteins involved in cell-cell signaling; such as, NOTCH2, JAG2, and SLIT2. As previously described, Slit-robo signaling is essential for coordinated whole islet calcium oscillations [204]. While the Notch proteins are not expressed in a very high percentage of beta cells (~2-7%) [205], it is known that Notch signaling is essential for triggering proliferation and suppressing apoptosis in beta cells [117, 206]. ERGP most likely interacts with these proteins through its interaction with ASPH, which beta hydroxylates the

calcium binding EGF-like (EGF-like) domain present on NOTCH2 and SLIT2. ASPH was identified as an interactor of ERGP through the TurboID screen as well. The effect of ERGP's interaction with ASPH remains unknown. Recently, it has been proposed that ASPH serves to signal improperly folded EGF-like domains. This is evidenced through ASPH's increased affinity for EGF-like domains containing non-canonical disulfide bridges—a sign of misfolding [175]. If this is the case and ASPH is ultimately important for folding of these proteins, ERGP may aid in the folding of these domains by buffering calcium near where these proteins are being folded and maintaining appropriate ER calcium concentrations.

In fact, EGF-like domain containing proteins represented a significant class of proteins identified by the TurboID screens as significant interactors of ERGP. Another notable potential interactor of ERGP identified was ATF6. ATF6 is a classical regulator of the unfolded protein response (UPR) [207, 208], further linking ERGP to protein folding within the ER. In addition to ATF6, the UPR protein CREB3L2 was also identified as a significant interactor of ERGP. Thapsigargin treatment significantly increased the interaction of CREB3L2 with ERGP. Bear in mind, the duration of thapsigargin treatment and/or biotinylation of potential interactors was only 15 minutes. This was done to prevent ER stress and avoid significant activation of the UPR. Should the duration of thapsigargin treatment have been extended, more UPR protein interactors of ERGP may have been identified. Several classical ER chaperones, such as BiP, calnexin, and calreticulin, were identified in the ERGP TurboID screens, but were not considered significant interactors due to their identification in the CD74 TurboID screens as well.

4.7. Future directions: validation of the potential interaction between the IP_3 receptors and ERGP and its impact on the incretin effect of glucagon like peptide 1 (GLP-1)

The potential interaction between the IP_3 receptors and ERGP is one of the most interesting identified in the TurboID screens. Should these interaction be confirmed, it would provide evidence that ERGP regulates both the influx of calcium into the ER via SOCE as well as the efflux of calcium out of the ER via the IP_3 receptors. The IP_3 receptors also play an important role in beta cells, serving as one of the downstream signaling pathways triggered by the incretin glucagon like peptide 1 (GLP-1) [209]. While the Gs-coupled cAMP pathway is the primary mediator of GLP-1's effect in healthy animals, a recent study found that in islets taken from obese mice or exposed to chronic high glucose conditions (16.7mM glucose) ex vivo, the Gq coupled IP_3 receptor pathway is necessary for the incretin effect of GLP-1 [146]. These findings could partially explain why significant fasting hyperinsulinemia and hyperglycemia is not seen in from *Ggcx^{ff};Ins1-Cre* mice unless they are fed a high fat diet. High fat diets, which are known to drive insulin resistance, may elevate blood glucose persistently enough to cause a Gs to Gq switch in beta cell GLP-1 signaling, revealing a phenotype potentially mediated by ERGP's inability to properly regulate the IP_3 receptors.

The effect of carboxylated ERGP on IP_3 receptor signaling will be determined via calcium imaging of HEK293 cells in the presence or absence of ERGP, vitamin K, and/or carbachol, an IP_3 receptor agonist [210]. The effect of carboxylation on GLP-1 signaling can also be determined using the *Ggcx^{ff};Ins1-Cre* mice. These mice could be fed a high fat or chow diet then treated with GLP-1 before their glucose stimulated insulin secretion is assessed. The effect of carboxylation on GLP-1 signaling could also be examined ex vivo after the islets are cultured in either high (16.7mM) or low (5.5mM) glucose conditions. These experiments can also be done

on the newly created beta cell specific ERGP knockout mouse line to directly determine the effect of ERGP on GLP-1 signaling.

4.8. Future directions: beta cell specific knockout of ERGP to directly study its effect on beta cell functioning

The *Ggcx*^{ff}*;Ins1-Cre* mice served as an animal model lacking functional ERGP in their beta cells. However, additional previously unknown Gla proteins have since been discovered to be expressed in beta cells (Lacombe et al. unpublished data). To eliminate potential confounding effects from these other Gla proteins, a beta cell specific knockout of ERGP has been generated. The *Asph* gene locus is complex and encodes many protein isoforms; including, ASPH, ERGP, junctate, and junctin. Following the failure of the *Asph*$^{LacZ/LacZ}$ gene trap to completely knock out ERGP, we shifted our approach to targeting *Asph* exon 17, the final exon of ERGP which is the only exon it does not have in common with ASPH. *Asph* exon 17 encodes the last two amino acids of ERGP and contains the polyA signal. ERGP shares this exon with junctate, which was confirmed to not be expressed in beta cells. CRISPR/Cas9 was used to introduce loxP sites flanking the 5' and 3' intronic regions just up and downstream of *Asph* exon 17 (*ERGP*^{ff}). These mice were then crossed with mice expressing Cre recombinase driven by the *Ins1* gene promoter (*Ins1-Cre*), resulting in a mouse line with ERGP knocked out of the beta cells (*ERGP*^{ff}*;Ins1-Cre*) (Figure 2).

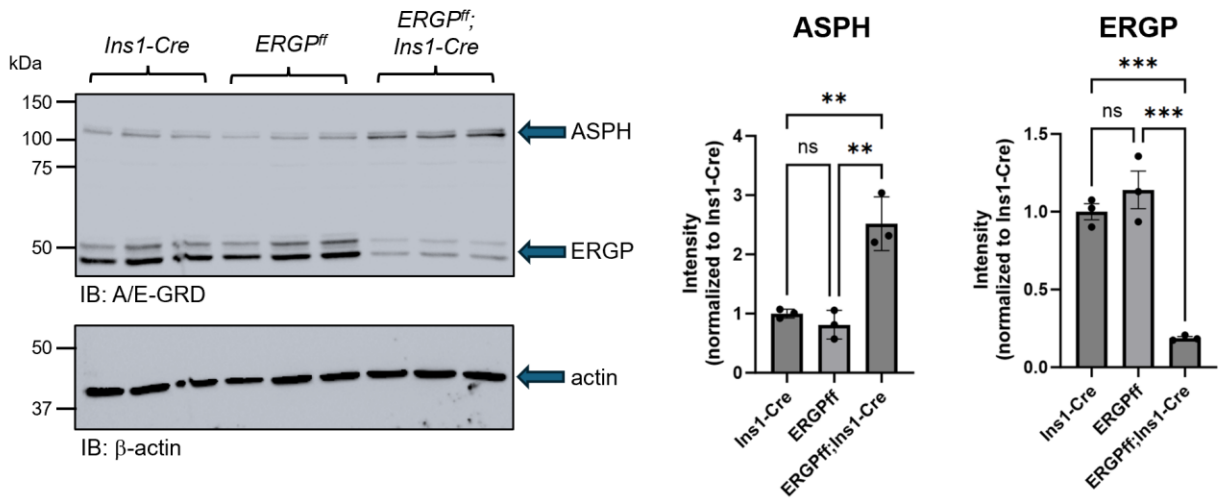

Figure 2. (left) Western blot of islet extracts taken from *Ins1-Cre*, *ERGP^{ff},* and *ERGP^{ff};Ins1-Cre* mice. (right) Quantification of bands corresponding to ASPH and ERGP normalized to actin expressed as fold change of *Ins1-Cre*

The residual ERGP seen on the Western blot of islet extracts taken from *ERGP^{ff};Ins1-Cre* mice most likely represent ERGP expressed in other islet endocrine cells; such as, alpha and delta cells. A potential pitfall of the *ERGP^{ff};Ins1-Cre* mouse model is their elevated expression of ASPH. While the N-terminal non-enzymatic regions of ASPH are nearly identical to ERGP, it is not known whether or not ASPH can compensate for any of the functions of ERGP. Metabolic tests will be utilized to determine the glucose tolerance, glucose stimulated insulin secretion, and insulin tolerance of the *ERGP^{ff};Ins1-Cre* mice fed either a high fat or chow diet. Islets from these mice will also be used to directly examine the effect of beta cell specific ERGP knockout on the coordination of whole islet calcium oscillations. These mice will also be used to directly determine the role of ERGP on GLP-1 signaling as described above.

4.9. Concluding remarks

The discovery of ERGP as a novel gamma-carboxylated protein expressed in beta cells helps explain the beneficial effect of vitamin K in protecting against diabetes. However, the beta cells are not the only cell type that expresses this protein. ERGP is expressed in tissues ranging from the liver to hypothalamic cells [211], suggesting that the findings detailed in this study could have further reaching implications. Moreover, this study focused on ERGP and did not examine the effect of gamma-carboxylation on ASPH, which is also gamma-carboxylated [212]. ERGP also represents the first of what may be a family of non-secreted ER resident Gla proteins. Preliminary data suggests that many of these proteins may be involved in folding of secretory proteins, functions that no previously known Gla proteins had.

These findings expand the previously established roles of vitamin K to include the regulation of insulin secretion and beta-cell signaling and may help in the development of vitamin K based treatments against diabetes, expanding our understanding of the relationship between nutrition and beta cell function. The discovery of ERGP may also shed light on the ancestral role of vitamin K in the regulation of cellular calcium through the gamma-carboxylation of proteins like ERGP. Furthermore, ERGP and its enzymatically active isoform ASPH are expressed in many other tissues as well; including, immune cells, nervous cells, and muscular cells [211]. If gamma-carboxylation is essential for the function of ERGP in these cells as well, vitamin K may have much further reaching functions in the body than previously thought.

ix. Reference list

1. Feather, A.R., D; Waterhouse, M, *Kumar and Clark's Clinical Medicine*. 10 ed. 2021: Elsevier.
2. Clinic, T.M. *Diabetes: Diagnosis & Treatment*. 2024; Available from: https://www.mayoclinic.org/diseases-conditions/diabetes/diagnosis-treatment/drc-20371451.
3. Federation, I.D., *IDF Diabetes Atlas*. 2021, International Diabetes Federation: Brussels, Belgium.
4. *Prediabetes - Your Chance to Prevent Type 2 Diabetes*. 2022.
5. Rother, K.I., *Diabetes treatment--bridging the divide.* N Engl J Med, 2007. **356**(15): p. 1499-501.
6. Dhatariya, K.K., et al., *Diabetic ketoacidosis.* Nat Rev Dis Primers, 2020. **6**(1): p. 40.
7. Martin, B.C., et al., *Role of glucose and insulin resistance in development of type 2 diabetes mellitus: results of a 25-year follow-up study.* Lancet, 1992. **340**(8825): p. 925-9.
8. Johnson, J.D., *On the causal relationships between hyperinsulinaemia, insulin resistance, obesity and dysglycaemia in type 2 diabetes.* Diabetologia, 2021. **64**(10): p. 2138-2146.
9. Prentki, M., et al., *Malonyl-CoA signaling, lipid partitioning, and glucolipotoxicity: role in beta-cell adaptation and failure in the etiology of diabetes.* Diabetes, 2002. **51 Suppl 3**: p. S405-13.
10. Poitout, V. and R.P. Robertson, *Minireview: Secondary beta-cell failure in type 2 diabetes--a convergence of glucotoxicity and lipotoxicity.* Endocrinology, 2002. **143**(2): p. 339-42.

11. Carrillo-Larco, R.M., et al., *Mean age and body mass index at type 2 diabetes diagnosis: Pooled analysis of 56 health surveys across income groups and world regions.* Diabet Med, 2024. **41**(2): p. e15174.

12. Modzelewski, R., et al., *Gestational Diabetes Mellitus-Recent Literature Review.* J Clin Med, 2022. **11**(19).

13. Urakami, T., *Maturity-onset diabetes of the young (MODY): current perspectives on diagnosis and treatment.* Diabetes Metab Syndr Obes, 2019. **12**: p. 1047-1056.

14. Nishi, M. and K. Nanjo, *Insulin gene mutations and diabetes.* J Diabetes Investig, 2011. **2**(2): p. 92-100.

15. Doan, L.V. and L.D. Madison, *Cystic Fibrosis–Related Diabetes*, in *StatPearls*. 2024, StatPearls Publishing

16. O'Gara, P.T., et al., *2013 ACCF/AHA guideline for the management of ST-elevation myocardial infarction: a report of the American College of Cardiology Foundation/American Heart Association Task Force on Practice Guidelines.* Circulation, 2013. **127**(4): p. e362-425.

17. Feldman, E.L., et al., *Diabetic neuropathy.* Nat Rev Dis Primers, 2019. **5**(1): p. 41.

18. Grisanti, L.A., *Diabetes and Arrhythmias: Pathophysiology, Mechanisms and Therapeutic Outcomes.* Front Physiol, 2018. **9**: p. 1669.

19. Thomas, M.C., et al., *Diabetic kidney disease.* Nat Rev Dis Primers, 2015. **1**: p. 15018.

20. Shukla, U.V. and K. Tripathy, *Diabetic Retinopathy*, in *StatPearls*. 2024, StatPearls Publishing

21. Karamanou, M., et al., *Milestones in the history of diabetes mellitus: The main contributors.* World J Diabetes, 2016. **7**(1): p. 1-7.

22. Lee, J. and P.F. Pilch, *The insulin receptor: structure, function, and signaling.* Am J Physiol, 1994. **266**(2 Pt 1): p. C319-34.

23. Han, H.S., et al., *Regulation of glucose metabolism from a liver-centric perspective.* Exp Mol Med, 2016. **48**(3): p. e218.

24. Dimitriadis, G., et al., *Insulin effects in muscle and adipose tissue.* Diabetes Res Clin Pract, 2011. **93 Suppl 1**: p. S52-9.

25. De la Cruz-Concepción, B., et al., *Insulin: A connection between pancreatic β cells and the hypothalamus.* World J Diabetes, 2023. **14**(2): p. 76-91.

26. Zhang, Z., H. Liu, and J. Liu, *Akt activation: A potential strategy to ameliorate insulin resistance.* Diabetes Res Clin Pract, 2019. **156**: p. 107092.

27. Conejo, R. and M. Lorenzo, *Insulin signaling leading to proliferation, survival, and membrane ruffling in C2C12 myoblasts.* J Cell Physiol, 2001. **187**(1): p. 96-108.

28. Schott, C., et al., *GAS6 and AXL Promote Insulin Resistance by Rewiring Insulin Signaling and Increasing Insulin Receptor Trafficking to Endosomes.* Diabetes, 2024. **73**(10): p. 1648-1661.

29. Yoon, M.S., *The Role of Mammalian Target of Rapamycin (mTOR) in Insulin Signaling.* Nutrients, 2017. **9**(11).

30. Muoio, D.M. and C.B. Newgard, *Mechanisms of disease:Molecular and metabolic mechanisms of insulin resistance and beta-cell failure in type 2 diabetes.* Nat Rev Mol Cell Biol, 2008. **9**(3): p. 193-205.

31. Leahy, J.L., *Pathogenesis of type 2 diabetes mellitus.* Arch Med Res, 2005. **36**(3): p. 197-209.

32. Roduit, R., et al., *A role for the malonyl-CoA/long-chain acyl-CoA pathway of lipid signaling in the regulation of insulin secretion in response to both fuel and nonfuel stimuli.* Diabetes, 2004. **53**(4): p. 1007-19.

33. Meglasson, M.D. and F.M. Matschinsky, *Pancreatic islet glucose metabolism and regulation of insulin secretion.* Diabetes Metab Rev, 1986. **2**(3-4): p. 163-214.

34. Wicksteed, B., et al., *Glucose-induced translational control of proinsulin biosynthesis is proportional to preproinsulin mRNA levels in islet beta-cells but not regulated via a positive feedback of secreted insulin.* J Biol Chem, 2003. **278**(43): p. 42080-90.

35. Prentki, M. and C.J. Nolan, *Islet beta cell failure in type 2 diabetes.* J Clin Invest, 2006. **116**(7): p. 1802-12.

36. Butler, A.E., et al., *Beta-cell deficit and increased beta-cell apoptosis in humans with type 2 diabetes.* Diabetes, 2003. **52**(1): p. 102-10.

37. Lacombe, J. and M. Ferron, *Vitamin K-dependent carboxylation in β-cells and diabetes.* Trends Endocrinol Metab, 2024.

38. Templeman, N.M., et al., *A causal role for hyperinsulinemia in obesity.* J Endocrinol, 2017. **232**(3): p. R173-r183.

39. Templeman, N.M., S.M. Clee, and J.D. Johnson, *Suppression of hyperinsulinaemia in growing female mice provides long-term protection against obesity.* Diabetologia, 2015. **58**(10): p. 2392-402.

40. Solis-Herrera, C., et al., *Pathogenesis of Type 2 Diabetes Mellitus*, in *Endotext*, K.R. Feingold, et al., Editors. 2000, MDText.com, Inc.

41. Tillil, H. and J. Köbberling, *Age-corrected empirical genetic risk estimates for first-degree relatives of IDDM patients.* Diabetes, 1987. **36**(1): p. 93-9.

42. Ali, O., *Genetics of type 2 diabetes.* World J Diabetes, 2013. **4**(4): p. 114-23.

43. Kaprio, J., et al., *Concordance for type 1 (insulin-dependent) and type 2 (non-insulin-dependent) diabetes mellitus in a population-based cohort of twins in Finland.* Diabetologia, 1992. **35**(11): p. 1060-7.

44. Isler, O., et al., *[Constitutional specific effect of vitamin K1 and its analogs against coumarin compounds].* Hoppe Seylers Z Physiol Chem, 1953. **295**: p. 290-309.

45. Halder, M., et al., *Vitamin K: Double Bonds beyond Coagulation Insights into Differences between Vitamin K1 and K2 in Health and Disease.* Int J Mol Sci, 2019. **20**(4).

46. Koitaya, N., et al., *Low-dose vitamin K2 (MK-4) supplementation for 12 months improves bone metabolism and prevents forearm bone loss in postmenopausal Japanese women.* J Bone Miner Metab, 2014. **32**(2): p. 142-50.

47. Schurgers, L.J., et al., *Vitamin K-containing dietary supplements: comparison of synthetic vitamin K1 and natto-derived menaquinone-7.* Blood, 2007. **109**(8): p. 3279-83.

48. Ichikawa, T., et al., *Steroid and xenobiotic receptor SXR mediates vitamin K2-activated transcription of extracellular matrix-related genes and collagen accumulation in osteoblastic cells.* J Biol Chem, 2006. **281**(25): p. 16927-16934.

49. Dyggve, H., *Toxic effect of menadione sodium bisulfite in premature infants.* Dan Med Bull, 1959. **6**(1): p. 19-23.

50. Stenflo, J. and J.W. Suttie, *Vitamin K-dependent formation of gamma-carboxyglutamic acid.* Annu Rev Biochem, 1977. **46**: p. 157-72.

51. Stafford, D.W., *The vitamin K cycle.* J Thromb Haemost, 2005. **3**(8): p. 1873-8.

52. Stanley, T.B., et al., *Amino acids responsible for reduced affinities of vitamin K-dependent propeptides for the carboxylase.* Biochemistry, 1999. **38**(47): p. 15681-7.

53. Bristol, J.A., et al., *Biosynthesis of prothrombin: intracellular localization of the vitamin K-dependent carboxylase and the sites of gamma-carboxylation.* Blood, 1996. **88**(7): p. 2585-93.

54. Hao, Z., et al., *Vitamin K-dependent carboxylation of coagulation factors: insights from a cell-based functional study.* Haematologica, 2020. **105**(8): p. 2164-2173.

55. Knobloch, J.E. and J.W. Suttie, *Vitamin K-dependent carboxylase. Control of enzyme activity by the "propeptide" region of factor X.* J Biol Chem, 1987. **262**(32): p. 15334-7.

56. Lacombe, J., et al., *VKOR paralog VKORC1L1 supports vitamin K-dependent protein carboxylation in vivo.* JCI Insight, 2018. **3**(1).

57. Yang, X., et al., *Regulation of VKORC1L1 is critical for p53-mediated tumor suppression through vitamin K metabolism.* Cell Metab, 2023. **35**(8): p. 1474-1490.e8.

58. Mishima, E., et al., *A non-canonical vitamin K cycle is a potent ferroptosis suppressor.* Nature, 2022. **608**(7924): p. 778-783.

59. Li, J., et al., *Novel role of vitamin k in preventing oxidative injury to developing oligodendrocytes and neurons.* J Neurosci, 2003. **23**(13): p. 5816-26.

60. Dam, H., *The antihaemorrhagic vitamin of the chick.* Biochem J, 1935. **29**(6): p. 1273-85.

61. Dam, H., F. Schønheyder, and E. Tage-Hansen, *Studies on the mode of action of vitamin K.* Biochem J, 1936. **30**(6): p. 1075-9.

62. Stenflo, J., et al., *Vitamin K dependent modifications of glutamic acid residues in prothrombin.* Proc Natl Acad Sci U S A, 1974. **71**(7): p. 2730-3.

63. Jorgensen, M.J., et al., *Recognition site directing vitamin K-dependent gamma-carboxylation resides on the propeptide of factor IX.* Cell, 1987. **48**(2): p. 185-91.

64. Esmon, C.T., et al., *Anticoagulation proteins C and S.* Adv Exp Med Biol, 1987. **214**: p. 47-54.

65. Hauschka, P.V. and M.L. Reid, *Timed appearance of a calcium-binding protein containing gamma-carboxyglutamic acid in developing chick bone.* Dev Biol, 1978. **65**(2): p. 426-34.

66. Lee, N.K., et al., *Endocrine regulation of energy metabolism by the skeleton.* Cell, 2007. **130**(3): p. 456-69.

67. Ferron, M., et al., *Osteocalcin differentially regulates beta cell and adipocyte gene expression and affects the development of metabolic diseases in wild-type mice.* Proc Natl Acad Sci U S A, 2008. **105**(13): p. 5266-70.

68. Ferron, M., et al., *Insulin signaling in osteoblasts integrates bone remodeling and energy metabolism.* Cell, 2010. **142**(2): p. 296-308.

69. Price, P.A., M.R. Urist, and Y. Otawara, *Matrix Gla protein, a new gamma-carboxyglutamic acid-containing protein which is associated with the organic matrix of bone.* Biochem Biophys Res Commun, 1983. **117**(3): p. 765-71.

70. Luo, G., et al., *Spontaneous calcification of arteries and cartilage in mice lacking matrix GLA protein.* Nature, 1997. **386**(6620): p. 78-81.

71. Munroe, P.B., et al., *Mutations in the gene encoding the human matrix Gla protein cause Keutel syndrome.* Nat Genet, 1999. **21**(1): p. 142-4.

72. *Global burden of 369 diseases and injuries in 204 countries and territories, 1990-2019: a systematic analysis for the Global Burden of Disease Study 2019.* Lancet, 2020. **396**(10258): p. 1204-1222.

73. García-Blanco, L., et al., *High consumption of ultra-processed foods is associated with increased risk of micronutrient inadequacy in children: The SENDO project.* Eur J Pediatr, 2023. **182**(8): p. 3537-3547.

74. Kaidar-Person, O., et al., *Nutritional deficiencies in morbidly obese patients: a new form of malnutrition? Part A: vitamins.* Obes Surg, 2008. **18**(7): p. 870-6.

75. Via, M., *The malnutrition of obesity: micronutrient deficiencies that promote diabetes.* ISRN Endocrinol, 2012. **2012**: p. 103472.

76. Pokharel, P., et al., *Vitamin K1 Intake and Incident Diabetes in the Danish Diet, Cancer, and Health Study.* J Clin Endocrinol Metab, 2023. **108**(11): p. e1253-e1263.

77. Pan, Y. and R.T. Jackson, *Dietary phylloquinone intakes and metabolic syndrome in US young adults.* J Am Coll Nutr, 2009. **28**(4): p. 369-79.

78. Beulens, J.W., et al., *Dietary phylloquinone and menaquinones intakes and risk of type 2 diabetes.* Diabetes Care, 2010. **33**(8): p. 1699-705.

79. Ibarrola-Jurado, N., et al., *Dietary phylloquinone intake and risk of type 2 diabetes in elderly subjects at high risk of cardiovascular disease.* Am J Clin Nutr, 2012. **96**(5): p. 1113-8.

80. Yoshida, M., et al., *Effect of vitamin K supplementation on insulin resistance in older men and women.* Diabetes Care, 2008. **31**(11): p. 2092-6.

81. Zwakenberg, S.R., et al., *Circulating Phylloquinone Concentrations and Risk of Type 2 Diabetes: A Mendelian Randomization Study.* Diabetes, 2019. **68**(1): p. 220-225.

82. Karamzad, N., et al., *Effects of MK-7 Supplementation on Glycemic Status, Anthropometric Indices and Lipid Profile in Patients with Type 2 Diabetes: A Randomized Controlled Trial.* Diabetes Metab Syndr Obes, 2020. **13**: p. 2239-2249.

83. Rahimi Sakak, F., et al., *Glycemic control improvement in individuals with type 2 diabetes with vitamin K(2) supplementation: a randomized controlled trial.* Eur J Nutr, 2021. **60**(5): p. 2495-2506.

84. Sai Varsha, M.K., et al., *Hypoglycemic action of vitamin K1 protects against early-onset diabetic nephropathy in streptozotocin-induced rats.* Nutrition, 2015. **31**(10): p. 1284-92.

85. Cheung, C.L., et al., *Treatment with direct oral anticoagulants or warfarin and the risk for incident diabetes among patients with atrial fibrillation: a population-based cohort study.* Cardiovasc Diabetol, 2021. **20**(1): p. 71.

86. Liu, X., et al., *Is the Risk of Diabetes Lower in Patients With Atrial Fibrillation Treated With Direct Oral Anticoagulant Compared to Warfarin?* Front Cardiovasc Med, 2022. **9**: p. 874795.

87. Waeber, G., et al., *Characterization of the murine high Km glucose transporter GLUT2 gene and its transcriptional regulation by glucose in a differentiated insulin-secreting cell line.* Journal of Biological Chemistry, 1994. **269**(43): p. 26912-26919.

88. Matschinsky, F.M. and D.F. Wilson, *The Central Role of Glucokinase in Glucose Homeostasis: A Perspective 50 Years After Demonstrating the Presence of the Enzyme in Islets of Langerhans.* Front Physiol, 2019. **10**: p. 148.

89. Day, P., et al., *What factors determine placental glucose transfer.* Placenta, 2013. **34**.

90. Cook, D.L. and C.N. Hales, *Intracellular ATP directly blocks K+ channels in pancreatic B-cells.* Nature, 1984. **311**(5983): p. 271-3.

91. Dunne, M.J. and O.H. Petersen, *Intracellular ADP activates K+ channels that are inhibited by ATP in an insulin-secreting cell line.* FEBS Lett, 1986. **208**(1): p. 59-62.

92. Prentki, M., *New insights into pancreatic beta-cell metabolic signaling in insulin secretion.* Eur J Endocrinol, 1996. **134**(3): p. 272-86.

93. Merrins, M.J., et al., *Metabolic cycles and signals for insulin secretion.* Cell Metab, 2022. **34**(7): p. 947-968.

94. Prentki, M., F.M. Matschinsky, and S.R. Madiraju, *Metabolic signaling in fuel-induced insulin secretion.* Cell Metab, 2013. **18**(2): p. 162-85.

95. Stark, R., et al., *Phosphoenolpyruvate cycling via mitochondrial phosphoenolpyruvate carboxykinase links anaplerosis and mitochondrial GTP with insulin secretion.* J Biol Chem, 2009. **284**(39): p. 26578-90.

96. Foster, H.R., et al., *The isoforms of pyruvate kinase act as nutrient sensors for the β-cell K_{ATP} channel.* bioRxiv, 2022: p. 2022.02.09.478817.

97. MacDonald, M.J., *Differences between mouse and rat pancreatic islets: succinate responsiveness, malic enzyme, and anaplerosis.* Am J Physiol Endocrinol Metab, 2002. **283**(2): p. E302-10.

98. Lewandowski, S.L., et al., *Pyruvate Kinase Controls Signal Strength in the Insulin Secretory Pathway.* Cell Metab, 2020. **32**(5): p. 736-750.e5.

99. Marinelli, I., et al., *Oscillations in K(ATP) conductance drive slow calcium oscillations in pancreatic β-cells.* Biophys J, 2022. **121**(8): p. 1449-1464.

100. Merrins, M.J., et al., *Phase Analysis of Metabolic Oscillations and Membrane Potential in Pancreatic Islet β-Cells.* Biophys J, 2016. **110**(3): p. 691-699.

101. Head, W.S., et al., *Connexin-36 gap junctions regulate in vivo first- and second-phase insulin secretion dynamics and glucose tolerance in the conscious mouse.* Diabetes, 2012. **61**(7): p. 1700-7.

102. Lang, D.A., et al., *Brief, irregular oscillations of basal plasma insulin and glucose concentrations in diabetic man.* Diabetes, 1981. **30**(5): p. 435-9.

103. Polonsky, K.S., et al., *Abnormal patterns of insulin secretion in non-insulin-dependent diabetes mellitus.* N Engl J Med, 1988. **318**(19): p. 1231-9.

104. Nauck, M.A. and J.J. Meier, *Incretin hormones: Their role in health and disease.* Diabetes Obes Metab, 2018. **20 Suppl 1**: p. 5-21.

105. Nolan, C.J., et al., *Beta cell compensation for insulin resistance in Zucker fatty rats: increased lipolysis and fatty acid signalling.* Diabetologia, 2006. **49**(9): p. 2120-30.

106. Corkey, B.E., *Banting lecture 2011: hyperinsulinemia: cause or consequence?* Diabetes, 2012. **61**(1): p. 4-13.

107. Ahrén, B. and J.J. Holst, *The cephalic insulin response to meal ingestion in humans is dependent on both cholinergic and noncholinergic mechanisms and is important for postprandial glycemia.* Diabetes, 2001. **50**(5): p. 1030-8.

108. Bavamian, S., et al., *Islet-cell-to-cell communication as basis for normal insulin secretion.* Diabetes Obes Metab, 2007. **9 Suppl 2**: p. 118-32.

109. Serre-Beinier, V., et al., *Cx36 preferentially connects beta-cells within pancreatic islets.* Diabetes, 2000. **49**(5): p. 727-34.

110. Bosco, D., J.A. Haefliger, and P. Meda, *Connexins: key mediators of endocrine function.* Physiol Rev, 2011. **91**(4): p. 1393-445.

111. Johnston, N.R., et al., *Beta Cell Hubs Dictate Pancreatic Islet Responses to Glucose.* Cell Metab, 2016. **24**(3): p. 389-401.

112. Farnsworth, N.L., et al., *Fluorescence recovery after photobleaching reveals regulation and distribution of connexin36 gap junction coupling within mouse islets of Langerhans.* J Physiol, 2014. **592**(20): p. 4431-46.

113. Salem, V., et al., *Leader β-cells coordinate Ca(2+) dynamics across pancreatic islets in vivo.* Nat Metab, 2019. **1**(6): p. 615-629.

114. Camunas-Soler, J., et al., *Patch-Seq Links Single-Cell Transcriptomes to Human Islet Dysfunction in Diabetes.* Cell Metab, 2020. **31**(5): p. 1017-1031.e4.

115. Rui, J., et al., *β Cells that Resist Immunological Attack Develop during Progression of Autoimmune Diabetes in NOD Mice.* Cell Metab, 2017. **25**(3): p. 727-738.

116. Lee, H., et al., *Beta Cell Dedifferentiation Induced by IRE1α Deletion Prevents Type 1 Diabetes.* Cell Metab, 2020. **31**(4): p. 822-836.e5.

117. Bartolome, A., et al., *Notch signaling dynamically regulates adult β cell proliferation and maturity.* J Clin Invest, 2019. **129**(1): p. 268-280.

118. Weir, G.C., C. Aguayo-Mazzucato, and S. Bonner-Weir, *β-cell dedifferentiation in diabetes is important, but what is it?* Islets, 2013. **5**(5): p. 233-7.

119. van der Meulen, T. and M.O. Huising, *Role of transcription factors in the transdifferentiation of pancreatic islet cells.* J Mol Endocrinol, 2015. **54**(2): p. R103-17.

120. Pobre, K.F.R., G.J. Poet, and L.M. Hendershot, *The endoplasmic reticulum (ER) chaperone BiP is a master regulator of ER functions: Getting by with a little help from ERdj friends.* J Biol Chem, 2019. **294**(6): p. 2098-2108.

121. Bergeron, J.J., et al., *Calnexin: a membrane-bound chaperone of the endoplasmic reticulum.* Trends Biochem Sci, 1994. **19**(3): p. 124-8.

122. Halperin, L., J. Jung, and M. Michalak, *The many functions of the endoplasmic reticulum chaperones and folding enzymes.* IUBMB Life, 2014. **66**(5): p. 318-26.

123. Corbett, E.F., et al., *Ca2+ regulation of interactions between endoplasmic reticulum chaperones.* J Biol Chem, 1999. **274**(10): p. 6203-11.

124. Prell, T., J. Lautenschläger, and J. Grosskreutz, *Calcium-dependent protein folding in amyotrophic lateral sclerosis.* Cell Calcium, 2013. **54**(2): p. 132-43.

125. Mazzorana, M. and T.L. Sørensen, *Calcium-Induced Protein Folding in Calumenin and Calmodulin.* Methods Mol Biol, 2019. **1929**: p. 517-537.

126. Rand, M.D., et al., *Calcium depletion dissociates and activates heterodimeric notch receptors.* Mol Cell Biol, 2000. **20**(5): p. 1825-35.

127. Camacho, P. and J.D. Lechleiter, *Calreticulin inhibits repetitive intracellular Ca2+ waves.* Cell, 1995. **82**(5): p. 765-71.

128. John, L.M., J.D. Lechleiter, and P. Camacho, *Differential modulation of SERCA2 isoforms by calreticulin.* J Cell Biol, 1998. **142**(4): p. 963-73.

129. Avezov, E., et al., *Retarded PDI diffusion and a reductive shift in poise of the calcium depleted endoplasmic reticulum.* BMC Biol, 2015. **13**: p. 2.

130. Oslowski, C.M. and F. Urano, *Measuring ER stress and the unfolded protein response using mammalian tissue culture system.* Methods Enzymol, 2011. **490**: p. 71-92.

131. Snyder, J.T., et al., *Endoplasmic Reticulum Stress Induced Proliferation Remains Intact in Aging Mouse β-Cells.* Front Endocrinol (Lausanne), 2021. **12**: p. 734079.

132. Jetton, T.L., et al., *Mechanisms of compensatory beta-cell growth in insulin-resistant rats: roles of Akt kinase.* Diabetes, 2005. **54**(8): p. 2294-304.

133. Marchetti, P., et al., *The endoplasmic reticulum in pancreatic beta cells of type 2 diabetes patients.* Diabetologia, 2007. **50**(12): p. 2486-94.

134. Delépine, M., et al., *EIF2AK3, encoding translation initiation factor 2-alpha kinase 3, is mutated in patients with Wolcott-Rallison syndrome.* Nat Genet, 2000. **25**(4): p. 406-9.

135. De Franco, E., et al., *De Novo Mutations in EIF2B1 Affecting eIF2 Signaling Cause Neonatal/Early-Onset Diabetes and Transient Hepatic Dysfunction.* Diabetes, 2020. **69**(3): p. 477-483.

136. Synofzik, M., et al., *Absence of BiP co-chaperone DNAJC3 causes diabetes mellitus and multisystemic neurodegeneration.* Am J Hum Genet, 2014. **95**(6): p. 689-97.

137. Abdulkarim, B., et al., *A Missense Mutation in PPP1R15B Causes a Syndrome Including Diabetes, Short Stature, and Microcephaly.* Diabetes, 2015. **64**(11): p. 3951-62.

138. Cnop, M., et al., *Endoplasmic reticulum stress and eIF2α phosphorylation: The Achilles heel of pancreatic β cells.* Mol Metab, 2017. **6**(9): p. 1024-1039.

139. Zhang, I.X., et al., *ER stress increases expression of intracellular calcium channel RyR1 to modify Ca(2+) homeostasis in pancreatic beta cells.* J Biol Chem, 2023. **299**(8): p. 105065.

140. Zhang, I.X., et al., *ER stress increases store-operated Ca(2+) entry (SOCE) and augments basal insulin secretion in pancreatic beta cells.* J Biol Chem, 2020. **295**(17): p. 5685-5700.

141. Prakriya, M. and R.S. Lewis, *Store-Operated Calcium Channels.* Physiol Rev, 2015. **95**(4): p. 1383-436.

142. Kono, T., et al., *Impaired Store-Operated Calcium Entry and STIM1 Loss Lead to Reduced Insulin Secretion and Increased Endoplasmic Reticulum Stress in the Diabetic β-Cell.* Diabetes, 2018. **67**(11): p. 2293-2304.

143. Prole, D.L. and C.W. Taylor, *Structure and Function of IP(3) Receptors.* Cold Spring Harb Perspect Biol, 2019. **11**(4).

144. Jayaraman, T., et al., *The inositol 1,4,5-trisphosphate receptor is essential for T-cell receptor signaling.* Proc Natl Acad Sci U S A, 1995. **92**(13): p. 6007-11.

145. Taufiq, A.M., et al., *Involvement of IP3 receptors in LTP and LTD induction in guinea pig hippocampal CA1 neurons.* Learn Mem, 2005. **12**(6): p. 594-600.

146. Oduori, O.S., et al., *Gs/Gq signaling switch in β cells defines incretin effectiveness in diabetes.* J Clin Invest, 2020. **130**(12): p. 6639-6655.

147. Luciani, D.S., et al., *Roles of IP3R and RyR Ca2+ channels in endoplasmic reticulum stress and beta-cell death.* Diabetes, 2009. **58**(2): p. 422-32.

148. Hogan, P.G. and A. Rao, *Store-operated calcium entry: Mechanisms and modulation.* Biochem Biophys Res Commun, 2015. **460**(1): p. 40-9.

149. Lopez, J.J., et al., *TRPC Channels in the SOCE Scenario.* Cells, 2020. **9**(1).

150. Williams, R.T., et al., *Identification and characterization of the STIM (stromal interaction molecule) gene family: coding for a novel class of transmembrane proteins.* Biochem J, 2001. **357**(Pt 3): p. 673-85.

151. Zhou, Y., et al., *The short N-terminal domains of STIM1 and STIM2 control the activation kinetics of Orai1 channels.* J Biol Chem, 2009. **284**(29): p. 19164-8.

152. Emrich, S.M., et al., *Omnitemporal choreographies of all five STIM/Orai and IP(3)Rs underlie the complexity of mammalian Ca(2+) signaling.* Cell Rep, 2021. **34**(9): p. 108760.

153. Zheng, L., et al., *Biophysical characterization of the EF-hand and SAM domain containing Ca2+ sensory region of STIM1 and STIM2.* Biochem Biophys Res Commun, 2008. **369**(1): p. 240-6.

154. Brandman, O., et al., *STIM2 is a feedback regulator that stabilizes basal cytosolic and endoplasmic reticulum Ca2+ levels.* Cell, 2007. **131**(7): p. 1327-39.

155. Hou, X., et al., *Crystal structure of the calcium release-activated calcium channel Orai.* Science, 2012. **338**(6112): p. 1308-13.

156. Demuro, A., et al., *Subunit stoichiometry of human Orai1 and Orai3 channels in closed and open states.* Proc Natl Acad Sci U S A, 2011. **108**(43): p. 17832-7.

157. Penna, A., et al., *The CRAC channel consists of a tetramer formed by Stim-induced dimerization of Orai dimers.* Nature, 2008. **456**(7218): p. 116-20.

158. Ji, W., et al., *Functional stoichiometry of the unitary calcium-release-activated calcium channel.* Proc Natl Acad Sci U S A, 2008. **105**(36): p. 13668-73.

159. Palty, R., et al., *SARAF inactivates the store operated calcium entry machinery to prevent excess calcium refilling.* Cell, 2012. **149**(2): p. 425-38.

160. Zomot, E., et al., *Bidirectional regulation of calcium release-activated calcium (CRAC) channel by SARAF.* J Cell Biol, 2021. **220**(12).

161. Srikanth, S., et al., *A novel EF-hand protein, CRACR2A, is a cytosolic Ca2+ sensor that stabilizes CRAC channels in T cells.* Nat Cell Biol, 2010. **12**(5): p. 436-46.

162. Li, X., et al., *Calmodulin dissociates the STIM1-Orai1 complex and STIM1 oligomers.* Nat Commun, 2017. **8**(1): p. 1042.

163. Song, H.J., et al., *PKC-β modulates Ca(2+) mobilization through Stim1 phosphorylation.* Genes Genomics, 2022. **44**(5): p. 571-582.

164. Martínez-Martínez, E., et al., *PKC-Mediated Orai1 Channel Phosphorylation Modulates Ca(2+) Signaling in HeLa Cells.* Cells, 2022. **11**(13).

165. Feriotto, G., et al., *Myocyte enhancer factor 2 activates promoter sequences of the human AbetaH-J-J locus, encoding aspartyl-beta-hydroxylase, junctin, and junctate.* Mol Cell Biol, 2005. **25**(8): p. 3261-75.

166. Dinchuk, J.E., et al., *Absence of post-translational aspartyl beta-hydroxylation of epidermal growth factor domains in mice leads to developmental defects and an increased incidence of intestinal neoplasia.* J Biol Chem, 2002. **277**(15): p. 12970-7.

167. Arvanitis, D.A., et al., *Histidine-rich calcium binding protein: the new regulator of sarcoplasmic reticulum calcium cycling.* J Mol Cell Cardiol, 2011. **50**(1): p. 43-9.

168. Treves, S., et al., *Junctate is a key element in calcium entry induced by activation of InsP3 receptors and/or calcium store depletion.* J Cell Biol, 2004. **166**(4): p. 537-48.

169. Srikanth, S., et al., *Junctate is a Ca2+-sensing structural component of Orai1 and stromal interaction molecule 1 (STIM1).* Proc Natl Acad Sci U S A, 2012. **109**(22): p. 8682-7.

170. Stenflo, J., et al., *Hydroxylation of aspartic acid in domains homologous to the epidermal growth factor precursor is catalyzed by a 2-oxoglutarate-dependent dioxygenase.* Proc Natl Acad Sci U S A, 1989. **86**(2): p. 444-7.

171. Brewitz, L., B.C. Onisko, and C.J. Schofield, *Combined proteomic and biochemical analyses redefine the consensus sequence requirement for epidermal growth factor-like domain hydroxylation.* J Biol Chem, 2022. **298**(8): p. 102129.

172. Tong, M., et al., *Phosphorylation Modulates Aspartyl-(Asparaginyl)-β Hydroxylase Protein Expression, Catalytic Activity and Migration in Human Immature Neuronal Cerebellar Cells.* Cell Biol (Henderson, NV), 2013. **6**(2).

173. Stenflo, J., Y. Stenberg, and A. Muranyi, *Calcium-binding EGF-like modules in coagulation proteinases: function of the calcium ion in module interactions.* Biochim Biophys Acta, 2000. **1477**(1-2): p. 51-63.

174. Derian, C.K., et al., *Inhibitors of 2-ketoglutarate-dependent dioxygenases block aspartyl beta-hydroxylation of recombinant human factor IX in several mammalian expression systems.* J Biol Chem, 1989. **264**(12): p. 6615-8.

175. Pfeffer, I., et al., *Aspartate/asparagine-β-hydroxylase crystal structures reveal an unexpected epidermal growth factor-like domain substrate disulfide pattern.* Nat Commun, 2019. **10**(1): p. 4910.

176. Dong, X., et al., *Aspartate β-Hydroxylase expression promotes a malignant pancreatic cellular phenotype.* Oncotarget, 2015. **6**(2): p. 1231-48.

177. Zou, Q., et al., *Hydroxylase Activity of ASPH Promotes Hepatocellular Carcinoma Metastasis Through Epithelial-to-Mesenchymal Transition Pathway.* EBioMedicine, 2018. **31**: p. 287-298.

178. Shawaf, S., et al., *A family with a syndrome of ectopia lentis, spontaneous filtering blebs, and craniofacial dysmorphism.* Ophthalmic Genet, 1995. **16**(4): p. 163-9.

179. Jones, G., et al., *Traboulsi syndrome caused by mutations in ASPH: An autosomal recessive disorder with overlapping features of Marfan syndrome.* Eur J Med Genet, 2022. **65**(10): p. 104572.

180. Dinchuk, J.E., et al., *Aspartyl beta -hydroxylase (Asph) and an evolutionarily conserved isoform of Asph missing the catalytic domain share exons with junctin.* J Biol Chem, 2000. **275**(50): p. 39543-54.

181. Györke, I., et al., *The role of calsequestrin, triadin, and junctin in conferring cardiac ryanodine receptor responsiveness to luminal calcium.* Biophys J, 2004. **86**(4): p. 2121-8.

182. Branon, T.C., et al., *Efficient proximity labeling in living cells and organisms with TurboID.* Nat Biotechnol, 2018. **36**(9): p. 880-887.

183. Zhu, A., et al., *Fatal hemorrhage in mice lacking gamma-glutamyl carboxylase.* Blood, 2007. **109**(12): p. 5270-5.

184. Wei, J. and G. Karsenty, *An overview of the metabolic functions of osteocalcin.* Rev Endocr Metab Disord, 2015. **16**(2): p. 93-8.

185. Mark, M.R., et al., *Characterization of Gas6, a member of the superfamily of G domain-containing proteins, as a ligand for Rse and Axl.* J Biol Chem, 1996. **271**(16): p. 9785-9.

186. Tanaka, M. and D.W. Siemann, *Gas6/Axl Signaling Pathway in the Tumor Immune Microenvironment.* Cancers (Basel), 2020. **12**(7).

187. Rothlin, C.V., et al., *TAM receptors are pleiotropic inhibitors of the innate immune response.* Cell, 2007. **131**(6): p. 1124-36.

188. Kulman, J.D., et al., *Primary structure and tissue distribution of two novel proline-rich gamma-carboxyglutamic acid proteins.* Proc Natl Acad Sci U S A, 1997. **94**(17): p. 9058-62.

189. Li, T., et al., *Identification of a Drosophila vitamin K-dependent gamma-glutamyl carboxylase.* J Biol Chem, 2000. **275**(24): p. 18291-6.

190. Srivastava, M., et al., *The Trichoplax genome and the nature of placozoans.* Nature, 2008. **454**(7207): p. 955-60.

191. Adams, M.D., et al., *The genome sequence of Drosophila melanogaster.* Science, 2000. **287**(5461): p. 2185-95.

192. Jumper, J., et al., *Highly accurate protein structure prediction with AlphaFold.* Nature, 2021. **596**(7873): p. 583-589.

193. Sehgal, P., et al., *Inhibition of the sarco/endoplasmic reticulum (ER) Ca(2+)-ATPase by thapsigargin analogs induces cell death via ER Ca(2+) depletion and the unfolded protein response.* J Biol Chem, 2017. **292**(48): p. 19656-19673.

194. Treves, S., et al., *Molecular cloning, expression, functional characterization, chromosomal localization, and gene structure of junctate, a novel integral calcium binding protein of sarco(endo)plasmic reticulum membrane.* J Biol Chem, 2000. **275**(50): p. 39555-68.

195. Cohen, S.M., et al., *Calmodulin shuttling mediates cytonuclear signaling to trigger experience-dependent transcription and memory.* Nat Commun, 2018. **9**(1): p. 2451.

196. Kozlov, G. and K. Gehring, *Calnexin cycle - structural features of the ER chaperone system.* Febs j, 2020. **287**(20): p. 4322-4340.

197. Maurer, P. and E. Hohenester, *Structural and functional aspects of calcium binding in extracellular matrix proteins.* Matrix Biol, 1997. **15**(8-9): p. 569-80; discussion 581.

198. Prins, D. and M. Michalak, *Organellar calcium buffers.* Cold Spring Harb Perspect Biol, 2011. **3**(3).

199. Lamb, H.K., et al., *The affinity of a major Ca2+ binding site on GRP78 is differentially enhanced by ADP and ATP.* J Biol Chem, 2006. **281**(13): p. 8796-805.

200. Nakamura, K., et al., *Functional specialization of calreticulin domains.* J Cell Biol, 2001. **154**(5): p. 961-72.

201. Park, H., et al., *Comparing skeletal and cardiac calsequestrin structures and their calcium binding: a proposed mechanism for coupled calcium binding and protein polymerization.* J Biol Chem, 2004. **279**(17): p. 18026-33.

202. Klejman, M.E., et al., *Expression of STIM1 in brain and puncta-like co-localization of STIM1 and ORAI1 upon depletion of Ca(2+) store in neurons.* Neurochem Int, 2009. **54**(1): p. 49-55.

203. Su, A.I., et al., *A gene atlas of the mouse and human protein-encoding transcriptomes.* Proc Natl Acad Sci U S A, 2004. **101**(16): p. 6062-7.

204. Adams, M.T., et al., *Reduced synchroneity of intra-islet Ca(2+) oscillations in vivo in Robo-deficient β cells.* Elife, 2021. **10**.

205. *Single-cell transcriptomics of 20 mouse organs creates a Tabula Muris.* Nature, 2018. **562**(7727): p. 367-372.

206. Dror, V., et al., *Notch signalling suppresses apoptosis in adult human and mouse pancreatic islet cells.* Diabetologia, 2007. **50**(12): p. 2504-15.

207. Haze, K., et al., *Identification of the G13 (cAMP-response-element-binding protein-related protein) gene product related to activating transcription factor 6 as a transcriptional activator of the mammalian unfolded protein response.* Biochem J, 2001. **355**(Pt 1): p. 19-28.

208. Read, A. and M. Schröder, *The Unfolded Protein Response: An Overview*. Biology (Basel), 2021. **10**(5).

209. Zhao, X., et al., *GLP-1 Receptor Agonists: Beyond Their Pancreatic Effects.* Front Endocrinol (Lausanne), 2021. **12**: p. 721135.

210. Keebler, M.V. and C.W. Taylor, *Endogenous signalling pathways and caged IP(3) evoke Ca(2+) puffs at the same abundant immobile intracellular sites.* J Cell Sci, 2017. **130**(21): p. 3728-3739.

211. Wu, C., et al., *BioGPS: an extensible and customizable portal for querying and organizing gene annotation resources.* Genome Biol, 2009. **10**(11): p. R130.

212. Lacombe, J., et al., *Vitamin K-dependent carboxylation regulates Ca(2+) flux and adaptation to metabolic stress in β cells.* Cell Rep, 2023. **42**(5): p. 112500.